# DISPERSIVE WAVE ATTENUATION AND REFOCUSING DUE TO DISORDERED OROGRAPHIC FORCING

By
Juan Carlos Muñoz Grajales

Instituto de Matemática Pura e Aplicada
Rio de Janeiro
November 2002

### Abstract

The shape of an acoustic wave is strongly affected as it propagates through a highly disordered medium. O'Doherty and Anstey [49] characterized this phenomenon by means of a deterministic approximation which accurately predicts the attenuation, broadening and delay acting on the incoming pulse. This delay is observed relative to the wave's travel time up to a fixed station into the medium.

In this work we study the interaction of weakly-nonlinear, weakly-dispersive water waves with shallow channels with highly variable depth, by using a Boussinesq-type system. We generalize the O'Doherty-Anstey approximation for the linearization of this weakly-dispersive system forced by a disordered orography. This is achieved by applying the invariant imbedding method to the equations governing the transmitted and reflected fields. We find that dispersive effects alter the medium's correlation function increasing the overall attenuation, delay and the pulse's spreading rate. Furthermore, at a fixed medium's station the wave's coherent front is found to stabilize, independent of the particular realization of the orography, when observed relative to its first arrival time.

The linear theory is found to be in excellent agreement with the weakly-nonlinear simulations performed for different values of the relevant parameters by using a high-order finite difference scheme proposed by Wei and Kirby [56]. This computing scheme is further employed to explore the refocusing property, a subject of great interest treated in recent works by Clouet and Fouque [17] and Prada and Fink [52]. New results for the refocusing of dispersive Gaussian-shaped disturbances and solitary waves are presented.

**Resumo**

A forma de uma onda acústica é fortemente afetada quando esta propaga em um meio altamente desordenado. O'Doherty e Anstey [49] caracterizaram este fenômeno usando uma aproximação determinística que prevê com precisão a atenuação, o espalhamento e o retardo que atuam sobre o pulso incidente. O retardo observado é relativo ao tempo de viagem da onda até uma estação fixa no meio.

Neste trabalho, estudamos a interação de ondas aquáticas fracamente não lineares, fracamente dispersivas com canais rasos de profundidade altamente variável, usando um sistema do tipo Boussinesq. Generalizamos a aproximação de O'Doherty-Anstey para a linearização deste sistema fracamente dispersivo quando este é forçado por uma orografia desordenada. Para isso aplicamos o método da imersão invariante às equações que governam os campos transmitido e refletido. Encontramos que os efeitos dispersivos modificam a função de correlação do meio incrementando a atenuação total, o retardo e a taxa de espalhamento do pulso. Além disso, em uma estação fixa no meio, a frente coerente da onda estabiliza, independentemente da realização particular da orografia, quando observada relativa ao seu tempo de chegada.

A teoria linear desenvolvida está em excelente acordo com as simulações fracamente não lineares, para diferentes valores dos parâmetros relevantes, realizadas usando um esquema de diferenças finitas de alta ordem proposto por Wei e Kirby [56]. Este esquema computacional é também usado para explorar a propriedade de refocalização, um assunto de grande interese tratado em trabalhos recentes por Clouet and Fouque [17] and Prada and Fink [52]. Apresentamos novos resultados de refocalização para perturbações Gaussianas dispersivas e ondas solitárias.

# Acknowledgements

I thank to my thesis advisor, Professor André Nachbin for proposing me the problem studied in this investigation. I am grateful for his dedication and support during my stay at IMPA. His excellent lectures in Fluid Dynamics and clear ideas enriched my work.

I would like to thank Professor Dan Marchesin, whom I had the opportunity of collaborating with at IMPA. I benefited from his lectures and seminars on Numerical Methods.

I further express my gratefulness to Professors Rafael Iório, Carlos Tomei, Marcus Sarkis and Martin Tygel, who kindly accepted to participate in my thesis committee and for their valuable suggestions that improved the final text.

I thank to my mother Graciela and my family in Colombia for their affection and support. They always encouraged me in difficult moments.

Finally I thank to the Conselho Nacional de Desenvolvimento Científico e Tecnológico (CNPq) for financing my doctoral studies in Brazil.

# Contents

# Chapter 1

# Introduction

In designing mechanisms for coastal protection it is of primary interest to study the processes of transmission and reflection of waves scattering over submerged orographies (mountains). In some cases may reduce a great deal of energy contained in the waves. It is then essential to characterize the shape of the travelling signal and the reflection produced by this wave-depth interaction. Understanding this process we can improve the efficiency of computer simulations.

In the context of linear acoustic waves in highly-variable media (such as the earth crust) one of such tools was discovered by O'Doherty and Anstey [49] in 1971. Their result showed that, at large distances of propagation the transmitted wave front (i.e. the leading part of the signal arriving at a selected observation station) appears to be diffused around a moving center in a similar way to a deterministic diffusion mechanism, from which they obtain an excellent estimate. This implies in a progressive broadening, attenuation and delay of the incoming pulse caused by the multiply scattered energy generated by the interaction between the propagating signal and the fine scale fluctuations of the medium. The delay of the pulse is relative to its travel time up to a fixed observation station into the medium.

Since O'Doherty-Anstey's research several investigators have explored the phenomenon in different types of hyperbolic systems and regimes through techniques that include multiple scales, probability, asymptotic analysis and invariant imbedding approaches [3], [12], [11], [16]. In [32] the theory is extended to a hyperbolic dissipative system and in [55] to three-dimensional spherical waves in locally layered heterogeneous media by using ray theory and stochastic analysis. The pulse-shaping theory is generalized to the reflected signal in [33]. In [9], Berlyand and Burridge derive the O'Doherty-Anstey approximation within a deterministic framework without introducing small parameters or stochastic analysis. Moreover a frequency-dependent estimate is deduced for the error in their approximation.

In the present work many aspects of the hyperbolic theory will be extended to dispersive waves. This is the major theoretical contribution of this thesis. We are concerned with the transmission and reflection of small-amplitude dispersive water waves propagating over shallow coastal regions. Particularly, we want to focus on the interaction of the wave with the small-scale features of the coast's depth. The section of the coast considered is modelled as a one-dimensional shallow channel with disordered (random) depth. Modelling uncertainty is a reasonable strategy because in a real situation we might not know the exact constitution of the sea bottom. The scale $\ell$ in which the submersed orography varies (**the correlation length**) is assumed to be smaller than the typical wavelength $\ell_p$ (a rapidly-varying depth). To be more specific, we adopt the ratio $\ell/\ell_p = 1/10$. We will show that this scaling is sufficient for an initial disturbance to be strongly altered by the presence of the variable depth at large distances from the source.

For studying in detail the interplay disorder-dispersion in the pulse-shaping mechanism we extend the result by O'Doherty-Anstey to dispersive water waves modelled by the linearized terrain-following Boussinesq system derived by Nachbin [45]. This is our first goal. The full, weakly-nonlinear, weakly-dispersive Boussinesq model is a one-dimensional system, with orography-dependent coefficients governing the wave elevation and the velocity field of gravity driven waves which is valid for arbitrary orographies provided that

$$\begin{aligned}
\alpha &= a_o/h_o << 1 \quad \text{(small amplitude waves)}, \\
\beta &= h_o^2/\ell_p^2 << 1 \quad \text{(shallow water or equivalently long-wave regime)},
\end{aligned} \tag{1.1}$$

where $a_o$ and $h_o$ are the characteristic amplitude of the waves and the characteristic depth, respectively. The foregoing features make this model (presented in the next chapter) applicable to our current problem. The dimensionless ratios $\alpha$ and $\beta$ are called the **nonlinearity and dispersion parameters** and characterize the specific regime we are interested in. The terms weakly-nonlinear and weakly-dispersive used above refer to assumptions (1.1).

Several authors have studied highly-disordered orographies. A theory for the reflected signal is developed in [47] by employing techniques of stochastic and asymptotic analysis on the linearized potential theory equations. In [46] is treated the localization phenomena in dispersive waves and in [22] is explored the aspect of refocusing of hyperbolic water waves in disordered depths. Waves over irregular depths and different regimes have been further considered in [14], [29], [31], [41]. Rosales and Papanicolaou [53] treat the special case of periodic bottoms for dispersive waves on the full, nonlinear potential theory equations by employing the method of multiple scales in the regime of shallow waters and small amplitude waves and Guazzeli et al. [25] study Bragg's resonance phenomenon for periodic beds. In [58] and [36] are examined numerically the mechanisms of refraction, diffraction and reflection of dispersive long waves over slowly-varying bottoms. For this, the full nonlinear Peregrine's Boussinesq model is decomposed as a coupled system of nonlinear differential equations for the spectral components of the signal.

The initial disturbances (in space) we consider in the numerical validation of the theory are Gaussian-shaped pulses and solitary waves (nonlinear pulses). Such profiles are usual in fluid dynamics and can be used as a simple model of a tsunami, a long wave with small amplitude and a high propagation speed generated by submarine earthquakes which are of great interest in ocean exploration [40]. We point out that the theory presented is also valid for general disturbances provided that they are smooth and compactly supported.

For obtaining the dispersive pulse-shaping estimate we exploit the analogy existing between the model of acoustic waves and the Boussinesq model adopted here. The rapidly-varying orography is the medium through which the waves propagate. The main ingredients in the analysis are (a) the equations governing the fluid can be decomposed as a pair of coupled KdV-type equations which are a dispersive perturbation of those derived in [9] and (b) the finite effective propagation speed of dispersive waves. These two facts are crucial in order to apply the invariant imbedding approach as in [9].

The new approximation that we obtain furnishes an accurate prediction for the shape of the transmitted (coherent) wave front (that resembles the incoming pulse) and even for a part of the random oscillatory (incoherent) coda following it. The latter appears as a consequence of the multiple reflections taking place between the signal and the variable medium. To our knowledge no such complete characterization for the shaping of dispersive waves can be found in previous works. Its expression is simple because it is found to depend only on the initial disturbance and the correlation function of the orography's properties, turning its computation inexpensive. In addition, an estimate for the error of the approximation is given which is sharp in the case of a Goupillaud-type orography. This is a type of piecewise constant medium in which the travel time in each section is constant.

In general, the Boussinesq system that formulates our problem can not be solved analytically. Further, the construction of an efficient numerical scheme for solving it is not an easy task. The reason is that the scheme must be able to resolve the fine-scale details of the disorder and, at the same time, describe accurately the dispersive characteristics of the model. Typically, this amounts to adopting smaller (in space and time) step sizes turning the code very slow. The numerical scheme we propose for the validation of the theory is adapted from the work by Wei and Kirby [56]. It is a high-order finite difference scheme that we find very accurate and stable with a low computational cost. The numerical simulations are conducted in the full nonlinear Boussinesq model which permitted our initiation in the study of the effect of small nonlinearities in the phenomena, in particular solitary waves.

The main results inferred from our theory and numerical simulations are the following. The incoming pulse is strongly affected by the rapid orography fluctuations being simultaneously broadened, attenuated and delayed relative to a system of coordinates travelling with the wave. All these effects are perfectly reproduced by the computation. In constant depth a dispersive wave (opposite to a hyperbolic one) develops an Airy-like oscillatory coda which progressively spreads backward as it propagates. The novelty in a rapidly-varying medium is that part of this dispersive coda is destroyed by the disorder. The high frequency modes are the first to be altered by the variable depth. This is a manifestation of the **localization** phenomenon treated in [46].

The linear theory is found to be very robust and in excellent agreement with the weakly-nonlinear simulations over the range $0 \leq \alpha \leq 0.001$, $0 \leq \beta \leq 0.01$. The largest level of nonlinearity considered $\alpha = 0.01$ is nonnegligible (therefore beyond the limit of application of a linear theory). But for this value our theory even gives a reasonable prediction for the pulse-shape. From the results we conclude that the new dispersive pulse-shaping theory provides a valuable tool for understanding the interplay between weak dispersion and disorder in waves with small amplitude.

As pointed out in [55], the O'Doherty-Anstey effect is in fact a phenomenon of redistribution of the energy among the Fourier modes compounding the signal. The energy contained in the incoming pulse is progressively filtered by the multiple reflections with the disordered medium. This reflected energy builds in the incoherent coda behind the leading transmitted front and in the incoherent reflected wave.

A fact not noticed in the original paper by O'Doherty and Anstey is that if we observe the shape of the wave front relative to its arrival time at some fixed medium station it results independent of the particular realization of the rapidly-varying medium. This remarkable fact is called **stabilization property** and is due to the pulse being broad with respect to the correlation length of the medium. This is the key that makes the O'Doherty-Anstey approximation very robust. It was formulated rigorously in [12] for acoustic waves in a Goupillaud medium through an averaging approach. The theory is validated in that paper through numerical simulations. In [35] and [34] the stabilization aspect is generalized to certain type of multidimensional hyperbolic systems which include in particular the elastic wave equations in a random two-dimensional medium. A second goal of our research is to explore, we believe for the first time, this phenomenon for dispersive nonlinear waves, in particular weak solitary waves.

Finally, our third goal is to apply the numerical solver implemented in the full nonlinear terrain-following Boussinesq model for studying **refocusing** by the time-reversal method of dispersive waves. The goal is to recover the location and the shape of the initial disturbance by using solely part of the generated transmitted or reflected signal. Here we consider only the refocusing in the reflected signal. In the linear regime we derive a deterministic approximation for the shape of the refocused pulse in terms of the incoming pulse and the function characterizing the reflection properties of the medium. The refocusing property has been already explored for highly-variable acoustic mediums in [52], [17] and in water waves by [22]. Nevertheless, it had not been treated for dispersive waves until recently. Based on this work's preprint [43], a stochastic theory has been developed complementing our findings [23].

## 1.1 Future plans

This work initiates and points out several lines of research. In first place, we intend to use the full nonlinear numerical code developed here to study the aspects of refocusing and stabilization for solitary waves for larger levels of nonlinearity and dispersion. In the present study we only examine these phenomena for weak solitons ($\alpha = \beta = 0.001$). Also, instead of using the reflected signal in the time-reversal refocusing as done here, we could consider a part of transmitted signal arriving at a selected observation station. The goal is again to recover the location and shape of the original disturbance. It has potential applications in oceanography, in particular to explore tsunami's sources. The results of such a numerical research would surely furnish valuable information for developing a full nonlinear theory of refocusing and stabilization in dispersive waves not available at the moment.

We also plan to explore other problems of interest such as the shoaling and reflection of nonlinear irregular waves over shallow coastal regions with slowly-varying or constant slope bottoms without the restriction of the mild-slope condition as in earlier works [58], [36], where Peregrine's model [51] is adopted. Such situations can be dealt with the terrain-following system because it is valid for arbitrary shallow depths as mentioned earlier. Our dispersive pulse-shape estimate could also be tested in these new orography regimes.

Finally, the problem of existence and uniqueness of solutions to our model for the reflected and transmitted modes is a subject of further research. In this connection we think that the invariant imbedding technique (see Appendix B) could be useful even in the nonlinear case.

## 1.2 Outline and organization

This work is organized as follows.

In Chapter 2 we present the governing equations and problem's scaling, define the quantities of interest and derive the dispersive pulse-shaping approximation. Chapter 3 is devoted to the numerical validation of the theory. Several wave-orography regimes are considered. It is further explored numerically for the stabilization of the shape of Gaussian-shaped pulses and solitary waves. Chapter 4 deals with the refocusing property for dispersive waves, including weak solitons, through several numerical experiments. In addition, a theoretical formula predicting the shape of the refocused pulse is obtained. In Chapter 5 we validate numerically the consistency of the terrain-following Boussinesq system with others models in the literature and point out some of its theoretical and numerical advantages. The conclusions of the investigation are presented in Chapter 6.

To avoid including details that would interfere with the flow of the presentation and for making it self-contained, complementary material is distributed over several appendices.

In Appendix A we present the closed-form solution via Fourier transform for the linear KdV equation and the linearized Boussinesq model with constant coefficients. Appendix B is a brief summary of results concerning the invariant imbedding approach with applications in particular to the reflection-transmission problem studied in this work. In Appendix C we check the consistency of the theory in the nondispersive and constant depth regime. Appendix D details the computation of the components of our pulse-shape formula. Appendix E analyzes the error function of the pulse-shaping theory for the special case of a Goupillaud-type orography. Appendix F presents an alternative decomposition given by Mattioli [39] for a Boussinesq-type system and contrasts it with that proposed in this work. Appendix G shows how to calculate the scattering parameters involved in the pulse-shape approximation. Finally, in Appendix H we calculate the truncation error of the numerical scheme by Wei and Kirby's [56].

# Chapter 2

# The linear pulse-shaping theory

In this chapter we derive a generalization of the O'Doherty-Anstey approximation (initially deduced in the context of acoustic waves) in order to study the mechanism of pulse-shaping of linear dispersive waves propagating over a section of coast with a highly disordered depth. This estimate explains the attenuation, broadening and delay observed in the incoming pulse as a consequence of the interaction of the wave with the fine-scale details of the section of bottom sea considered. The modelling of the wave motion is done through the recently derived terrain-following Boussinesq system [45], a weakly-nonlinear, weakly dispersive model with smooth variable coefficients which is valid for arbitrary depths, as an asymptotic approximation of the equations of the potential theory. The pulse-shaping approximation presented will be validated in Chapter 3 through numerical simulations in the Boussinesq model that formulates our problem for different values of the parameters of interest.

## 2.1 Problem formulation

In past years several Boussinesq-type equations have been employed to model surface wave propagation in shallow channels. In such models the fluid is assumed to be inviscid, incompressible and irrotational. Peregrine [51] in 1967 deduced a nonlinear model valid for channels of slowly varying depth, whereas Hamilton [26] in 1977 derived a linear set of equations valid for arbitrary orographies. He used an appropriate curvilinear coordinate system and applied a perturbation approach to the equations of the linear potential theory retaining the lowest-order effects of dispersion. Hamilton [26] also outlines the formulation of a weakly-nonlinear model by considering a Lagragian functional. Recently, using dimensionless variables and Hamilton's conformal mapping strategy, Nachbin [45] derived the **terrain-following nonlinear Boussinesq system** in one dimension

$$M(\xi)\eta_t + \left(\left(1+\frac{\alpha\eta}{M(\xi)}\right)u\right)_\xi = 0, \tag{2.1}$$
$$u_t + \eta_\xi + \frac{\alpha}{2}\left(\frac{u^2}{M(\xi)^2}\right)_\xi - \frac{\beta}{3}u_{\xi\xi t} = 0,$$

where $-\infty < \xi < \infty$ and $t > 0$ are the space and time coordinates, respectively, $\eta = \eta(\xi, t)$ is the wave elevation and $u = u(\xi, t)$ is the depth-averaged velocity. Also, $\alpha = a_o/h_o$ is the parameter regulating the strength of nonlinear effects ($a_o$ is the characteristic wave amplitude), $\beta > 0$ is the dispersion parameter defined by $\beta = h_o^2/\ell_p^2$ with $h_o$ the characteristic depth and $\ell_p$ the typical wavelength. The variable coefficient $M(\xi)$ is a smooth orography dependent function to be defined later. The parameters $\alpha$ and $\beta$ must be small enough (equivalently small-amplitude and shallow channel/long waves) so that the terms neglected in the perturbation analysis are in fact of higher order.

### 2.1.1 Outline of the derivation of the terrain-following Boussinesq system

In [45], the starting point to derive system (2.1) is the equations of the potential theory, that in dimensionless variables can be written as (see [57])

$$\beta\,\phi_{xx} + \phi_{yy} = 0 \quad \text{for} \quad -H(x/\gamma) < y < \alpha\eta(x,t), \qquad -\infty < x < \infty,$$

with the nonlinear free surface conditions

$$\eta_t + \alpha\phi_x\eta_x - \frac{1}{\beta}\phi_y = 0,$$

$$\eta + \phi_t + \frac{\alpha}{2}\left(\phi_x^2 + \frac{1}{\beta}\phi_y^2\right) = 0$$

at $y = \alpha\eta(x,t)$. Here $\phi(x, y, t)$ denotes the potential velocity, $\eta(x, t)$ the wave elevation measured with respect to the undisturbed free surface $y = 0$ and the dimensionless parameter $\gamma = \ell/\ell_p$ measures the ratio inhomogeneities/wavelength.

The Neumann condition at the impermeable bottom is

$$\phi_y + \frac{\beta}{\gamma}\,H'(x/\gamma)\phi_x = 0. \tag{2.2}$$

The bottom topography is described by $y = -H(x/\gamma)$ where

$$H(x/\gamma) \quad = \quad \begin{cases} 1 + n(x/\gamma) & \text{when} \quad 0 < x < L \\ 1 & \text{when} \quad x \leq 0 \quad \text{or} \quad x \geq L. \end{cases}$$

The bottom profile is described by the (possibly rapidly varying) function $-n(x/\gamma)$. The topography is rapidly varying when $\gamma \ll 1$. The undisturbed depth is given by $y = \; -1$ and the topography can be of large amplitude provided that $|n| < 1$. The fluctuations $n$ are not assumed to be small, nor continuous, nor slowly varying.

Following Hamilton [26], in [45] is defined a symmetric flow domain by reflecting the original one about the undisturbed free surface (c.f. figure 2.1). This domain is denoted by $\Omega_z$ where $z = x + i\sqrt{\beta}y$ and can be considered as the conformal image of the strip $\Omega_w$ where $w = \xi + i\tilde{\zeta}$ with $|\tilde{\zeta}| \leq \sqrt{\beta}$. Then $z = x(\xi,\tilde{\zeta}) + i\sqrt{\beta}y(\xi,\tilde{\zeta}) = x(\xi,\tilde{\zeta}) + i\tilde{y}(\xi,\tilde{\zeta})$ with $x$ and $\tilde{y}$ a pair of harmonic functions on $\Omega_w$.

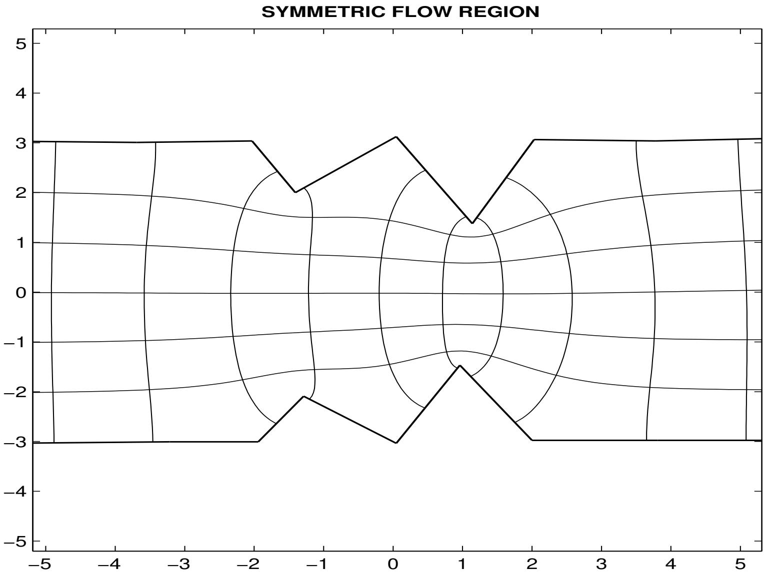


Figure 2.1: The symmetric domain in the complex $z$-plane, where $z = x(\xi,\tilde{\zeta}) + i\tilde{y}(\xi,\tilde{\zeta})$. The lower half ($x \in [-5,5], \quad y \in [-3,0]$) is the physical channel with $y = \tilde{\zeta} = 0$ indicating the undisturbed free surface. Superimposed in this complex $z$-plane domain are the (curvilinear) coordinate level curves from the $w$-plane system $\xi\tilde{\zeta}$. The polygonal line at the bottom of the figure is a schematic representation of the topography (where $\tilde{\zeta} = \pm\sqrt{\beta}$). This figure was generated using SC-Toolbox [18].

The scaled water wave equations in the fixed orthogonal curvilinear coordinates $(\xi, \tilde{\zeta})$ are:

$$\phi_{\xi\xi} \; + \; \phi_{\tilde{\zeta}\tilde{\zeta}} \; = \; 0, \qquad\qquad -\sqrt{\beta} < \tilde{\zeta} < \alpha\sqrt{\beta}N(\xi, t), \tag{2.3}$$

with free surface conditions

$$|J|N_t + \alpha\phi_\xi N_\xi - \frac{1}{\sqrt{\beta}}\phi_{\tilde{\zeta}} = 0 \tag{2.4}$$

and

$$\phi_t + \eta + \frac{\alpha}{2|J|}\left(\phi_\xi^2 + \phi_{\tilde{\zeta}}^2\right) = 0 \tag{2.5}$$

at $\tilde{\zeta} = \alpha\sqrt{\beta}N(\xi, t)$. The bottom condition (2.2) transforms into

$$\phi_{\tilde{\zeta}} = 0 \qquad \text{at} \;\; \tilde{\zeta} = -\sqrt{\beta}. \tag{2.6}$$

Here $N(\xi, t)$ denotes the position of the free surface in the new coordinate system and $|J|$ denotes the Jacobian of the change of coordinates,

$$|J| = x_\xi \tilde{y}_{\tilde{\zeta}} - \tilde{y}_\xi x_{\tilde{\zeta}} = \tilde{y}_{\tilde{\zeta}}^2 + \tilde{y}_\xi^2.$$

It is convenient to let the origin of the curvilinear coordinate system be at the bottom and define $\tilde{\zeta} = \sqrt{\beta}(\zeta - 1)$. In the system of coordinates $(\xi, \zeta)$, equations (2.3)-(2.6) transform into

$$\beta\phi_{\xi\xi} \; + \; \phi_{\zeta\zeta} \; = \; 0, \qquad \text{at} \;\; 0 < \zeta < 1 + \alpha N(\xi, t), \tag{2.7}$$

with free surface conditions

$$|J|N_t + \alpha\phi_\xi N_\xi - \frac{1}{\beta}\phi_\zeta = 0, \tag{2.8}$$

$$\eta + \phi_t + \frac{\alpha}{2|J|}\left(\phi_\xi^2 + \frac{1}{\beta}\phi_\zeta^2\right) = 0 \tag{2.9}$$

at $\zeta = 1 + \alpha N(\xi, t)$ and

$$\phi_\zeta = 0 \qquad \text{at} \;\; \zeta = 0. \tag{2.10}$$

As in Whitham [57], consider a power series expansion near the bottom of the channel in the form

$$\phi(\xi,\zeta,t) = \sum_{n=0}^{\infty} \zeta^n \; f_n(\xi,t). \tag{2.11}$$

Asymptotic analysis will be performed at the level of the equations in terms of the small parameters $\alpha$ and $\beta$.

By substituting this expression in the scaled Laplace equation (2.7) and the Newmann condition (2.10) at the bottom we can express the potential as a power expansion in $\beta$

$$\phi(\xi,\zeta,t) = \sum_{n=0}^{\infty} \frac{(-\beta)^n}{(2n)!} \zeta^{2n} \frac{\partial^{2n} f(\xi,t)}{\partial \xi^{2n}} \tag{2.12}$$

where, for simplicity, $f(\xi,t) = f_0(\xi,t)$.

Now using that at the smooth free surface $\tilde{\zeta}_{FS} = \alpha\sqrt{\beta}N(\xi,t)$ the Jacobian is

$$|J|(\xi,t) = \tilde{y}_\xi^2(\xi,\tilde{\zeta}_{FS}) + \tilde{y}_\zeta^2(\xi,\tilde{\zeta}_{FS}),$$

the Taylor polynomial formula leads to

$$|J|(\xi,t) = \tilde{y}_{\tilde{\zeta}}^2(\xi,0) + \alpha^2 R_J(\xi,\tilde{\zeta}_M) = M(\xi)^2 + O(\alpha^2), \quad 0 < |\tilde{\zeta}_M| < |\tilde{\zeta}_{FS}|. \tag{2.13}$$

Thus, the Jacobian can be well approximated by an $O(1)$ time independent coefficient. The time dependent correction term is $O(\alpha^2)$ due to the fact that the curvilinear coordinate system is symmetric about $\tilde{y} = \tilde{\zeta} = 0$. There are no $O(\alpha)$ terms. For the same reason, approximating $\tilde{\zeta}(x,\tilde{y}_{FS})$ in $\tilde{y}$ leads to

$$N(\xi,t) = \frac{1}{M(\xi)}\eta(x(\xi),t) + \alpha^2\beta R_N(\xi,\tilde{y}_M), \quad 0 < |\tilde{y}_M| < |\tilde{y}_{FS}|. \tag{2.14}$$

At the undisturbed level we define the **variable free surface coefficient**

$$M(\xi) \equiv \tilde{y}_{\tilde{\zeta}}(\xi,0) = 1 + m(\xi)$$

where

$$m(\xi;\sqrt{\beta},\gamma) \equiv \frac{\pi}{4\sqrt{\beta}} \int_{-\infty}^{\infty} \frac{n(x(\xi_0,-\sqrt{\beta})/\gamma)}{cosh^2 \frac{\pi}{2\sqrt{\beta}}(\xi_0-\xi)} d\xi_0 \;\; = \;\; (K*(n\circ x))(\xi). \tag{2.15}$$

Note that the coefficient $M(\xi)$ is smooth and time independent and becomes identically one in the case of a constant depth.

Therefore, by using the foregoing results, the free surface conditions (2.8)-(2.9) transform into

$$\eta + f_t - \frac{\beta}{2} f_{\xi\xi t} + \frac{\alpha}{2M^2(\xi)} f_\xi^2 = O(\alpha\beta, \beta^2), \tag{2.16}$$

$$M(\xi)\ \eta_t + \left[\left(1 + \frac{\alpha}{M(\xi)}\eta\right) f_\xi\right]_\xi - \frac{\beta}{6} f_{\xi\xi\xi\xi} = O(\alpha^2, \alpha\beta, \beta^2). \tag{2.17}$$

Remark that the variable coefficients result time independent and depend only on $\tilde{y}_\zeta(\xi, 0)$. This is a consequence of equations (2.13)-(2.14). Moreover, the transversal curvilinear coordinate $\zeta$ does not appear in the equations above.

As in Whitham [57] it is useful to work with a conveniently averaged velocity component. It can be shown that

$$\phi_\xi(\xi, \zeta_{FS}, t) = \tilde{u}(\xi, t) - \frac{\beta}{2}\zeta_{FS}^2 \tilde{u}_{\xi\xi}(\xi, t) + O(\beta^2),$$

where $\tilde{u} \equiv f_\xi$ is the "slip–velocity" along the bottom topography. In analogy with the $\sigma$–coordinates used in atmospheric flows [24], we call $\phi_\xi$ the terrain–following velocity component [15]. Its transversal average (along a $\xi$ level-curve) is defined as

$$u(\xi, t) \equiv \frac{1}{\zeta_{FS}} \int_0^{\zeta_{FS}} \phi_\xi(\xi, \zeta, t) d\zeta. \tag{2.18}$$

In the physical space this integral represents a weighted average of the terrain-following velocity components. Therefore using the potential's power series representation

$$u(\xi, t) = \sum_{n=0}^{\infty} \frac{(-\beta)^n}{(2n)!} \left[\frac{1}{\zeta_{FS}} \int_0^{\zeta_{FS}} \zeta^{2n} d\zeta\right] \frac{\partial^{2n+1} f(\xi, t)}{\partial \xi^{2n+1}} = \tilde{u} - \frac{\beta}{6}\tilde{u}_{\xi\xi} + O(\alpha\beta, \beta^2).$$

Differentiating the first free surface condition (2.16) with respect to $\xi$ and substituting for depth–averaged velocity through the expansion

$$\tilde{u} = u + \frac{\beta}{6} u_{\xi\xi} + O(\alpha\beta, \beta^2),$$

in the resulting equation and in equation (2.17), we arrive (retaining the terms of order $\alpha$, $\beta$) at the terrain-following Boussinesq system (2.1). Further details can be found in [45].

We remark that this Boussinesq system is valid for arbitrary orographies provided that the parameters $\alpha$ and $\beta$ be small. Furthermore, the physical orography (opposite to other Boussinesq models [51], [37]) was replaced by the metric coefficient $M(\xi)$ which is smooth even when the orography has singularities. This important property makes system (2.1) appropriate for modelling the problem we are interested in. We will explore some numerical properties of this system in Chapter 5.

## 2.2 The linear Boussinesq system and initial conditions

In this work, system (2.1) is adopted as the model for dispersive waves propagating over a section of a coastal region, here modelled as a one-dimensional shallow channel. As mentioned earlier, we focus our attention on the case where the ratio irregularities/wavelength is small (See Figure 2.2). Further, the total length of the irregular section is taken large enough so that the effect of the depth fluctuations be appreciable. We do not assume the amplitude of the fluctuations to be small.

System (2.1) is complemented with the initial conditions

$$\eta(\xi, 0) = u(\xi, 0) = g(\xi), \tag{2.19}$$

describing the initial disturbances (in space) considered. Function $g$ is smooth and to guarantee that at the starting time the incoming pulse $g$ does not interact with the orography, we assume that it is effectively supported in a compact subset of the interval $(-\infty, 0)$.

In the numerical validation of our theory, we consider the particular cases of Gaussian-shaped pulses and solitary wave solutions of system (2.1). These type of pulses are usual and important in applications of Fluid Dynamics. For instance, they can be used as simple models for a tsunami-type disturbance. Other profiles could be considered as long as they are smooth and localized in space (i.e. decaying exponentially fast).

Of particular interest in our study is the system

$$\begin{aligned} M(\xi)\eta_t + u_\xi &= 0, \\ u_t + \eta_\xi - \frac{\beta}{3} u_{\xi\xi t} &= 0, \end{aligned} \tag{2.20}$$

which is the linearization of equations (2.1) ($\alpha = 0$). We remark that when $\beta = 0$, model (2.20) reduces to a hyperbolic system which is analogous to the model for acoustic waves studied, for instance in [9], [12] and [16].

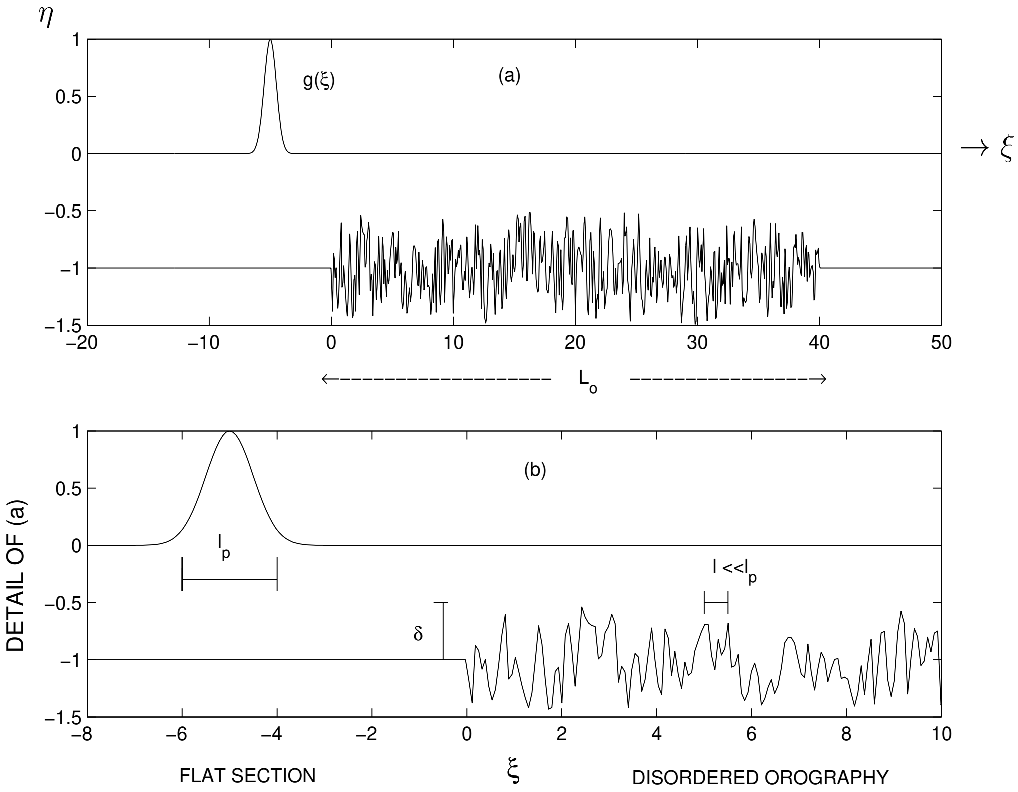


Figure 2.2: Geometry of the problem. The initial disturbance $g(\xi)$ is incoming from the left of the disordered orography. The depth vary rapidly which means that the ratio irregularities/ wavelength is taken to be small ($\ell << \ell_p$). The orography's fluctuations cover an interval of length $L_o >> \ell_p$. Outside this interval the bottom is assumed to be flat. The parameter $0 < \delta < 1$ measures the amplitude of the fluctuations.

We will generalize the O'Doherty-Anstey approximation (ODA) from linear acoustic waves to the linear weakly-dispersive system (2.20) when forced by a rapidly varying orography expressed through the coefficient $M(\xi)$.

The technique analogous to L. Berlyand and R. Burridge's work [9] is applied successfully due to two reasons. First, system (2.20) can be written equivalently as two coupled KdV-type equations for the transmitted and reflected fields. These linearized KdV-type equations can be viewed as a dispersive perturbation to those obtained in [9]. Namely a propagating pulse will slowly disperse with a given (known) rate (c.f. Appendix A, equation (A.6) or equation (C.3)). Second, the pulse's effective propagation velocity is bounded and all Fourier modes have positive phase speeds bounded by 1 (c.f. equation (A.11)). These two properties allow us to apply the **invariant imbedding approach** (see Appendix B), taking the propagation distance as the **imbedding parameter**.

In what follows, solutions $u, \eta$ to (2.20) will be assumed to be smooth enough and absolutely integrable. This requirement is necessary to justify the use of the Fourier transform and the Fourier inversion formula.

## 2.3 Transformed variables and splitting

We will introduce convenient changes of variables in order to study the propagation of waves in a variable medium. In terms of the new variables considered, the Boussinesq system (2.20) will be expressed as a pair of coupled linear KdV-type equations with variable coefficients describing the properties of the medium. In absence of dispersion ($\beta = 0$) this system reduces to a hyperbolic system as in [9].

We start by performing the change of variable

$$x = \int_0^{\xi} \frac{1}{C_o(s)} ds, \tag{2.21}$$

into system (2.20). Here $C_o(s) = \sqrt{\frac{1}{M(s)}}$ is the **local characteristic speed** and $x$ the **wave travel time**. Due to relationship (2.21) we also refer to variable $x$ as "propagation distance" or "medium position". The variable $x$ is a function of the medium's position $\xi$ and measures the time for the wave travelling up to the position $\xi$. Further, we remark that the quantity $C_o(\xi)$ measures the velocity of propagation of the wave at the point of medium $\xi$, in contrast to the weighted average velocity $u(\xi, t)$ of the fluid particles defined by equation (2.18) above.

System (2.20) become

$$C_o^{-1/2}\ \eta_t + C_o^{1/2}\ u_x = 0, \tag{2.22}$$
$$C_o^{1/2}\ u_t + C_o^{-1/2}\ \eta_x - \frac{\beta}{3C_o^{1/2}}\left(u_{xxt}\ \frac{1}{C_o} + \left(\frac{1}{C_o}\right)_x u_{xt}\right) = 0.$$

Instead of looking at the velocity and wave elevation fields, it is convenient to introduce the **wave mode splitting**

$$R = C_o^{1/2}u + C_o^{-1/2}\eta, \tag{2.23}$$
$$L = -C_o^{1/2}u + C_o^{-1/2}\eta. \tag{2.24}$$

The new fields $R$ and $L$ will be the quantities of interest in this work. The approximation to be derived accounts for the shape of the wave mode $R$.

Differentiating (2.23) with respect to $x$ and $t$ leads to

$$\begin{aligned} R_t + R_x &= C_o^{1/2}u_t + C_o^{-1/2}\eta_t + \frac{1}{2}C_o^{-1/2}C_{o,x}u + C_o^{1/2}u_x + \\ &\quad C_o^{-1/2}\eta_x - \frac{1}{2}C_o^{-3/2}C_{o,x}\eta. \end{aligned} \tag{2.25}$$

Then on using (2.22), equation (2.25) becomes

$$R_t + R_x = \frac{\beta}{3C_o^{3/2}}u_{xxt} - \frac{\beta C_{o,x}}{3C_o^{5/2}}u_{xt} - rL. \tag{2.26}$$

In a similar fashion,

$$L_x - L_t = \frac{\beta}{3C_o^{3/2}}u_{xxt} - \frac{\beta C_{o,x}}{3C_o^{5/2}}u_{xt} - rR. \tag{2.27}$$

Notice that quantities $R$ and $L$ correspond to the Riemann invariants (that is, preserved along characteristic curves) of system (2.20) in the homogeneous, nondispersive regime ($\beta = 0, C_o \equiv 1$).

Now, using that $u = (R-L)/(2C_o^{1/2})$ in (2.26) and (2.27), we obtain the coupled wave-mode system

$$
\begin{aligned}
R_t + R_x &= p(x)\left(\frac{R-L}{2C_o^{1/2}}\right)_{xxt} + q(x)\left(\frac{R-L}{2C_o^{1/2}}\right)_{xt} - r(x)L, \\
L_x - L_t &= p(x)\left(\frac{R-L}{2C_o^{1/2}}\right)_{xxt} + q(x)\left(\frac{R-L}{2C_o^{1/2}}\right)_{xt} - r(x)R,
\end{aligned}
\tag{2.28}
$$

where

$$
p(x) = \frac{\beta}{3C_o^{3/2}(x)}, \quad q(x) = -\frac{\beta C_{o,x}(x)}{3C_o^{5/2}(x)}, \quad \text{and} \quad r(x) = \frac{C_{o,x}(x)}{2C_o(x)}.
$$

System (2.28) is the pair of KdV-type equations mentioned earlier. This representation is equivalent to the original Boussinesq system (2.20) because no approximations are involved.

From (2.19), appropriate initial conditions for system (2.28) are

$$
R(x,0) = R_o(x), \quad L(x,0) = 0, \tag{2.29}
$$

where $R_o$ is a function effectively supported in a compact set.

### 2.3.1 Physical meaning of splitting

Observe that when the bottom is flat ($M \equiv 1$ or equivalently $r \equiv 0$) and $\beta = 0$ (no dispersion), equations (2.28) decouple indicating that we may identify $R$ with a wave propagating to the right (**transmitted wave**) and $L$ with a wave propagating to the left (**reflected wave**). For variable depths we adopt the same terminology motivated by the above observation. This terminology is consistent in the weakly-dispersive regime ($0 < \beta << 1$) and at constant depth since in this case the left propagating signal $L$ is negligible for all time $t$ since the initial data for $\eta$ and $u$ correspond to a rightgoing wave (see initial conditions (2.19) and Appendix A ).

Several decompositions of the Boussinesq equations into a pair of KdV equations are introduced by F. Mattioli in [38] and [39]. We point out that the new representation (2.28) proposed here has some advantages with respect to those presented by Mattioli. First, unlike system (2.28), the Boussinesq-type equations used by Mattioli are not valid as an asymptotic approximation of the potential theory equations for arbitrary rapidly-varying or non-differentiable orographies. Second, in contrast to system (2.28), the linear dispersion relation for Mattioli's model results in instable short waves with amplitude tending to infinity (see Appendix F).

## 2.4 Transmitted and reflected wave mode equations

In this section we show that in the Fourier domain, the transmitted and reflected fields satisfy a system of coupled linear ordinary differential equations with variable coefficients. The analysis of this system through the invariant imbedding technique within a medium slab will lead to the pulse-shape approximation for dispersive waves to be presented in Section 2.6.

In order to set our forthcoming results in a wave propagating frame let us introduce the change of variables

$$\tau = t - x,$$

Notice that the time-delay variable $\tau$ can be fixed at an arbitrary value in contrast to the real ("clock") time variable $t$. This advantage will be useful in the theory. The quantity $\tau$ measures the time with respect to the first arrival of the signal at a selected station in the medium. Equations (2.28) are transformed into

$$\begin{aligned}
R_x &= p\left(\frac{R-L}{2C_o^{1/2}}\right)_{\tau\tau\tau} - 2p\left(\frac{R-L}{2C_o^{1/2}}\right)_{x\tau\tau} + p\left(\frac{R-L}{2C_o^{1/2}}\right)_{xx\tau} \\
&\quad -q\left(\frac{R-L}{2C_o^{1/2}}\right)_{\tau\tau} + q\left(\frac{R-L}{2C_o^{1/2}}\right)_{x\tau} - rL, \\
L_x - 2L_\tau &= p\left(\frac{R-L}{2C_o^{1/2}}\right)_{\tau\tau\tau} - 2p\left(\frac{R-L}{2C_o^{1/2}}\right)_{x\tau\tau} + p\left(\frac{R-L}{2C_o^{1/2}}\right)_{xx\tau} \\
&\quad -q\left(\frac{R-L}{2C_o^{1/2}}\right)_{\tau\tau} + q\left(\frac{R-L}{2C_o^{1/2}}\right)_{x\tau} - rR.
\end{aligned} \tag{2.30}$$

The fact that all variable coefficients in the linear system (2.30) are time independent enables us to employ the Fourier transform strategy in time. Let $\widehat{f}(\omega)$ denote the Fourier Transform of $f(\tau)$ in the time-delay variable $\tau$ :

$$\widehat{f}(\omega) = \int_{-\infty}^{\infty} e^{-i\omega\tau} f(\tau)\, d\tau.$$

Then, taking Fourier Transform in $\tau$ of equations (2.30), we obtain

$$\begin{aligned}\widehat{R}_x &= -pi\omega^3\left(\frac{\widehat{R}-\widehat{L}}{2C_o^{1/2}}\right)+2p\omega^2\left(\frac{\widehat{R}-\widehat{L}}{2C_o^{1/2}}\right)_x+pi\omega\left(\frac{\widehat{R}-\widehat{L}}{2C_o^{1/2}}\right)_{xx} \\ &\quad +q\omega^2\left(\frac{\widehat{R}-\widehat{L}}{2C_o^{1/2}}\right)+qi\omega\left(\frac{\widehat{R}-\widehat{L}}{2C_o^{1/2}}\right)_x-r\widehat{L},\end{aligned} \tag{2.31}$$

$$\begin{aligned}\widehat{L}_x-2i\omega\widehat{L} &= -pi\omega^3\left(\frac{\widehat{R}-\widehat{L}}{2C_o^{1/2}}\right)+2p\omega^2\left(\frac{\widehat{R}-\widehat{L}}{2C_o^{1/2}}\right)_x+pi\omega\left(\frac{\widehat{R}-\widehat{L}}{2C_o^{1/2}}\right)_{xx} \\ &\quad +q\omega^2\left(\frac{\widehat{R}-\widehat{L}}{2C_o^{1/2}}\right)+qi\omega\left(\frac{\widehat{R}-\widehat{L}}{2C_o^{1/2}}\right)_x-r\widehat{R}.\end{aligned} \tag{2.32}$$

Equations (2.31)-(2.32) imply that

$$\widehat{R}_x-\widehat{L}_x=r\widehat{R}-2i\omega\widehat{L}-r\widehat{L}. \tag{2.33}$$

Expanding the $x$ derivatives in equation (2.31), we obtain

$$\begin{aligned}&\widehat{R}_x=(-piw^3+qw^2)\left(\frac{\widehat{R}-\widehat{L}}{2C_o^{1/2}}\right)+(2pw^2+qiw)\left((\widehat{R}-\widehat{L})\left(\frac{1}{2C_o^{1/2}}\right)_x+\right. \\ &\left.(\widehat{R}-\widehat{L})_x\left(\frac{1}{2C_o^{1/2}}\right)\right)+piw\left((\widehat{R}-\widehat{L})_x\left(\frac{1}{2C_o^{1/2}}\right)_x+(\widehat{R}-\widehat{L})\left(\frac{1}{2C_o^{1/2}}\right)_{xx}\right. \\ &\left.+(\widehat{R}-\widehat{L})_{xx}\left(\frac{1}{2C_o^{1/2}}\right)+(\widehat{R}-\widehat{L})_x\left(\frac{1}{2C_o^{1/2}}\right)_x\right)-r\widehat{L}.\end{aligned} \tag{2.34}$$

On the other hand, by differentiating equation (2.33) with respect to $x$, we find

$$\begin{aligned}\widehat{R}_{xx}-\widehat{L}_{xx} &= r'(x)\widehat{R}-r'(x)\widehat{L}-2iw\widehat{R}_x+2iwr(x)\widehat{R} \\ &\quad +4w^2\widehat{L}-4iwr(x)\widehat{L}+r^2(x)\widehat{R}-r^2(x)\widehat{L}.\end{aligned} \tag{2.35}$$

Now denote $d(x)=\beta/(3C_o^2(x))$. In the present analysis it is sufficient to consider a bounded frequency range $|\omega|<\omega_o<\sqrt{3/\beta}$. The bound $\sqrt{3/\beta}$ arises from equation (A.10) in Appendix A. Hence, we can substitute equation (2.35) into equation (2.34) and solve for $\widehat{R}_x$ to obtain

$$\widehat{R}_x = \zeta(x,\omega)\widehat{L} + \gamma(x,\omega)\widehat{R}, \tag{2.36}$$

where

$$\zeta(x,\omega) = \frac{id(x)\omega^3 - 2r(x)d(x)\omega^2 - 2r(x)}{2(1-d(x)\ \omega^2)} \quad \text{and} \quad \gamma(x,\omega) = \frac{-id(x)\omega^3 - 4r(x)d(x)\omega^2}{2(1-d(x)\omega^2)}.$$

Note that $\gamma(x,\omega)$ can be rewritten as

$$\gamma(x,\omega) = \frac{-i\beta\omega^2(\omega - 4ir(x))}{2(3C_o^2(x) - \beta\omega^2)}$$

to make evident the role of dispersion and orography within this quantity. In particular, notice that at constant depth it is space independent and reduces to $\gamma(\omega) = -i\beta\omega^3/(6(1-(\beta/3)\omega^2))$ which controls the Airy function "mechanism" as seen in equations (C.2) and (C.3) (Appendix C).

Putting equation (2.36) into equation (2.33) and solving for $\widehat{L}_x$, it becomes

$$\widehat{L}_x = (2i\omega + \bar{\gamma}(x,\omega))\widehat{L} + \bar{\zeta}(x,\omega)\widehat{R}, \tag{2.37}$$

where $\bar{\zeta}(x,w)$ and $\bar{\gamma}(x,w)$ denote the complex conjugates of $\zeta(x,w)$ and $\gamma(x,w)$, respectively. The system of ordinary differential equations (2.36) and (2.37) gives the evolution in $x$ (the wave travel time) of each Fourier mode of the transmitted and reflected fields. This is a crucial step in order to apply the **invariant imbedding technique** (see Appendix B).

Given the incoming signal $f(\tau)$ at the origin $\xi = 0$, we are interested in calculating the transmitted field $R(x_o, \tau)$ over the finite time interval $0 < \tau < T$. In this connection the invariant imbedding approach proves to be useful. To this effect we consider system (2.36) and (2.37) restricted to a disordered medium slab, say $[x_o, x_o + X]$ (see Figure 2.3). Here, instead of looking for the interior values of $R$ and $L$ we put our attention into their incoming and outcome values across the borders of the slab. To proceed, it is necessary to note that the disordered medium covering the interval $[x_o + X, \infty)$ can not be "felt" at the current observation station $x_o$ (over the finite time interval $0 < \tau = t - x_o < T$), since the signal did not have enough time to go beyond $x_o + X$ and return to $x_o$. This is true for $X > 0$ large enough (depending on $T$) due to the bounded (effective) wave propagation speed mentioned earlier. Thus, we can imbed the relevant medium slab into another medium (homogeneous at $x > x_o + X$) so that the boundary conditions

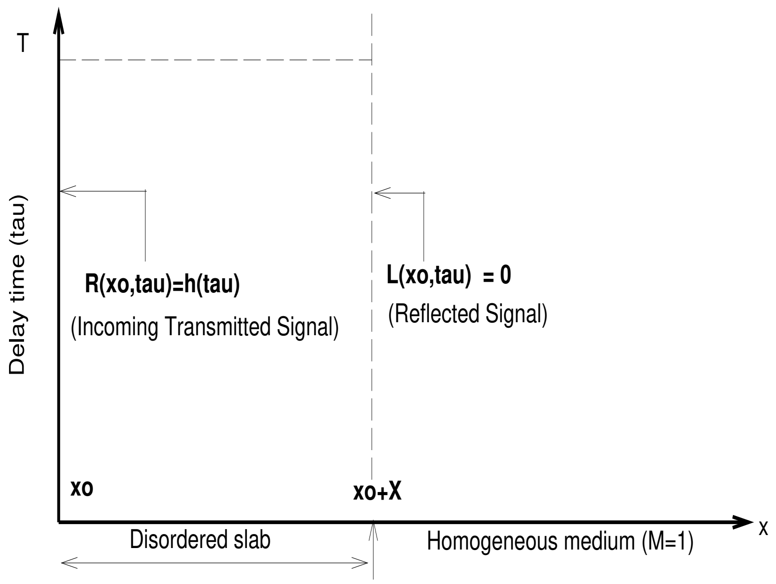


Figure 2.3: Invariant imbedding slab. System (2.36) and (2.37) subject to boundary conditions (2.38) and (2.39) is solved on the interval $[x_o, x_o + X]$.

$$\widehat{R}(x_o, \omega; T) = \widehat{h}(\omega), \tag{2.38}$$

$$\widehat{L}(x_o + X, \omega; T) = 0 \tag{2.39}$$

can be imposed.

In the modified medium, equation (2.39) can be considered as a radiation condition which means that no reflection is expected at the downstream travel time location $x_o$. Remember the definition of the wave travel time in equation (2.21) above.

Now, linearity of system (2.36)-(2.37) leads to the invariant imbedding representation (see Appendix B)

$$\widehat{L}(x, \omega; T) = \widehat{K}(x, \omega; T)\ \widehat{R}(x, \omega; T), \tag{2.40}$$

where $\widehat{K}(x, \omega; T)$ (**the reflection coefficient**) satisfies the Riccati equation

$$\widehat{K}_x = \bar{\zeta}(x, \omega) + 2i\omega\Gamma(x, \omega)\widehat{K} - \zeta(x, \omega)\widehat{K}^2, \tag{2.41}$$

with

$$\Gamma(x,\omega) = \frac{2 - d(x)\omega^2}{2(1 - d(x)\omega^2)}.$$

Note that $\widehat{K}(x,-\omega) = \overline{\widehat{K}(x,\omega)}$. Further, in the physical domain equation (2.40) reads

$$L(x,\tau;T) = \int K(x,\tau - y;T)R(x,y;T)dy. \tag{2.42}$$

For this reason, function $K(x,\tau;T)$ is called **the reflection kernel**. Note that the Fourier transform of this kernel is the reflection coefficient satisfying the Riccati equation (2.41).

From equation (2.39) we obtain an appropriate initial condition for equation (2.41), namely

$$\widehat{K}(x_o + X, \omega; T) = 0. \tag{2.43}$$

Notice that equation (2.42) allows us to solve for the reflected signal $L(x_o,\tau;T)$ in terms of the reflection kernel $K(x_o,\tau;T)$ and the transmitted pulse $R(x_o,\tau;T)$ for $0 \leq \tau \leq T$. This function $K$ contains all the information about the medium's reflection properties. We also remark that the boundary value problem (2.36), (2.37), (2.38), (2.39) has been reduced to solving the initial problem value (2.41)-(2.43) in reversed direction up to the medium station $x_o$. This is an aspect of the invariant imbedding approach which has important theoretical and numerical applications. Further, it has connection with the shooting method to solve boundary value problems (see details in Appendix B and references therein).

## 2.5 Analysis of the Riccati equation

In general, it is not possible to solve explicitly for $\widehat{K}$ from equation (2.41), so we adopt an approximation. To this end, we need the following generalization to Berlyand and Burridge's lemma [9]. This is a Gronwall-type result providing an useful decomposition for the solution of the initial problem value (2.41)-(2.43). In this section, by applying this lemma, an accurate approximation for the reflection coefficient $\widehat{K}$ and an estimate for the error committed will be derived. These results will be used in Section 2.6 to derive the approximation for the pulse shape of dispersive waves propagating in highly disordered media.

**Lemma.** Let $y$ satisfy the Riccati equation

$$y'(s) = -A(s) - 2i\omega B(s)y(s) + \bar{A}(s)y^2(s), \quad 0 \leq s \leq s_o, \tag{2.44}$$

subject to the initial condition

$$y(0) = 0.$$

Here $\bar{A}(s)$ denotes the complex conjugate of $A(s)$. Set

$$v(s_o) = \sup_{0 \leq s \leq s_o} \left| \int_0^s e^{2iw \int_0^{s'} B(\xi)d\xi} A(s')ds' \right|,$$

and

$$V(s) = \int_0^s |A(s')|\, ds'.$$

It follows that

$$y(s_o) = -\int_0^{s_o} e^{-2i\omega \int_{s'}^{s_o} B(\xi)d\xi} A(s')ds' + E(s_o), \tag{2.45}$$

where

$$E(s_o) = \int_0^{s_o} \bar{A}(s')e^{-2i\omega \int_{s'}^{s_o} B(\xi)d\xi} y^2(s')ds'.$$

Moreover, if $v(s_o)V(s) < 1$

$$|E(s)| \leq \frac{v^2(s_o)V(s)}{1 - v(s_o)V(s)}, \quad 0 \leq s \leq s_o. \tag{2.46}$$

**Proof :**
Multiplying equation (2.44) by its integrating factor and integrating both sides from 0 to $s$, yields that

$$\int_0^s e^{2i\omega \int_0^{s'} B(\xi)d\xi} y'(s')ds' + 2iw \int_0^s B(s')e^{2i\omega \int_0^{s'} B(\xi)d\xi} y(s')ds' =$$
$$-\int_0^s e^{2iw \int_0^{s'} B(\xi)d\xi} A(s')ds' + \int_0^s \bar{A}(s')e^{2i\omega \int_0^{s'} B(\xi)d\xi} y^2(s')ds'.$$

Consequently,

$$\int_0^s \frac{d}{ds'}\left(e^{2i\omega\int_0^{s'} B(\xi)d\xi} y(s')\right) ds' = e^{2i\omega\int_0^{s} B(\xi)d\xi} y(s)$$
$$= -\int_0^s e^{2i\omega\int_0^{s'} B(\xi)d\xi} A(s')ds' + \int_0^s \bar{A}(s') e^{2i\omega\int_0^{s'} B(\xi)d\xi} y^2(s')ds'. \tag{2.47}$$

Now, solving for $y(s)$ and evaluating at $s = s_o$ in equation (2.47) we arrive at equation (2.45).

To achieve the estimate (2.46), we start with

$$\begin{aligned} E(s) &= \int_0^s \bar{A}(s') e^{-2i\omega\int_{s'}^{s} B(\xi)d\xi} y^2(s')ds' \\ &= e^{-2i\omega\int_0^{s} B(\xi)d\xi} \int_0^s \bar{A}(s') e^{2i\omega\int_0^{s'} B(\xi)d\xi} y^2(s')ds'. \end{aligned}$$

Introducing

$$Y(s) = \int_0^s |A(s')| \, |y(s')|^2 \, ds', \tag{2.48}$$

we find that

$$|E(s)| = \left| \int_0^s \bar{A}(s') e^{2i\omega\int_0^{s'} B(\xi)d\xi} y^2(s')ds' \right| \leq Y(s). \tag{2.49}$$

Differentiate equation (2.48) with respect to $s$ to get

$$Y'(s) = |A(s)| \, |y(s)|^2 . \tag{2.50}$$

Note that from equations (2.45) and (2.49)

$$|y(s)| \leq v(s_o) + Y(s), \quad 0 \leq s \leq s_o. \tag{2.51}$$

Thus, substituting equation (2.51) into (2.50) leads to

$$Y'(s) \leq |A(s)| \, (v(s_o) + Y(s))^2. \tag{2.52}$$

By integrating equation (2.52) from 0 to $s$, we obtain

$$\int_0^s \frac{Y'(s)}{(v(s_o)+Y(s'))^2}ds' \leq \int_0^s |A(s')|\, ds' = V(s).$$

Therefore,

$$\frac{1}{v(s_o)} - \frac{1}{v(s_o)+Y(s)} \leq V(s).$$

Thus, if $v(s_o)V(s) < 1$, we have

$$Y(s) \leq \frac{v^2(s_o)V(s)}{1 - v(s_o)V(s)}.$$

Finally, because of equation (2.49),

$$|E(s)| \leq Y(s) \leq \frac{v^2(s_o)V(s)}{1 - v(s_o)V(s)}, \quad 0 \leq s \leq s_o.$$

This concludes the lemma's proof.

$\square$

For brevity, the argument $T$ will be omitted in what follows. Notice that, due to equation (2.41), the Fourier transform of the reflection kernel, $\widehat{K}$, satisfies an ordinary differential equation analogous to equation (2.44) for $y(s)$. For this reason, we may apply, the above lemma to problem (2.41) - (2.43) if we consider

$$\begin{aligned}
&A(s) = \bar{\zeta}(x(s), \omega), \\
&B(s) = \Gamma(x(s), \omega), \\
&s = x_o + X - x, \\
&s_o = X, \\
&y(s) = \widehat{K}(x(s), \omega).
\end{aligned}$$

In this way, at the slab's border $x_o$ we have that

$$\widehat{K}(x_o, \omega) = -\int_{x_o}^{x_o+X} e^{2i\omega \int_{x'}^{x_o} \Gamma(s,\omega)\, ds} \bar{\zeta}(x', \omega) dx' + E(x_o, \omega), \tag{2.53}$$

where

$$E(x_o,\omega) = \int_{x_o}^{x_o+X} e^{2i\omega\int_{x'}^{x_o}\Gamma(s,\omega)\,ds}\zeta(x',\omega)\widehat{K}^2(x',\omega)dx'.$$

Also

$$v(x_o,\omega) = \sup_{x_o\le x\le x_o+X}\left|\int_{x}^{x_o+X} e^{2i\omega\int_{x'}^{x_o+X}\Gamma(s,\omega)\,ds}\bar{\zeta}(x',\omega)dx'\right|$$

and

$$V(x_o,\omega) = \int_{x_o}^{x_o+X} |\zeta(x',\omega)|\ dx'.$$

Then, if $v(x_o,\omega)V(x_o,\omega) < 1$ we have

$$|E(x_o,\omega)| \le \frac{v^2(x_o,\omega)V(x_o,\omega)}{1-v(x_o,\omega)V(x_o,\omega)}. \tag{2.54}$$

For rapidly varying orographies and $\beta << 1$ the function $E(x,\omega)$ is small compared to the right-side term in the decomposition (2.53) (see Appendix E), even though estimate (2.54) is not sharp. Thus, it is reasonable to adopt the linear approximation

$$\widehat{K}(x_o,\omega) \approx -\int_{x_o}^{x_o+X} e^{2i\omega\int_{x'}^{x_o}\Gamma(s,\omega)\,ds}\bar{\zeta}(x',\omega)dx'. \tag{2.55}$$

Notice that the approximation (2.55) furnishes an **explicit formula** for the reflection coefficient $\widehat{K}$ which depends only on the medium's information inside the interval $[x_o, x_o+X]$.

## 2.6 Main result

In this section we arrive at a deterministic approximation for the shape the transmitted field $R(x_o,\tau)$ at an arbitrary point $x_o$. The main ingredient in the analysis is the lemma presented in Section 2.5. This is our main result in this chapter. The estimate to be presented gives a complete characterization for the pulse-shape mechanism in the presence of dispersion for arbitrary depths. With the help of this result, we will analyze the role of the model's dispersion on the shape of the transmitted signal propagating over a depth with small-scale inhomogeneities. We assume that the initial disturbance in time $f$ is smooth and that its Fourier transform $\hat{f}$ is supported in the interval $(-\sqrt{3/\beta}, \sqrt{3/\beta})$.

### 2.6.1 The generalized O'Doherty-Anstey approximation

By using equations (2.53) and (2.40) into equation (2.36), it results that

$$\widehat{R}_x(x,\omega) = \left(\zeta(x,\omega)\left(-\int_x^{x+X} e^{2i\omega\int_{x'}^{x}\Gamma(s,\omega)\,ds}\bar{\zeta}(x',\omega)dx' + E(x,\omega)\right) + \gamma\right)\ \widehat{R}(x,\omega).$$

Now, if $\widehat{R}(0,\omega) = \widehat{f}(\omega)$, then

$$\begin{aligned}\widehat{R}(x_o,\omega) \;&=\; \widehat{f}(\omega)\ \exp\left[\int_0^{x_o}\left(-\int_x^{x+X}\zeta(x,\omega)e^{2i\omega\int_{x'}^{x}\Gamma(s,\omega)\,ds}\ \bar{\zeta}(x',\omega)dx' + \gamma(x,\omega)\right)dx\right]\\ &\quad\cdot\exp\left[\int_0^{x_o}\zeta(x,\omega)\ E(x,\omega)\,dx\right].\end{aligned} \tag{2.56}$$

As mentioned before, in our applications the function $E(x_o,\omega)$ is small and thus, equation (2.56) and approximation (2.55) lead to the **generalized O'Doherty-Anstey approximation**

$$\widehat{R}(x_o,\omega) \approx \widehat{f}(\omega)e^{-x_o(a_\beta(x_o,\omega)+b(x_o,\omega))}, \tag{2.57}$$

where

$$a_\beta(x_o,\omega) \;=\; \frac{1}{x_o}\int_0^{x_o}\int_x^{x+X}\zeta(x,\omega)e^{2i\omega\int_{x'}^{x}\Gamma(s,\omega)\,ds}\bar{\zeta}(x',\omega)dx'\,dx, \tag{2.58}$$

$$b(x_o,\omega) \;=\; -\frac{1}{x_o}\int_0^{x_o}\gamma(x,\omega)\,dx. \tag{2.59}$$

From approximation (2.57) we can estimate $R(x_o,\tau)$ (the transmitted field) by using the Fourier inversion formula. Thus, for $0 \le \tau \le T$, we find

$$R(x_o,\tau) \approx \frac{1}{2\pi}\int_{-\omega_o}^{\omega_o}\widehat{f}(\omega)e^{-x_o(a_\beta(\omega)+b(\omega))}e^{i\omega\tau}d\omega, \tag{2.60}$$

where $\omega_o \le \sqrt{3/\beta}$ is such that the integrand in (2.60) is well-defined. As mentioned earlier, the bound $\sqrt{3/\beta}$ arises from the dispersion relation (A.10) in Appendix A.

Note that the exponential factor in equation (2.60) accounts for the wave attenuation at $x_o$. This will be analyzed in detail in Section 2.7. Equation (2.54) gives us an error estimate in making this approximation.

From equation (C.1) (in Appendix C) we see that, for a constant depth, the dispersive medium's correlation function $a_\beta(x_o, \omega)$ is roughly of $O(\beta^2)$ being dominated by the dispersive coefficient $b(x_o, \omega)$ which is of $O(\beta)$. Thus, for variable depth it is reasonable to neglect dispersive effects in the coefficient $a_\beta(x_o, \omega)$ and approximate it by the hyperbolic medium's correlation function $a_0(x_o, \omega)$, its leading order term in a Taylor series around $\beta = 0$. In other words,

$$a_\beta(x_o, \omega) \approx \frac{1}{x_o} \int_0^{x_o} \int_x^{x+X} r(x) e^{2i\omega(x-x')} r(x') dx' \, dx = a_0(x_o, \omega), \tag{2.61}$$

which is easier to compute than the original formula (2.58). The reason is that (2.58) cannot be computed by using the FFT (Fast Fourier Transform) since the function $\zeta$ in the integrand depends on the frequency $\omega$. On the other hand, in equation (2.61) the coefficient $r(x)$ is frequency independent and the FFT algorithm applies directly (see details in Appendix D).

The accuracy of estimate (2.61) will be verified in Sections 3.2 and 3.3 showing that leading order dispersive effects are controlled by coefficient $b(x_o, \omega)$. Our numerical experiments will also show that approximation (2.60) captures very well not only the wave front but also part of the forward scattering radiation. Moreover, the parameter $X$ in equation (2.58) or (2.61) regulates to what extent the signal is recovered. Recall that $X$ is the disordered slab's width in the invariant imbedding procedure.

If $\beta = 0$, then $b(x_o, \omega) \equiv 0$ and the approximation given by (2.57) reduces to

$$\widehat{R}(x_o, \omega) \approx \widehat{f}(\omega) e^{-x_o a_0(x_o, \omega)}, \tag{2.62}$$

where

$$a_0(x_o, \omega) = \frac{1}{x_o} \int_0^{x_o} \int_x^{x+X} r(x) e^{2i\omega(x-x')} r(x') dx' \, dx,$$

as in Berlyand and Burridge's work [9]. If $\beta \neq 0$ we observe that the hyperbolic medium's correlation function $a_0(x_o, \omega)$, which controls the attenuation mechanism, is altered and an extra term $b(x_o, \omega)$ appears due to the model's dispersion.

In the case of constant depth, we can verify directly the consistency of approximation (2.60) because system (2.28) can be approximated by a decoupled system for the right and left propagating pulses which can be solved explicitly (see Appendix C for details).

We get interesting conservation of energy information by considering the initial value problem (2.41)-(2.43) at frequency $\omega = 0$. In this particular case, it can be solved **exactly** for the reflection kernel in an arbitrary interval $[x, x + X]$ giving that

$$\widehat{K}(x,0) = \frac{e^{2\int_x^{x+X} r(s)ds} - 1}{1 + e^{2\int_x^{x+X} r(s)ds}}. \tag{2.63}$$

Note that in such a case $\widehat{K}(x,0)$ is real. Now, if we take the length of the invariant imbedding slab larger than the total length of the orography's irregular section, that is $X > L_o$, equation (2.63) reduces into

$$\widehat{K}(x,0) = \frac{1 - C_o(x)}{1 + C_o(x)}. \tag{2.64}$$

Recall that the medium's irregularities are located over an interval $[0, L_o]$ and outside this interval the bottom is flat, that is $C_o \equiv M \equiv 1$. Furthermore at the irregular medium's ends we have that $C_o(0) = C_o(L_o) = 1$.

Substituting the exact formula (2.64) into equation (2.36), using (2.40) and integrating with respect to $x$ on interval $[0, x_o]$, yields that

$$\begin{aligned} \widehat{R}(x_o,0) &= \hat{f}(0) \exp\left[-\int_0^{x_o} \frac{C_{o,x}(x)}{2C_o(x)} \left(\frac{1 - C_o(x)}{1 + C_o(x)}\right) dx\right], \\ \widehat{R}(x_o,0) &= \int R(x_o,\tau) d\tau = P(x_o) \int f(\tau) d\tau, \end{aligned} \tag{2.65}$$

where

$$P(x_o) = \frac{1 + C_o(x_o)}{2C_o(x_o)^{1/2}}. \tag{2.66}$$

Note that $P(x_o) \geq 1$ is bounded due to the boundedness of local velocity $C_o(x_o) > 0$. In particular, $P(L_o) = 1$, indicating that the total mass emerging across the medium's right side border $x_o = L_o$ (given by the field $\widehat{R}(L_o, \omega = 0)$) equals to the mass entering in the medium at $x = 0$. Thus we have established the **mass conservation law** $\int R(L_o,\tau)d\tau = \int f(\tau)d\tau$, already expected due to the absence of dissipation in system (2.20).

Meanwhile, at an interior point into the medium $0 < x_o < L_o$, with $C_o(x_o) \neq 1$, we have that $P(x_o) > 1$. As a consequence, the area of component $R$ results larger than that of the incoming pulse $f$.

### 2.6.2 Conclusions

The generalized O'Doherty-Anstey approximation derived in this section is valid for initial disturbances (in time) which are smooth and its Fourier transform is compactly supported. The new approximation can be expressed in terms of the correlation function of the medium and a coefficient controlling the dispersion mechanism introduced in the phenomenon. Its computation results inexpensive because it can be calculated by using the FFT algorithm. In the case of $\beta = 0$ the theory is consistent with previous results [9]. Moreover, the estimate results to satisfy the mass conservation law, as expected from the Boussinesq model (2.20) formulating the phenomenon which has no dissipation.

## 2.7 The coherent transmitted mode approximation

For brevity, in the following we will omit the argument $x_o$ in the functions $a_\beta(.,.)$ and $b(.,.)$. We further assume that the initial disturbance $f(\tau)$ is smooth and absolutely integrable.

From the generalized O'Doherty-Anstey approximation (2.60) (with $a_\beta(\omega) \approx a_0(\omega)$) another approximation can be deduced giving more detailed information on the transmitted wave front. For this purpose, we analyze the asymptotic behavior of integral (2.60) for large values of the parameter $x_o$. Here, the delay time $\tau$ is held fixed in $[0, T]$.

For $x_o >> 1$, we seek a long-wave approximation (equivalently low time frequencies $\omega$) by expanding the coefficients $a_0(\omega)$ and $b(\omega)$ in a Taylor series around $\omega = 0$ up to third order. This we do in order to include dispersive effects in the Fourier integral in (2.60). Doing so, leads to the estimate

$$\begin{aligned} R(x_o,\tau) \;\approx\; & \frac{1}{2\pi}\int_{-\infty}^{\infty} \widehat{f}(\omega)\exp[-x_o(a_0(0)+b(0)+(a_0'(0)+b'(0))\omega + \frac{a_0''(0)+b''(0)}{2}\omega^2 + \\ & \frac{a_0'''(0)+b'''(0)}{3!}\omega^3) + i\omega\tau]d\omega. \end{aligned} \tag{2.67}$$

It is expected that this approximation improves as $x_o$ increases. It is clear that, in making approximation (2.67), we loose the high-frequency part of the correlation function $a_0(\omega)$ and the dispersive coefficient $b(\omega)$. Therefore, only the transmitted wave front is reproduced by this estimate, as shown in Appendix G.

Now, approximation (2.67) can be rewritten as

$$R(x_o,\tau) \approx \frac{1}{2\pi}\int_{-\infty}^{\infty}\left(\int_{-\infty}^{\infty} \exp[-x_o(\alpha_o + i\mu\omega + \sigma\omega^2 + i\lambda\omega^3) + i\omega(\tau - y)]d\omega\right) f(y)\,dy, \tag{2.68}$$

with

$$\begin{aligned}
&\alpha_o = \alpha_o(x_o) = a_0(0) \quad \text{(parameter which modifies slightly the pulse's area)},\\
&\mu = \mu(x_o) = -ia_0'(0) \quad \text{(regulates the pulse's delay)},\\
&\sigma = \sigma(x_o) = \frac{a_0''(0) + b''(0)}{2} \quad \text{(parameter which controls the pulse's attenuation)},\\
&\lambda = \lambda(x_o) = -i\left(\frac{a_0'''(0) + b'''(0)}{3!}\right) \quad \text{(parameter regulating the dispersion mechanism)}.
\end{aligned}$$

Note that $b(0) = b'(0) = 0$ (c.f. equation (2.59) and the definition of $\gamma(x, \omega)$ below (2.36) ). It can also be shown that

$$\begin{aligned}
\alpha_o(x_o) &= \frac{1}{x_o}\int_0^{x_o}\int_x^{x+X} r(x)r(x')\,dx'\,dx,\\
\mu(x_o) &= \frac{1}{x_o}\int_0^{x_o}\int_x^{x+X} 2r(x)r(x')(x - x')\,dx'\,dx,\\
\sigma(x_o) &= \frac{1}{2x_o}\int_0^{x_o}\int_x^{x+X} r(x)r(x')(2i)^2(x - x')^2\,dx'\,dx + \frac{2}{x_o}\int_0^{x_o} r(x)d(x)\,dx,\\
\lambda(x_o) &= -\frac{4}{3x_o}\int_0^{x_o}\int_x^{x+X} r(x)r(x')(x - x')^3 dx dx' + \frac{1}{x_o}\int_0^{x_o}\frac{d(x)}{2}dx. \qquad (2.69)
\end{aligned}$$

Notice that all parameters above are real numbers. Also, for a particular orography's realization, the coefficient $\lambda$ gets larger as the dispersion parameter $\beta$ increases. Recall that $d(x) = \beta/(3C_o^2(x))$ in equation (2.69) above.

In addition, when $X > L_o$ we obtain a simpler expression for parameter $\alpha_o$

$$\alpha_o(x_o) = -\frac{(\ln C_o(x_o))^2}{8x_o}. \qquad (2.70)$$

Here, the parameter $\alpha_o$ is closely related to the area expansion factor $P(x_o)$ in equation (2.65). Indeed, it can be verified that $e^{-x_o\alpha_o(x_o)} \approx P(x_o)$ when $X > L_o$.

In our applications, $\lambda(x_o) > 0$ (when $\beta > 0$) and $\sigma(x_o) > 0$ (see Appendix G). Thus, by means of a suitable change of variables, the inner integral in approximation (2.68) can be written in terms of the Airy function to give

$$R(x_o, \tau) \approx [A(x_o, \cdot) * f(\cdot)](\tau), \quad x_o >> 1, \qquad (2.71)$$

where

$$A(x_o,\tau) = \frac{e^{-\alpha_o x_o} e^{\frac{\sigma}{3\lambda}[(\mu+2\sigma^2/(9\lambda))x_o-\tau]}}{(3\lambda x_o)^{1/3}} \mathrm{Ai}\left(\frac{(\mu+\sigma^2/(3\lambda))x_o-\tau}{(3\lambda x_o)^{1/3}}\right). \tag{2.72}$$

Here $*$ denotes the convolution operator and $\mathrm{Ai}(z)$ the Airy function which is defined by

$$\mathrm{Ai}(z) = \frac{1}{2\pi}\int_{-\infty}^{\infty} e^{i(z\omega+\frac{1}{3}\omega^3)}d\omega.$$

Equation (2.71) expresses that, when $x_o >> 1$, the wave front can, to leading order be approximated by a convolution between an Airy function (modulated by an exponential factor) and the initial disturbance $f(\tau)$. When the bottom is flat, $\mu = \sigma = 0$ and $0 < \beta << 1$, we are in a pure weakly-dispersive regime where the height of the wave front is decreasing like $(3\lambda x_o)^{-1/3}$ as $x_o$ increases. This case is detailed in Appendix C.

For variable depths, note how the Airy-like mechanism is altered (through the orography-dependent parameters $\mu$,$\sigma$) as a consequence of the wave interaction with the disordered media. In this case, to analyze the attenuation mechanism acting on the incident pulse, we have to consider the kernel $A(x_o,\tau)$ in convolution (2.71).

First, for $z >> 1$ we have the asymptotic approximation [1]

$$\mathrm{Ai}(z) \sim \frac{1}{2\pi} z^{-1/4} e^{-\frac{2}{3}z^{3/2}}. \tag{2.73}$$

Moreover, for $x_o >> 1$ and $\tau$ fixed, we have that

$$\frac{(\mu+\sigma^2/(3\lambda))x_o-\tau}{(3\lambda x_o)^{1/3}} \to \infty.$$

Thus, we can substitute the approximation (2.73) into (2.72) yielding that
wes

$$A(x_o,\tau) \sim \frac{e^{-\alpha_o x_o} e^{\frac{\sigma}{3\lambda}[(\mu+2\sigma^2/(9\lambda))x_o-\tau]} e^{-\frac{2[(\mu+\sigma^2/(3\lambda))x_o-\tau]^{3/2}}{3(3\lambda x_o)^{1/2}}}}{2\pi(3\lambda x_o)^{1/4}[(\mu+\sigma^2/(3/\lambda))x_o-\tau]^{1/4}}, \tag{2.74}$$

for $x_o >> 1$. Now suppose that $3\sigma \le \lambda$ and $0 < \sigma << 1$. Then it can be shown that

$$\frac{\sigma^2 x_o}{3\lambda}\left(\left(\mu+\frac{2\sigma^2}{9\lambda}\right)x_o-\tau\right)^2 < \frac{4}{9}\left(\left(\mu+\frac{\sigma^2}{3\lambda}\right)x_o-\tau\right)^3,$$

provided that $x_o >> 1$. Remark that, due to equation (2.70), the exponential factor $e^{-x_o\alpha_o}$ in the Airy kernel (2.72) remains bounded as $x_o$ increases. Then, from the approximation (2.74), we find that $A(x_o,\tau) \to 0$ when $x_o$ tends to infinity. We see that the Airy function inhibits the growth of the exponential term in (2.72) as $x_o \to \infty$. At the same time, we verified the progressive attenuation induced on the incoming pulse by the disordered orography.

Furthermore at the wave front $\tau = (\mu + \sigma^2/(3\lambda))x_o$, the kernel $A(x_o,\tau)$ reduces to

$$A(x_o,\tau) = \frac{Ce^{-\frac{\sigma^3}{27\lambda^2}x_o} e^{-\alpha_o x_o}}{(3\lambda x_o)^{1/3}}, \tag{2.75}$$

where $C$ is a constant. This means that the amount of attenuation close to the wave front increases, relative to the purely dispersive regime (constant depth), approximately by an exponential factor.

In addition to the attenuation phenomenon, the pulse is simultaneously **delayed** and **broadened**. The delay is observed relative to the pulse's travel time up to a fixed station $x_o$ into the medium. This is due to the quantity $(\mu + \sigma^2/(3\lambda))x_o$ appearing in the argument of the Airy function in equation (2.72). The broadening is found to be proportional to $x_o^{1/3}$.

Equivalently, the phenomenon can be decomposed into two stages by using convolution operators in equation (2.67). Namely,

$$R(x_o,\tau) \approx [G(x_o,\cdot) * G_d(x_o,\cdot) * f(\cdot)](\tau), \tag{2.76}$$

where

$$G(x_o,y) = \frac{e^{-\alpha_o x_o} e^{-\frac{(y-\mu x_o)^2}{4\sigma x_o}}}{\sqrt{4\pi\sigma x_o}}$$

and

$$G_d(x_o,y) = \frac{1}{(3x_o\lambda)^{1/3}} \mathrm{Ai}\left(-\frac{y}{(3x_o\lambda)^{1/3}}\right).$$

Hence, dispersion convolves the initial disturbance with the Airy kernel $G_d$. At the same time, the orography's fluctuations act on the resulting pulse $G_d * f$ through the Gaussian kernel $G$ which diffuses it around the moving center $y = \mu x_o$.

By differentiating equation (2.68) with respect to $x_o$ and $\tau$ we find that

$$\begin{aligned}
R_{x_o} &\approx -(\tilde{\alpha}_o + i\tilde{\mu}\omega + \tilde{\sigma}\omega^2 + i\tilde{\lambda}\omega^3)R, \\
R_\tau &\approx i\omega R, \\
R_{\tau\tau} &\approx -\omega^2 R, \\
R_{\tau\tau\tau} &\approx -i\omega^3 R,
\end{aligned}$$

where

$$\tilde{\alpha}_o(x_o) = \alpha_o(x_o) + x_o\alpha_o'(x_o), \quad \tilde{\sigma}(x_o) = \sigma(x_o) + x_o\sigma'(x_o),$$
$$\tilde{\mu}(x_o) = \mu(x_o) + x_o\mu'(x_o), \quad \tilde{\lambda}(x_o) = \lambda(x_o) + x_o\lambda'(x_o).$$

As a result, for $x_o >> 1$, the pulse seems to be governed by the linear dispersive-diffusion equation in time

$$R_{x_o} = -\tilde{\mu}(x_o)R_\tau + \tilde{\sigma}(x_o)R_{\tau\tau} + \tilde{\lambda}(x_o)R_{\tau\tau\tau} - \tilde{\alpha}_o(x_o)R. \tag{2.77}$$

In the hyperbolic regime ($\beta = 0$), $\sigma(x_o)$ and $\lambda(x_o)$ reduce to

$$\begin{aligned}
\sigma(x_o) &= \frac{1}{2x_o}\int_0^{x_o}\int_x^{x+X} r(x)r(x')(2i)^2(x-x')^2\,dx'\,dx,\\
\lambda(x_o) &= 0,
\end{aligned}$$

($\alpha_o(x_o)$ and $\mu(x_o)$ are as above) and the approximation (2.71) is replaced by

$$R(x_o,\tau) \approx \frac{e^{-\alpha_o x_o}}{\sqrt{4\pi\sigma x_o}}\int_{-\infty}^{\infty} e^{-\frac{(\tau-\mu x_o - y)^2}{4\sigma x_o}} f(y)dy, \tag{2.78}$$

for $x_o >> 1$.

Approximation (2.78) means that at great distances from the disturbance's origin the pulse seems to be diffused around the moving center $\tau = \mu x_o$, obeying the linear advection-diffusion equation in time

$$R_{x_o} = -\tilde{\mu}(x_o)R_\tau + \tilde{\sigma}(x_o)R_{\tau\tau} - \tilde{\alpha}_o(x_o)R. \tag{2.79}$$

Formula (2.78) resembles the one derived by Berlyand and Burridge [11] for a Goupillaud medium. In their result, fluctuations vanish in average and the total mass seems to be in the pulse front. For this reason, in their theory, factor $e^{-\alpha_o x_o}$ does not appear and the pulse travels approximately with constant area. In Appendix G we compute the scattering parameters $\alpha_o$, $\mu$, $\sigma$ and $\lambda$ and validate numerically the approximations (2.71) and (2.78).

It is also important to note that the attenuation predicted by equations (2.71) and (2.78) is entirely due to multiple scattering and dispersion effects since there is no dissipation in model (2.20).

## 2.8 Summary of results

We have shown that the linear Boussinesq system (2.20) can be decomposed as a coupled KdV-type equations with variable coefficients for the transmitted and reflected fields introduced. In turn, in the Fourier domain, it transforms into a system of coupled linear ordinary differential equations which describe the evolution of the transmitted and reflected signals with respect to the travel time $x$. Due to the linearity of the resulting equations, the invariant imbedding representation is valid within a medium slab $[x_o, x_o + X]$, furnishing a relationship between the reflected and the transmitted signals through the reflection kernel $K$ which contains all the medium's reflection properties. The Fourier transform of the reflection kernel was shown to satisfy a non-trivial Riccati equation. The analysis of this nonlinear equation is performed by means of a lemma that generalizes that of Berlyand and Burridge [9]. It leads to the generalized O'Doherty-Anstey approximation for dispersive waves governed by the Boussinesq system (2.20). This is our main theoretical result in this chapter. By applying this result, the asymptotic analysis of Section 2.7 shows a progressive attenuation, broadening and delay acting in the incoming pulse as a consequence of disorder and dispersion. These phenomena are found to be more noticeable the longer the wave penetrates the disordered medium.

# Chapter 3

# Numerical results

The numerical simulations will be performed with the weakly-nonlinear, weakly-dispersive Boussinesq system presented in Nachbin [45],

$$
\begin{aligned}
&M(\xi)\eta_t + \left(\left(1 + \frac{\alpha\eta}{M(\xi)}\right)u\right)_\xi = 0, \\
&u_t + \eta_\xi + \frac{\alpha}{2}\left(\frac{u^2}{M(\xi)^2}\right)_\xi - \frac{\beta}{3}u_{\xi\xi t} = 0,
\end{aligned}
\tag{3.1}
$$

for $-\infty < \xi < \infty$ and $t > 0$.

We will study the scattering of Gaussian-shaped disturbances of the form

$$
u(\xi, 0) = \eta(\xi, 0) = e^{-(\xi-\xi_o)^2/\epsilon}, \tag{3.2}
$$

where the parameter $\xi_o$ controls the pulse's initial position and $\epsilon > 0$ its effective width. Furthermore, we also consider solitary waves of the form

$$
\begin{aligned}
\eta(\xi, 0) &= A_1 \operatorname{sech}^2(B(\xi - \xi_o)) + A_2 \operatorname{sech}^4(B(\xi - \xi_o)), \\
u(\xi, 0) &= A \operatorname{sech}^2(B(\xi - \xi_o)),
\end{aligned}
\tag{3.3}
$$

with $A_1$, $A_2$, $A$ and $B$ constants to be defined later.

Except for some special cases (for instance when $M \equiv 1, \alpha = 0$ or $\beta = 0$), finding the solution of system (3.1) is a nontrivial problem. To solve system (3.1) numerically, we will use a finite-differences solver introduced by Wei and Kirby [56]. This scheme will be used to perform several numerical experiments in order to validate and study (within a regime of small amplitudes) the extent of application of the linear theory developed in chapter 2.

First we rewrite the system (3.1) in a more convenient way, as

$$\begin{aligned} \eta_t &= E(\eta, u), \\ V_t &= F(\eta, u), \end{aligned} \tag{3.4}$$

where

$$\begin{aligned} E(\eta, u) &= -\frac{1}{M(\xi)}\left(\left(1+\frac{\alpha\eta}{M(\xi)}\right)u\right)_\xi, \\ F(\eta, u) &= -\eta_\xi - \frac{\alpha}{2}\left(\frac{u^2}{M(\xi)^2}\right)_\xi, \end{aligned} \tag{3.5}$$

and $V$ is an intermediate variable defined by

$$V = u - \frac{\beta}{3}u_{\xi\xi}.$$

We now approximate the solution of system (3.4) by using a high-order predictor-corrector solver. The space-time domain $\xi \in [\xi_1, \xi_J]$, $t \geq 0$ will be discretized by $\xi_j = \xi_1 + (j-1)\Delta\xi, 1 \leq j \leq J$ and $t_n = (n-1)\Delta t, 1 \leq n \leq N$, respectively. The discretizations of the variables $u, \eta, V$ will be denoted by $u_j^n, \eta_j^n, V_j^n$.

As is well known, the predictor-corrector schemes combine two numerical methods. First a third-order explicit Adams-Bashforth solver will be employed to produce a predicted value of $(V, \eta)$ and then a fourth-order implicit Adams-Moulton scheme is applied to obtain a corrected solution.

The explicit predictor step is given by

$$\begin{aligned} \eta_j^{n+1} &= \eta_j^n + \frac{\Delta t}{12}(23E_j^n - 16E_j^{n-1} + 5E_j^{n-2}), \\ V_j^{n+1} &= V_j^n + \frac{\Delta t}{12}(23F_j^n - 16F_j^{n-1} + 5F_j^{n-2}), \end{aligned} \tag{3.6}$$

where the values at levels $n-2$, $n-1$, $n$ are known. Furthermore the notation $E_j^n = E(\eta_j^n, u_j^n)$ and $F_j^n = F(\eta_j^n, u_j^n)$ is used.

In this step some remarks should be made :
The first-order derivatives $u_\xi$, $\eta_\xi$ (which appear in expanding the derivatives in equation (3.5)) are approximated by the fourth-order schemes

$$
\begin{aligned}
u_\xi(\xi_j) &\approx \frac{8(u_{j+1}-u_{j-1})+u_{j-2}-u_{j+2}}{12\Delta\xi}+O(\Delta\xi^4),\\
\eta_\xi(\xi_j) &\approx \frac{8(\eta_{j+1}-\eta_{j-1})+\eta_{j-2}-\eta_{j+2}}{12\Delta\xi}+O(\Delta\xi^4),
\end{aligned}
$$

at interior points such that $3 \le j \le J-2$. At boundary points we use the fourth-order approximations

$$
\begin{aligned}
u_\xi(\xi_1) &\approx \frac{-3u_5+16u_4-36u_3+48u_2-25u_1}{12\Delta\xi}+O(\Delta\xi^4),\\
u_\xi(\xi_2) &\approx \frac{u_5-6u_4+18u_3-10u_2-3u_1}{12\Delta\xi}+O(\Delta\xi^4),\\
u_\xi(\xi_{J-1}) &\approx \frac{3u_J+10u_{J-1}-18u_{J-2}+6u_{J-3}-u_{J-4}}{12\Delta\xi}+O(\Delta\xi^4),\\
u_\xi(\xi_J) &\approx \frac{25u_J-48u_{J-1}+36u_{J-2}-16u_{J-3}+3u_{J-4}}{12\Delta\xi}+O(\Delta\xi^4),
\end{aligned}
$$

and analogous formulas for $\eta$.

Computation of $\eta_j^{n+1}$ from equations (3.6) is straightforward. Nevertheless, in evaluating the fluid velocity $u_j^{n+1}$ we must solve the (spatial) ordinary differential equation

$$
u-\frac{\beta}{3}u_{\xi\xi}=V, \tag{3.7}
$$

which is forced by the known left hand side $V$. Equation (3.7) is discretized by the second-order approximation

$$
u_j^{n+1}-\frac{\beta}{3}\left(\frac{u_{j+1}^{n+1}-2u_j^{n+1}+u_{j-1}^{n+1}}{\Delta\xi^2}\right)=V_j^{n+1},
$$

for $2 \le j \le J-1$.

To compute the boundary values $u_1^{n+1}$, $u_J^{n+1}$, $\eta_1^{n+1}$ and $\eta_J^{n+1}$ at level $n+1$ we use the radiation conditions (B. Engquist and A. Majda [19])

$$
\begin{aligned}
u_t-u_\xi &= 0, \quad \text{at } \xi=\xi_1, \\
u_t+u_\xi &= 0, \quad \text{at } \xi=\xi_J,
\end{aligned} \tag{3.8}
$$

and

$$\begin{aligned} \eta_t - \eta_\xi &= 0, \quad \text{at} \ \ \xi = \xi_1, \\ \eta_t + \eta_\xi &= 0, \quad \text{at} \ \ \xi = \xi_J, \end{aligned} \tag{3.9}$$

which are discretized by the first-order in time, fourth-order in space approximations

$$\begin{aligned} \frac{u_1^{n+1} - u_1^n}{\Delta t} &= \frac{-3u_5^n + 16u_4^n - 36u_3^n + 48u_2^n - 25u_1^n}{12\Delta\xi}, \\ \frac{u_J^{n+1} - u_J^n}{\Delta t} &= -\frac{25u_J^n - 48u_{J-1}^n + 36u_{J-2}^n - 16u_{J-3}^n + 3u_{J-4}^n}{12\Delta\xi}, \end{aligned}$$

and similar approximations for $\eta$.

Thus, to go from variable $V$ to $u$, a tridiagonal linear system of dimension $J-2$ x $J-2$ must be solved. The system's matrix has the following structure:

$$\begin{pmatrix} \Delta\xi^2 + 2\beta/3 & -\beta/3 & 0 & 0 & \cdots & 0 \\ -\beta/3 & \Delta\xi^2 + 2\beta/3 & -\beta/3 & 0 & \cdots & \vdots \\ 0 & -\beta/3 & \Delta\xi^2 + 2\beta/3 & -\beta/3 & \cdots & 0 \\ \vdots & 0 & \ddots & \ddots & & \vdots \\ \vdots & \vdots & & & & 0 \\ \vdots & \vdots & & & & -\beta/3 \\ 0 & 0 & \cdots & 0 & -\beta/3 & \Delta\xi^2 + 2\beta/3 \end{pmatrix}. \tag{3.10}$$

We remark that this matrix is constant in time and thus just one $LU$ decomposition must be performed at the starting point. This decomposition may be stored to be used in each time step.

Once the predicted values $\eta_j^{n+1}, u_j^{n+1}$ are obtained we compute $E_j^{n+1}, F_j^{n+1}$ from equations (3.5). The corrected values are calculated from

$$\begin{aligned} \eta_j^{n+1} &= \eta_j^n + \frac{\Delta t}{24}(9E_j^{n+1} + 19E_j^n - 5E_j^{n-1} + E_j^{n-2}), \\ V_j^{n+1} &= V_j^n + \frac{\Delta t}{24}(9F_j^{n+1} + 19F_j^n - 5F_j^{n-1} + F_j^{n-2}), \end{aligned} \tag{3.11}$$

where the quantities at level $n+1$ are computed iteratively by using the predicted approximation as initial value. The new $u_j^{n+1}$ is computed from $V_j^{n+1}$ as in the predictor step. We stop the iteration process when the relative error between two successive corrected values $\eta^{n+1}$, $u^{n+1}$ and $\eta^{(n+1)^*}$, $u^{(n+1)^*}$ satisfies that

$$\Delta u^{n+1} = \frac{\sum_i \left| u_j^{n+1} - u_j^{(n+1)^*} \right|}{\sum_i \left| u_j^{n+1} \right|} < tol$$

and

$$\Delta \eta^{n+1} = \frac{\sum_i \left| \eta_j^{n+1} - \eta_j^{(n+1)^*} \right|}{\sum_i \left| \eta_j^{n+1} \right|} < tol.$$

We set $tol = 0.001$. This tolerance is achieved with only one iteration in all our experiments.

Note that at least three time levels must be known in order to initialize the scheme above. In this task the explicit fourth-order Runge-Kutta method is employed. This scheme is given by

$$\begin{aligned}
\eta^{n+1} &= \eta^n + \frac{\Delta t}{6}(K_1 + 2K_2 + 2K_3 + K_4), \\
V^{n+1} &= V^n + \frac{\Delta t}{6}(\tilde{K}_1 + 2\tilde{K}_2 + 2\tilde{K}_3 + \tilde{K}_4),
\end{aligned}$$

where

$$\begin{aligned}
K_1 &= E(\eta^n, u^n), \\
K_2 &= E(\eta^n + (1/2)\Delta t K_1, u^n + (1/2)\Delta t K_1), \\
K_3 &= E(\eta^n + (1/2)\Delta t K_2, u^n + (1/2)\Delta t K_2), \\
K_4 &= E(\eta^n + \Delta t K_3, u^n + \Delta t K_3), \\
\tilde{K}_1 &= F(\eta^n, u^n), \\
\tilde{K}_2 &= F(\eta^n + (1/2)\Delta t \tilde{K}_1, u^n + (1/2)\Delta t \tilde{K}_1), \\
\tilde{K}_3 &= F(\eta^n + (1/2)\Delta t \tilde{K}_2, u^n + (1/2)\Delta t \tilde{K}_2), \\
\tilde{K}_4 &= F(\eta^n + \Delta t \tilde{K}_3, u^n + \Delta t \tilde{K}_3), \\
\eta^n &= (\eta_1^n, \eta_2^n, ..., \eta_J^n), \quad V^n = (V_1^n, V_2^n, ..., V_J^n), \\
u^n &= (u_1^n, u_2^n, ..., u_J^n).
\end{aligned}$$

Since only one tridiagonal linear system must be solved in each iteration we find Wei and Kirby's scheme very efficient and cheap. As shown in Appendix H its precision is

$O(\Delta\xi^2) + O(\Delta t^4)$. It was implemented by using the MATLAB 6.0 package where we have at hand vectorized routines to deal with large sparse matrixes. Its computational cost is found to be approximately linear which in particular means that when spatial or time meshes are doubled then the time of computation is also multiplied by 2.

Other finite difference schemes for Boussinesq systems were considered in our investigation. In [8] is exposed a 4th-order method in space and time which also reduces to solve one tridiagonal linear system in each iteration. However it was discarded because its stability properties depend highly on the presence of symmetric dispersive terms on both equations of the Boussinesq system.

On the other hand, Nwogu [48] proposes a 3rd-order scheme which combines a first order prediction with a 2nd-order iterative Crank-Nicholson scheme as corrector. The truncation errors of the same form as the dispersive terms in the Boussinesq equations (in our case the term $u_{\xi\xi t}$) are added as corrections at the iterative stage. This strategy insures 3rd order of accuracy in time and space and that the dispersive characteristics of the model be accurately reproduced. This scheme results costly (two tridiagonal systems must be solved in each iteration) and difficult of implementing.

## 3.1 Testing the numerical method

Extensive experiments are carried out in order to test the numerical solver described in the preceding section.

**Experiment 1 :(Flat bottom/weakly-nonlinear regime)**. In these experiments the pulse is assumed to propagate over a flat bottom ($M \equiv 1$). In Appendix A (c.f. equations (A.8) and (A.9)) we show that if in addition $\alpha = 0$ we can solve explicitly system (3.1) by using the Fourier transform technique. This solution may be employed to test the numerical scheme's precision and stability properties.

In Figure 3.1 we see that the exact solution $\eta$ (for $\beta = 0.03$ and $t = 40$) and the numerical solution for $\alpha = 0.001$, $\beta = 0.03$ are in good agreement. The numerical parameters are $J = 4000$ (spatial mesh points), $N = 5000$ (time mesh points), $\Delta\xi = 0.0125$ (space step), $\Delta t = 0.008$ (time step). As expected, this test shows that the code is capturing very well the effectively linear dispersive regime when $\alpha$ is small enough.

In Figure 3.2 we repeat the experiment above for $\alpha = 0.001$, $\beta = 0.0005$ and $t = 40$. Now an effective linear hyperbolic regime is observed.

Additional tests show that a sufficient condition for the code's stability is that $\Delta t/\Delta\xi \leq 0.6$. Furthermore, note that the code's high-order accuracy models very well the dispersive characteristics of the model. An analysis of the truncation error of the numerical method

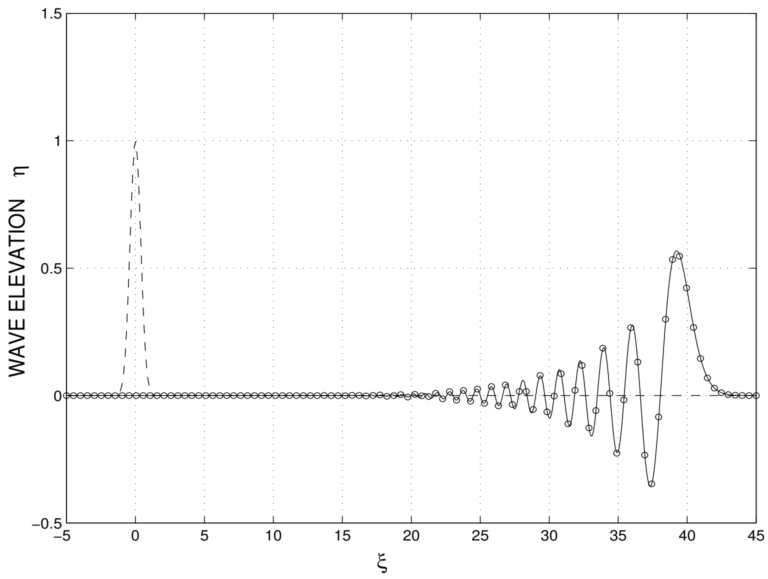


Figure 3.1: Dashed line : initial pulse $\eta(\xi,0) = u(\xi,0) = e^{-\xi^2/0.3}$. Solid line : numerical solution for $\alpha = 0.001$, $\beta = 0.03$ and $t = 40$. Dotted line : Exact solution.

can be found in Appendix H.

Radiation conditions (3.8)-(3.9) also proved to absorb appropriately waves leaving the computational domain. It was observed that reflected waves produced by the computational boundaries were negligible.

**Experiment 2 :(Flat bottom/weakly-nonlinear,weakly-dispersive regime)**. We now study system (3.1) in the case that $M \equiv 1$, $0 < \alpha << 1$, and $0 < \beta << 1$, that is a soliton. Under these hypothesis, it is possible to obtain an approximate rigthgoing solitary wave solution of system (3.1) which has the following analytical form

$$\begin{aligned} \eta(\xi,t) &= A_1 \operatorname{sech}^2(B(\xi - Ct - \xi_o)) + A_2 \operatorname{sech}^4(B(\xi - Ct - \xi_o)), \\ u(\xi,t) &= A \operatorname{sech}^2(B(\xi - Ct - \xi_o)), \end{aligned} \tag{3.12}$$

where

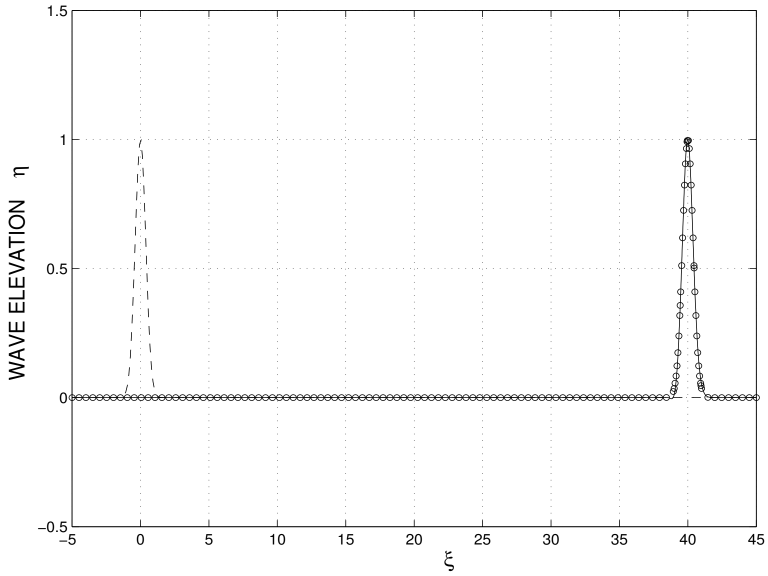


Figure 3.2: Dashed line : initial disturbance $\eta(\xi, 0) = u(\xi, 0) = e^{-\xi^2/0.3}$. Solid line : numerical solution for $\alpha = 0.001$, $\beta = 0.0005$ and $t = 40$. Dotted line : Initial Gaussian pulse at $t = 40$.

$$
\begin{aligned}
A_1 &= \frac{C^2-1}{\alpha C^2} = \frac{1}{C^2}, \quad C = \sqrt{1+\alpha}, \\
A_2 &= \frac{(C^2-1)^2}{\alpha C^2} = \frac{\alpha}{C^2}, \quad A = \frac{C^2-1}{\alpha C} = \frac{1}{C},
\end{aligned}
$$

and

$$
B = \left\{ \frac{C^2-1}{(4/3)\beta C^2} \right\}^{1/2} = \left\{ \frac{\alpha}{(4/3)\beta C^2} \right\}^{1/2}.
$$

Note that $A_1 + A_2 = 1$. See Wei and Kirby [56] for details.

In Figure 3.3 we graph the analytical solution $\eta$ given by equation (3.12) for $\alpha = 0.03$, $\beta = 0.03$ at time $t = 30$. The initial soliton's position is set to $\xi_o = 0$. The numerical solution is also included in this plot for the parameters $J = 2000$, $N = 2500$, $\Delta\xi = 0.025$ and $\Delta t = 0.012$.

Observe that the pulse's propagation velocity is approximately $C \approx 1.0149$, in agreement with solution (3.12), preserving its initial shape. This fact was expected because of the balance existing between dispersive and nonlinear effects ($\alpha = \beta = 0.03$). The code

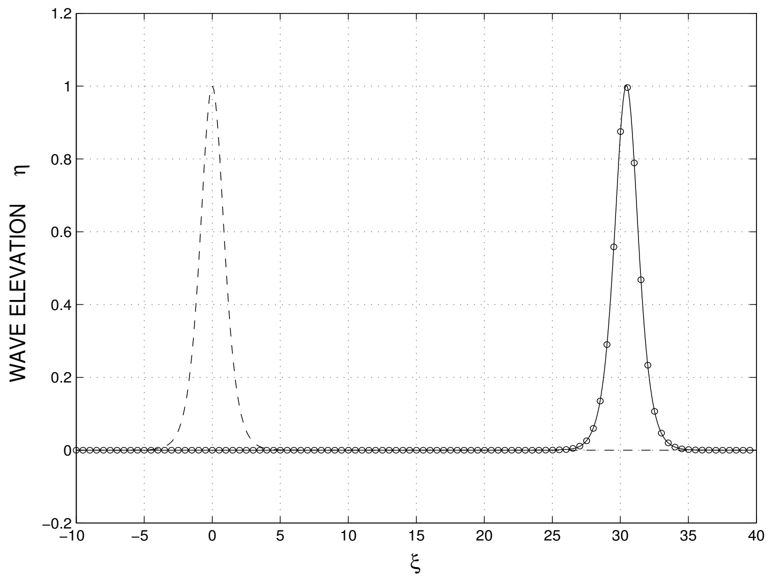


Figure 3.3: Solitary wave propagating over a flat bottom. Dashed line : initial disturbance $\eta(\xi, 0) = A_1 \operatorname{sech}^2(B\xi) + A_2 \operatorname{sech}^4(B\xi)$. Solid line : numerical solution for $\alpha = 0.03$, $\beta = 0.03$ and $t = 30$. Dotted line : Analytical solution (3.12).

reproduces very well the weakly-dispersive, weakly-nonlinear evolution of the soliton. More generally we find that the approximate solitary wave solution preserves its shape when $O(\beta) \approx O(\alpha) < 0.1$.

**Experiment 3 :(Periodic slowly-varying orography/effectively hyperbolic regime)**. In experiments 1 and 2, in which the water depth was assumed to be flat, the orography-dependent coefficient $M(\xi)$ becomes identically one. However, for variable depth, computation of function $M(\xi)$ involves the resolution of a change of variables problem which is not an easy task. For this reason, in next experiments it will be synthetized and replaced by functions of the form $M(\xi) = 1 + n(\xi)$, where $n(\xi) < 1$ describes the coefficient's fluctuations. Thus we ignore (for the time being) its dependence on the original orography. Nevertheless, this strategy will prove to be useful for observing the phenomena we are interested in and validating the pulse-shaping theory. Nevertheless, in Section 3.6 we compute function $M(\xi)$ and validate the theory in the particular case of a piecewise linear orography.

We start by considering an effective linear hyperbolic regime ( $\alpha = 0.001$, $\beta = 0.0005$) and a periodic slowly-varying coefficient of the form

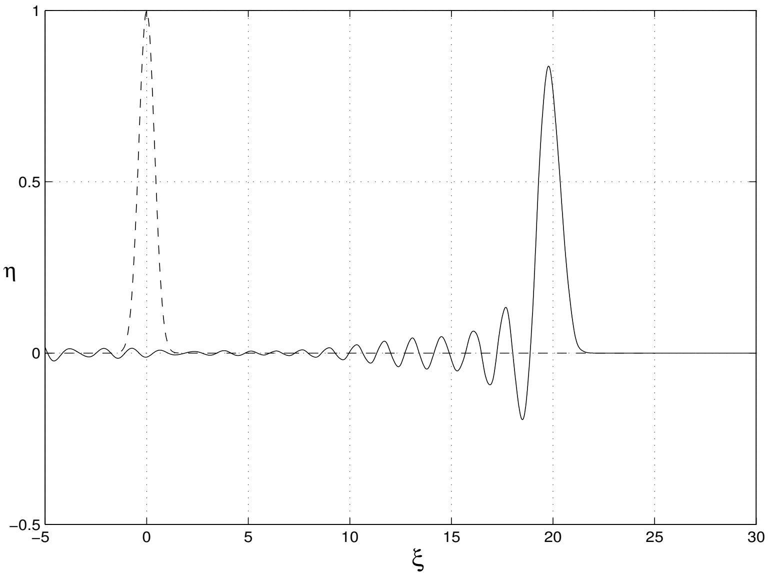


Figure 3.4: Pulse propagating over a synthetic periodic slowly-varying topography. Solid line: Numerical solution for $\alpha = 0.001$, $\beta = 0.0005$ and $t = 20$. Dashed line : initial disturbance $\eta(\xi, 0) = e^{-\xi^2/0.3}$ (effective width $\ell_p \approx 2$).

$$M(\xi) = \begin{cases} 1 + 0.5\sin(60\pi\ \frac{\xi-5}{20}), & \text{for } 5 \le \xi \le 25, \\ 1, & \text{otherwise.} \end{cases}$$

Thus the bottom irregularities are located in the region $5 \le \xi \le 25$ and the number of bottom's oscillations is 30. The initial Gaussian's effective width is $\ell_p \approx 2$ and therefore the ratio inhomogeneities/wavelength is about 3/10.

In Figure 3.4 we visualize the numerical solution for $\alpha = 0.001$, $\beta = 0.0005$ and $t = 20$. The numerical parameters are $J = 5000$, $N = 4000$, $\Delta\xi = 0.01$, $\Delta t = 0.005$. By analyzing Figure 3.4 we find out that the reflected wave length ($\approx 1.67$) is approximately equal to twice the oscillation length of the bottom fluctuations ($\approx 0.67$), which is in perfect agreement with Bragg's resonance phenomenon (see Guazzeli, Rey and Belzons [25]). The attenuation in the amplitude of the pulse (about 20% of its initial height) and the oscillations behind the pulse (which correspond to reflected waves) are produced by the periodic coefficient $M(\xi)$.

**Experiment 4 :(Periodic rapidly-varying orography/effectively hyperbolic regime)**. Set $\alpha = 0.001$ and $\beta = 0.0005$ and consider the periodic rapidly-varying coefficient

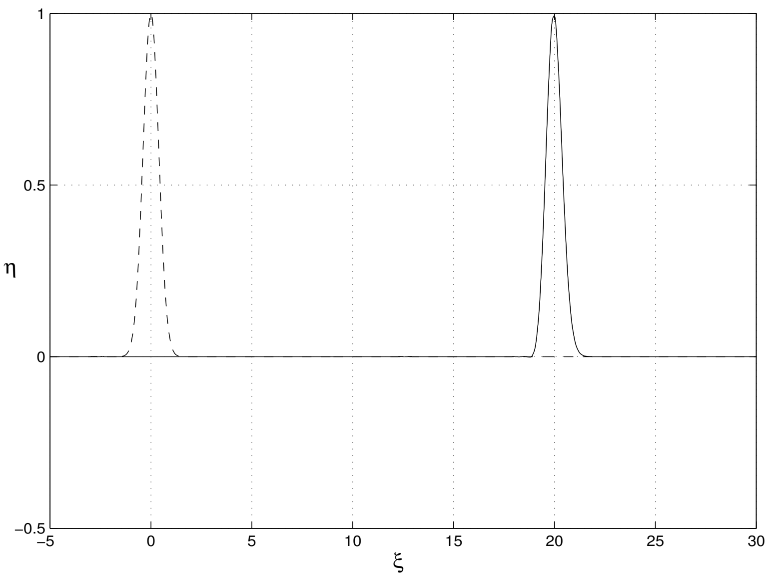


Figure 3.5: Pulse propagating over a synthetic periodic rapidly-varying topography. Solid line: Numerical solution for $\alpha = 0.001$, $\beta = 0.0005$ and $t = 20$. Dashed line : initial disturbance $\eta(\xi, 0) = e^{-\xi^2/0.3}$ (effective width $\ell_p \approx 2$).

$$M(\xi) = \begin{cases} 1 + 0.5\sin(200\pi\ \frac{\xi-5}{20}), & \text{for } 5 \leq \xi \leq 25, \\ 1, & \text{otherwise.} \end{cases}$$

Note that the number of bottom's oscillations was increased to 100 and the ratio irregularities/wavelength is about 1/10, three times smaller than in experiment 3. The corresponding numerical solution is displayed in Figure 3.5. The numerical parameters are the same as in experiment 3. We point out that the pulse propagates without changing its shape only experimenting a small variation in amplitude when entering and leaving the rough region. The propagation velocity was found to be smaller than 1. Observe that no reflections are generated in contrast to Figure 3.4. These facts are in agreement with Nachbin [44].

## 3.2 Disordered orography / hyperbolic regime

The experiments presented above show the excellent properties of our numerical code modelling very well dispersive characteristics of Boussinesq model (3.1) and capturing fine details of periodic rapidly-varying orographies. In all cases the results are in perfect accordance with theoretical results in the literature. Thus we are now in a position of applying it to the more general case of disordered orographies. The numerical simulations are carried out in the nonlinear Boussinesq system (3.1) which enables us to analyze the effect of weak nonlinearities in the phenomenon and know the extent of application of the linear pulse-shaping theory.

We wish to validate the theory of Chapter 2 without dispersion ($\beta = 0$) when model (3.1) reduces to a hyperbolic system. We consider initial rightgoing Gaussian-shaped disturbances of the form (3.2) propagating over a disordered rapidly-varying orography.

Here the coefficient $M(\xi)$ is synthetized as

$$M(\xi) = 1 + \delta n(\xi/\ell), \tag{3.13}$$

where $n(\xi)$ is a mean-zero piecewise linear function, constructed by using a random number generator in the interval [-1,1], $0 < \delta < 1$ is the amplitude of fluctuations and $\ell$ the correlation length of the orography's irregularities. At the corners $M'(\xi)$ is taken as the leftside derivative of function $M(\xi)$.

The parameters in the initial Gaussian pulse and the orography's correlation scale are such that the ratio inhomogeneities/wavelength is 1/10. To this effect we take $\epsilon = 0.05$ (in equation (3.2)) which gives a pulse with effective width $\ell_p \approx 1$ and $\ell = 0.1$. Unless explicitly modified this is the scaling adopted in the following.

To start we set the level of nonlinearity to be weak $\alpha = 0.001$. The orography irregularities covers the interval [5,45] and the amplitude of fluctuations is $\delta = 0.5$. Outside this interval the bottom is assumed to be flat.

The numerical parameters are $J = 10000$, $N = 11500$, $\Delta\xi = 8.5e-3$ and $\Delta t = 5.2e-3$. This sets 24 grid points for each orography's mountain. Large mesh sizes are necessary for the code's stability and for the radiation conditions to work efficiently. The interval [-15,70] is adopted as the computational domain. The time of computation of each experiment is about 20 minutes on a Linux system computer.

The Gaussian pulse (in space) is located at position $\xi_o = -5$ at time $t = t_o$ and allowed to propagate to the right. To be consistent with the theory, at the origin $\xi = 0$ the signal is recorded in time up to $11500\Delta t$ which supplies the incoming pulse $f(\tau)$ required to evaluate the ODA approximation. Moreover the initial time $t_o$ is such that this pulse results centered in the delay time variable $\tau$. To this end we set $t_o = -5$. Therefore from the definition of the transmitted mode $R$ ( equation (2.23)) and equation (3.2) we have that $f(\tau) = 2e^{-\tau^2/0.05}$. We refer to Figure 3.6 containing a schematic description of this procedure.

In Figure 3.7(b) we compare the numerical solution at the medium position $\xi = 20$ with the ODA approximation (2.62) where the length of the slab used in the invariant imbedding technique (see equation (2.58) or (2.61) in Chapter 2) is taken to be $X = 5$. We observe that the coherent front of the transmitted wave and part of the incoherent coda are reproduced up to approximately $\tau = 10$ with a high accuracy (about $O(10^{-2})$ ).

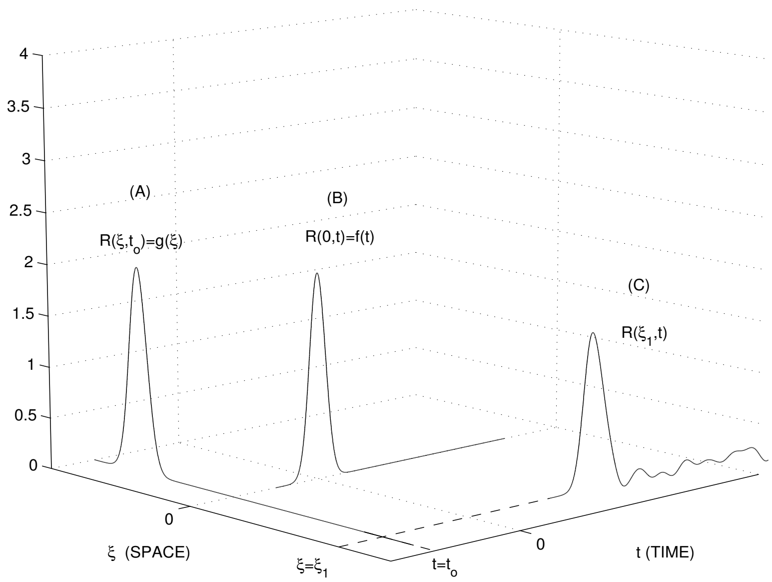


Figure 3.6: (A) Gaussian pulse $g(\xi)$ corresponds to the initial disturbance in space which is supplied to the numerical code. (B) When this pulse arrives at the interface $\xi = 0$ it is recorded (in time) to be used as the incoming pulse $f(t)$ for the theoretical formula (2.60). In the hyperbolic case this pulse is again a Gaussian. (C) The signal is recorded (in time) at the fixed station $\xi = \xi_1$ selected into the medium.

To study the dependence of the theory on this parameter we increase it to $X = 20$ and compare again with the corresponding numerical solution (see Figure 3.7(c)). We observe that the theory captures an even longer part (up to $\tau = 15$ approximately) of the incoherent forward scattering radiation. This is an outstanding fact of the theory not mentioned in the previous work [9]. The length of the time interval over which the signal is recovered with good accuracy is approximately twice the length of the medium slab $X$ used. This is the time required for the signal going to location $x_o + X$ and return to the observation station at $x_o$. Thus for $\tau > 2X$ the information of the medium beyond $x_o + X$ is necessary. For instance in Figure 3.7(b) (where $X = 5$) the ODA approximation represents well the signal up to $\tau = 10$. Beyond this point the approximation is about zero. This is in accordance with the invariant imbedding approach which assumes the medium to be homogeneous for $x > x_o + X$.

In Figure 3.8 we show the effect of the fluctuations upon the pulse shape as long as it propagates through the disordered medium. In all cases the ODA approximation and the numerical simulation are in good agreement.

Let us analyze the different phenomena predicted by the deterministic theory. First a progressive attenuation in the height of the pulse is observed. According to the theory the amount of attenuation is proportional to the square root of the propagation distance (c.f. equation (2.78)). In Figure 3.8(e) the pulse's height decays to about 50% after propagating 35 units of inhomogeneous channel (equivalent to 35 pulse widths). Second, the wave front is delayed when observed in the travel time reference frame. This is mainly observed in Figures 3.8(d) and 3.8(e) where the peak of the wave appears slightly shifted to the right of the origin $\tau = 0$. Furthermore the delay is found to increase with the travel distance.

We remark that since the scattering parameter $\sigma$ (responsible for the pulse's attenuation) in equation (2.78) is small (about order $10^{-3}$, c.f. Appendix G) the propagation distance must be large enough (about $20\ell_p$) so that the effect of fine fluctuations become noticeable. This is verified in Figure 3.8(b) at the medium station $\xi = 6$ (equivalent to $6\ell_p$) where the initial pulse is almost unchanged and only a small fluctuation begins to appear ahead the Gaussian.

Observe also that at the medium location $\xi = 40$ the pulse has been broadened ( approximately twice its initial value) as shown in Figure 3.8(d). This **broadening** phenomenon (also called **apparent diffusion**) also increases with the travel distance.

Now we increase the nonlinearity parameter three times $\alpha = 0.003$. At this level of nonlinearity the linear radiation conditions (3.8)-(3.9) do not absorb appropriately waves arriving at the computational boundaries. Numerical instability is observed to appear near the rightside boundary. The more efficient way we found to solve this problem was extending the computational domain to [-10,85]. Furthermore the spatial mesh size is increased to $J = 11200$. All other numerical parameters are the same as before. This does not alter very much the time of computation which is again estimated in 20 minutes.

In Figure 3.9 we see that the linear theory even captures the front of the transmitted pulse and a part of the fluctuating coda following it. The maximum error in the wave front (of roughly $O(10^{-1})$ reached at the wave's peak) appears to be larger than in the coda where it is of approximately $O(10^{-2})$. Thus nonlinear effects are first observed in the crest of the wave as long as the coda evolves approximately in a linear regime and the ODA theory still gives a reasonable prediction.

Then the nonlinearity parameter is increased to $\alpha = 0.005$. In Figure 3.10 we see that the transmitted wave is near to break (it is shifted to the left) and the linear theory is no longer valid. The oscillations in front of the pulse are due to the numerical method.

On the other hand, according to the results in Section 2.7, a higher amplitude $\delta$ of the orography's fluctuations (and therefore a larger orography slope) enlarges the attenuation, delay and broadening on the incoming pulse. The reason for this is that we have a higher absolute local reflection coefficient $|r(x)|$ in the correlation function $a_0(x_o, \omega)$ controlling the wave's delay and attenuation (see equation (2.58)). Recall that $r(x) = -1/4M'(x)/M(x)$. Consequently, the scattering parameters $\sigma$ and $\mu$ in the Gaussian approximation (2.78) are expected to be larger.

To confirm this we reduce the amplitude of the fluctuations in 50% ($\delta = 0.25$). In Figure 3.11 we compare the resulting signal to that obtained over an orography with $\delta = 0.5$ at the same medium location $\xi = 30$. The nonlinear parameter is set to be $\alpha = 0.001$ in both cases. Other parameters in the orography and the initial Gaussian are the same as in previous experiments. The transmitted wave for $\delta = 0.25$ results less attenuated (about 10% relative to the initial pulse height) and narrower than the one for $\delta = 0.5$. Moreover the delay is less appreciable in the former. For the mediums at hand we find that $\sigma \approx 0.0002$, $\mu \approx 0.001$ for $\delta = 0.25$ and $\sigma \approx 0.0009$, $\mu \approx 0.006$ for $\delta = 0.5$. See details on the computation of the scattering parameters in Appendix G. Recall that $\sigma$ is an effective diffusion coefficient as seen in approximation (2.78).

## 3.3 Disordered orography/ weakly-dispersive regime

In this section our goal is to validate approximation (2.60) for weakly dispersive waves governed by system (2.1). The nonlinearity parameter is let to be $\alpha = 0.001$.

In the first experiment we take a very weak dispersion $\beta = 0.0005$. The amplitude of the orography's fluctuations is $\delta = 0.5$ and its correlation length is $\ell = 0.1$. The irregulatities cover the interval [5,45]. Numerical parameters, computational domain are taken as in the hyperbolic case.

In the dispersive case the time of computation is somewhat higher (about 30 minutes) due to the extra change of variables $u \to V$ (c.f. equation (3.7), Chapter 3). When $\beta = 0$ this is not necessary.

We consider a rightgoing Gaussian-shaped disturbance as in Section 3.2. At the fixed medium station $\xi = 40$ (35 units of inhomogeneous channel) the transmitted wave is recorded in time and plotted in Figure 3.12(b). The linear theory (computed for a medium slab of length $X = 20$) accurately reproduces the numerical solution up to $\tau = 20$ approximately. Within this region the order of the maximum error is about $10^{-2}$.

Figures 3.12(a)-(b) also allow us to compare the purely dispersive regime (flat bottom) with the inhomogenous case, respectively. First observe an additional attenuation in the height of the pulse's crest in the latter (about 1) with respect to the former (about 1.5). In constant depth the attenuation is due only to dispersion.

In second place, in presence of orography the dispersive tail is readly destroyed (see Figure 3.12(b)). This fact can be explained through the concept of **localization** [46]. The localization length of a Fourier mode is a **characteristic propagation distance** after which the transmission coefficient is negligible. The bulk of the energy is in the reflected signal. Moreover high frequency components have small localization lengths. This means they are quickly filtered (back) by the disordered medium. In the context of the ODA theory this was phrased in a slightly different way by Berlyand and Burridge [9]. They called a layered random medium a **stratigraphic Gaussian filter**. As presented there, the transmitted wave can be written as the convolution of its initial pulse's Fourier content with a Gaussian kernel. The Gaussian kernel is the leading order approximation to the kernel in (2.60) with $\beta = 0$. Applying this notion to our current problem we have that disorder filters the higher part of the Fourier content of the pure dispersive solution shown with solid line in Figure 3.12(a). Hence the oscillatory tail (which is of high frequency content) has been converted into the incoherent part of the wave.

Next we increase substancially the dispersion parameter to $\beta = 0.002$ and repeat the above experiment. At this moment we point out that in the dispersive regime the initial pulse $f(\tau)$ to be used in computing the generalized ODA approximation (2.60) is no longer a Gaussian. In Figure 3.13(a) we visualize it in dashed line. A tail appears behind the pulse due to the model's dispersion.

In Figure 3.13(b) the ODA approximation for $X = 3$ and the numerical solution are compared. They coincide at high accuracy up to approximately $\tau = 7$. Again the attenuation enlarges with respect to the homogeneous case shown in Figure 3.13(a) in particular if we observe the envelope of the wave. Notice that the effect of the orography upon the attenuation mechanism is less noticeable for larger values of $\beta$. This is in agreement with equation (2.75) since coefficient $\lambda$ increases with the dispersion parameter $\beta$ as pointed out in Section 2.7.

Next increasing the medium slab to $X = 20$ the accuracy interval of the theoretical formula is extended to about $\tau = 12$ (see Figure 3.13(c)). We first observe a dispersive oscillatory tail (3 oscillations) followed by the disordered coda. The orography destroys the wave's dispersive coda beyond $\tau = 4$.

We remark that the accuracy within the interval $0 < \tau < 6$ has not been improved. Thus larger values of the $X$ parameter only adds new details to the coda in the ODA approximation. This was consistently observed in all experiments.

Extensive simulations were performed by increasing progressively the value of the dispersion parameter $\beta$. Here we only present the results for the dispersion parameters $\beta = 0.005$ and $\beta = 0.01$ in Figures 3.14 and 3.15, respectively. In all cases the linear theory is in perfect agreement with the small amplitude numerical solutions specially in the coherent part of the signal. We point out that the larger the value of $\beta$, the smaller the part of the coda captured by the generalized ODA approximation. Increasing the slab length $X$ does not improve the results in this case. This is due to fact that the frequency band of high accuracy of the approximation $a_\beta(x_o, \omega) \approx a_0(x_o, \omega)$ (see equation (2.61)) is decreased as $\beta$ increases.

For a broader pulse the ODA theory reproduces a very long segment of the coda even for high levels of dispersion. For instance, in Figure 3.16 a Gaussian of effective width $\ell_p \approx 6$ scatters over a disordered orography with correlation length $\ell = 0.6$ preserving the ratio inhomogeneities/wavelength as before. We also set $\delta = 0.5$ and $\beta = 0.05$. Observe that the incoherent coda is reproduced up to approximately $\tau = 40$ with $X = 20$ (compare with the pulse in Figure 3.15(b) for $\beta = 0.01$).

Next in Figure 3.17 we plot the transmitted pulse at four different stations in the medium together with the corresponding ODA approximations with $X = 20$. The dispersion parameter in this experiment is taken to be $\beta = 0.002$. Notice that in all medium stations the ODA approximation captures very well the shape of the coherent wave (the interval [-2,2] approximately) and still a segment of the oscillatory coda. The progressive attenuation, spreading and delay of the pulse are clearly observed in this sequence of plots.

In the next experiment we increase the nonlinearity parameter ten times $\alpha = 0.01$. Furthermore we set $\beta = 0.01$. In Figure 3.18 we compare the linear theory with the nonlinear numerical solution. As expected the main discrepancy between them is in the coherent wave's amplitude. This is more appreciable near the pulse's crest. We find that the ODA estimate gives a reasonable prediction even at this level of nonlinearity. Compare with Figure 3.15 over the time interval [-5,10] with the same level of dispersion. Note also that in this case the model's dispersion prevents the wave to develop a shock. Compare to the experiment in Figure 3.10 ($\beta = 0$) for a smaller value $\alpha = 0.005$.

Finally changes in the amplitude of the fluctuations are considered. In Figure 3.19 we plot at the same medium station $\xi = 30$ the transmitted pulses obtained over orographies with $\delta = 0.25$ and $\delta = 0.5$. The level of dispersion is fixed at $\beta = 0.005$ and the nonlinearity strength at $\alpha = 0.001$. Other parameters are the same in both experiments. Notice that in the former the overall attenuation and the delay are slightly smaller. These phenomena are more appreciable in the part of the oscillatory coda corresponding to the interval [1,10].

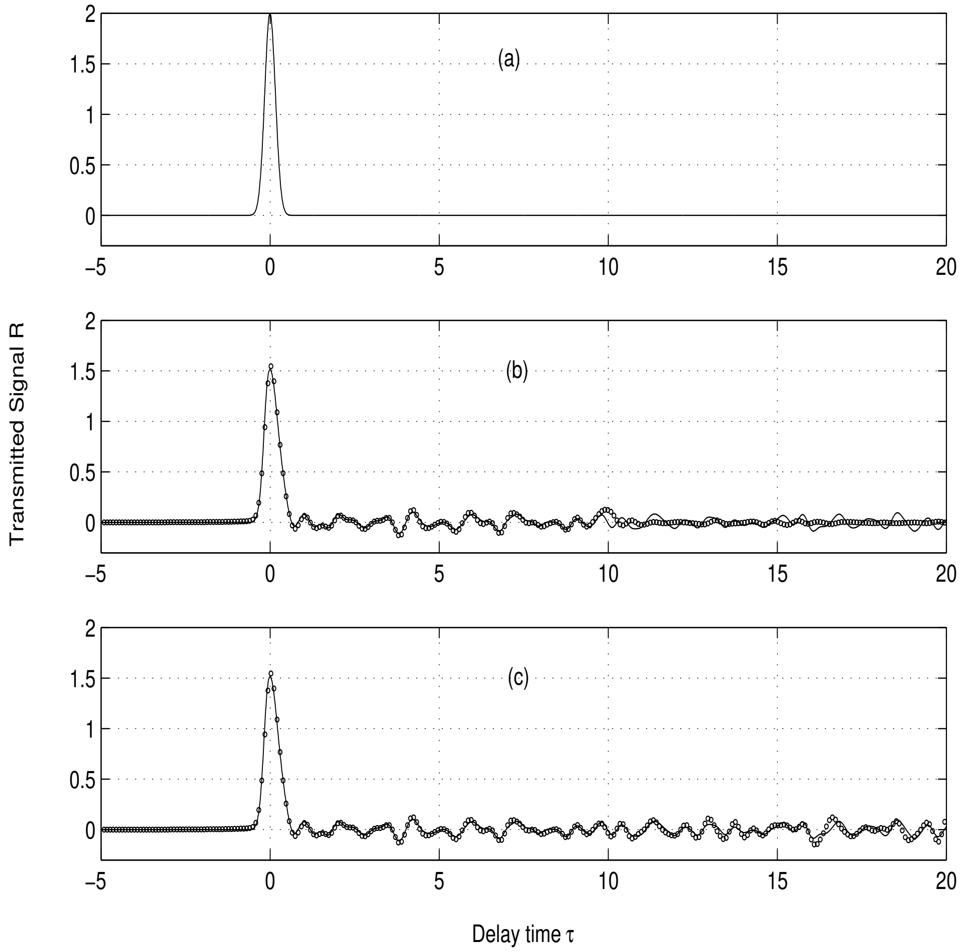


Figure 3.7: (a) Initial disturbance $R(0,\tau) = f(\tau) = 2e^{-\tau^2/0.05}$. (b) Pulse propagating over a synthetic disordered rapidly-varying topography. Solid line: Numerical solution for $\alpha = 0.001$, $\beta = 0$ at $\xi = 20$ (20 pulse widths). Dotted line : O'Doherty-Anstey approximation (2.62) for $X = 5$. (c) Same experiment as in (b) for $X = 20$. We see that the transmitted pulse is reproduced by approximation (2.62) for a longer delay time $\tau$.

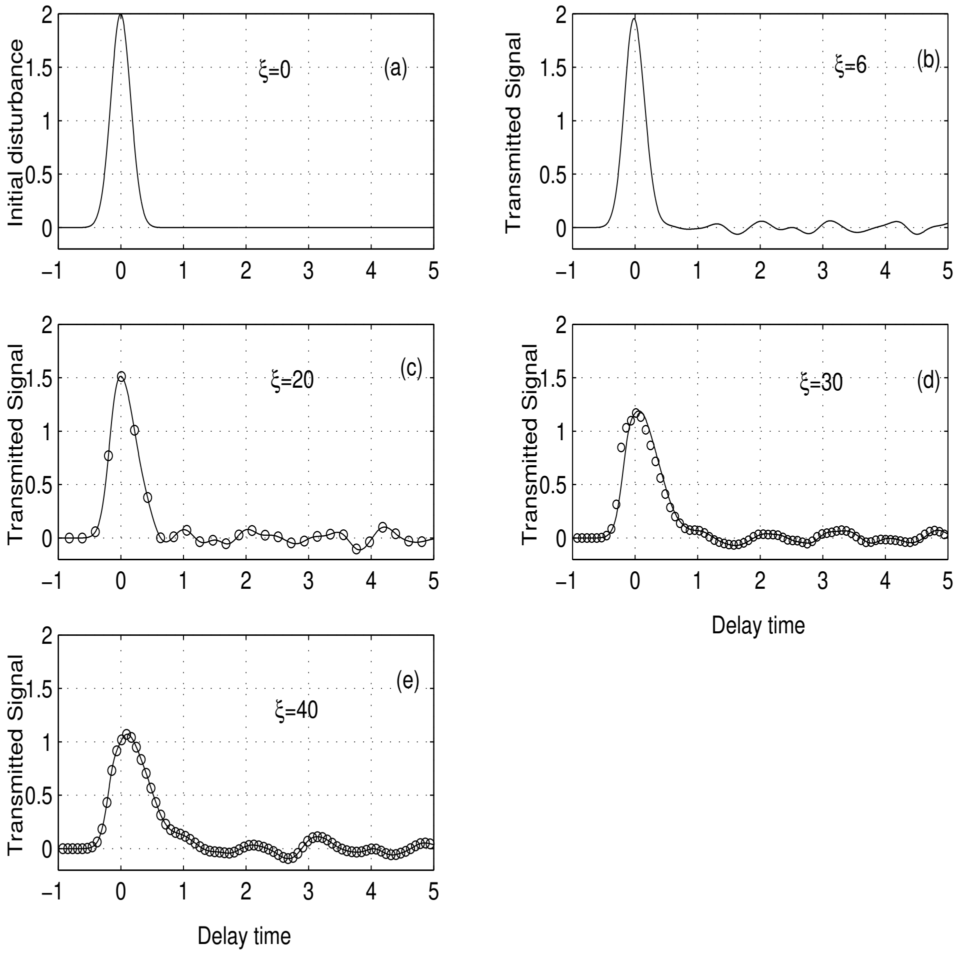


Figure 3.8: Transmitted signal at five different medium's locations for $\alpha = 0.001$ and $\beta = 0$. The numerical solution is in solid line and in (c), (d) and (e) the ODA approximation (2.62) with $X = 20$ is displayed in dotted line.

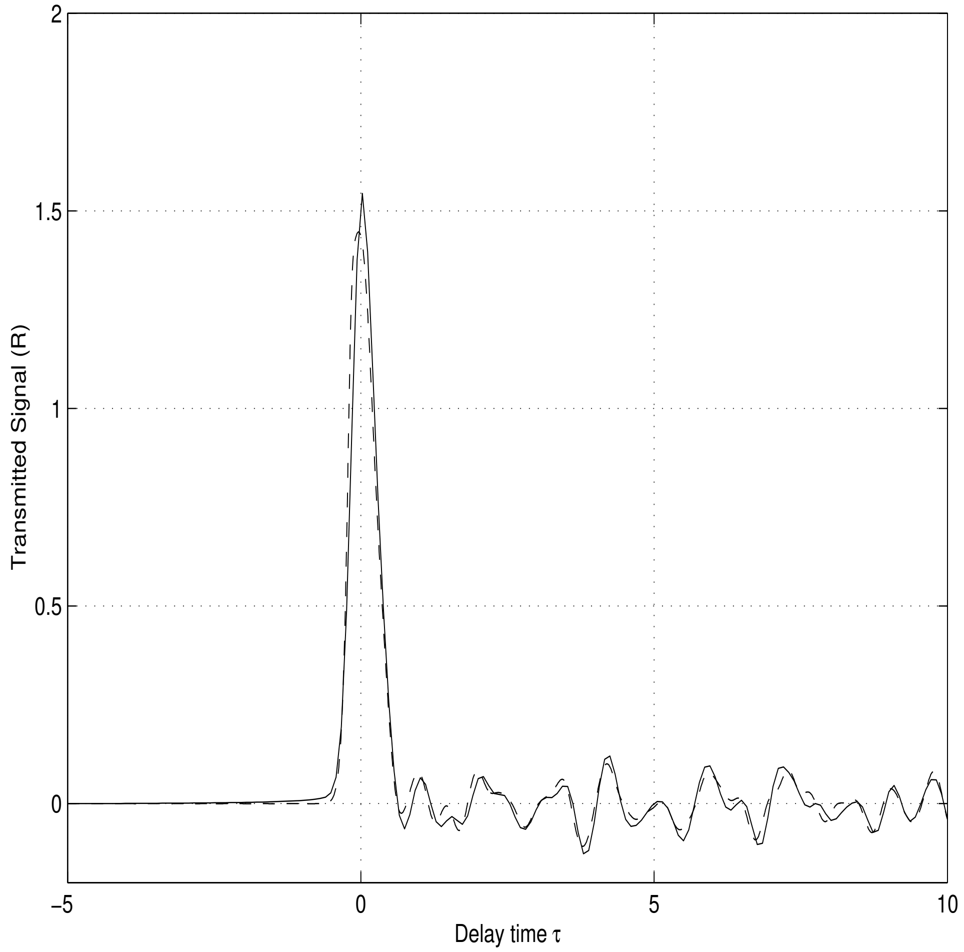


Figure 3.9: Pulse propagating over a synthetic disordered rapidly-varying topography. Dashed line: Numerical solution for $\alpha = 0.003$, $\beta = 0$ at $\xi = 20$ (20 pulse widths). Solid line : O'Doherty-Anstey approximation (2.62) for $X = 20$.

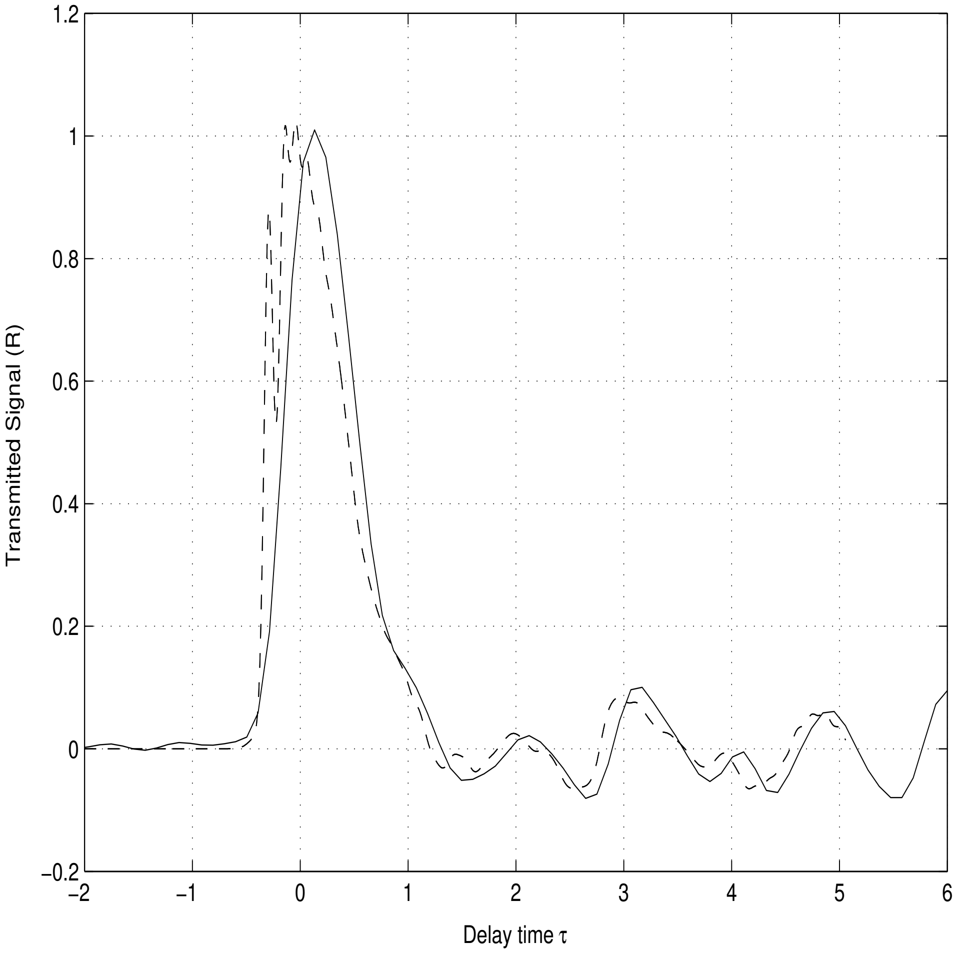


Figure 3.10: Pulse propagating over a synthetic disordered rapidly-varying topography. Dashed line: Numerical solution for $\alpha = 0.005$, $\beta = 0$ at $\xi = 50$ (50 pulse widths). Solid line : O'Doherty-Anstey approximation (2.62) for $X = 20$.

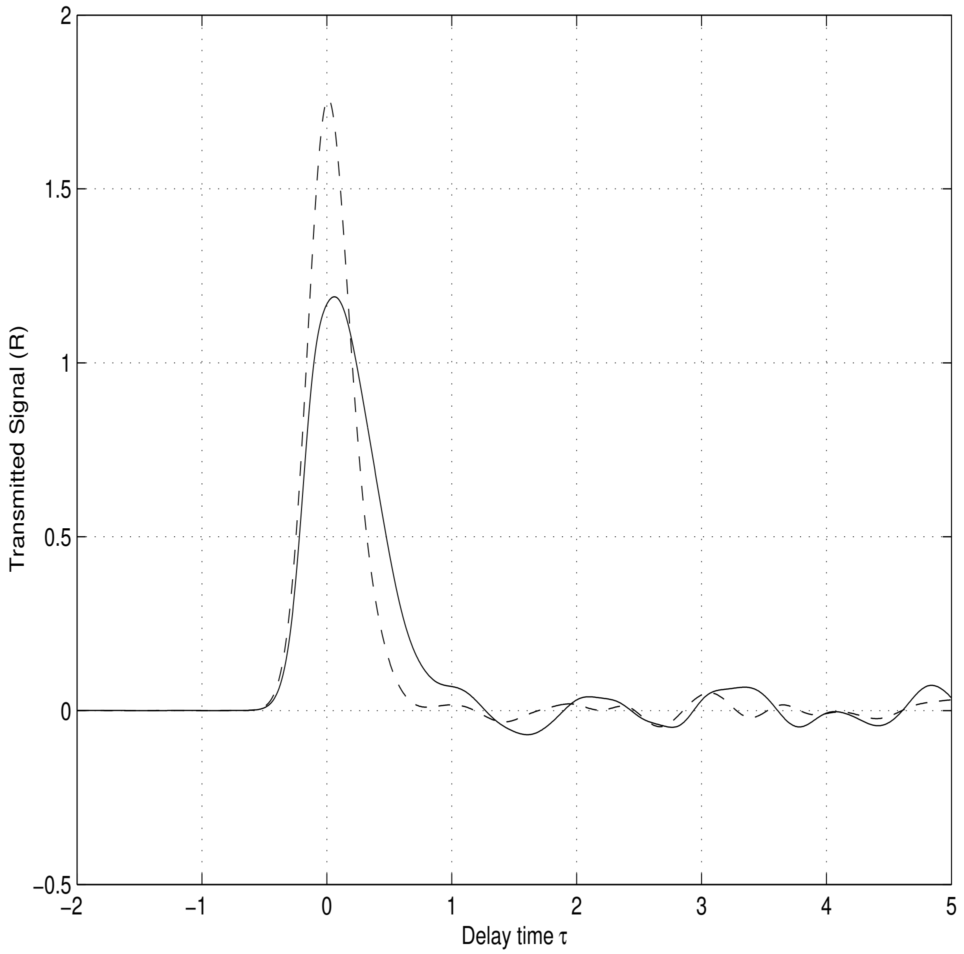


Figure 3.11: Pulse propagating over two realizations of synthetic orographies. For the pulse with solid line the amplitude of the orography's fluctuations is $\delta = 0.5$. For the pulse in dashed line $\delta = 0.25$. Model parameters : $\alpha = 0.001$, $\beta = 0$ and the medium's position is $\xi = 30$.

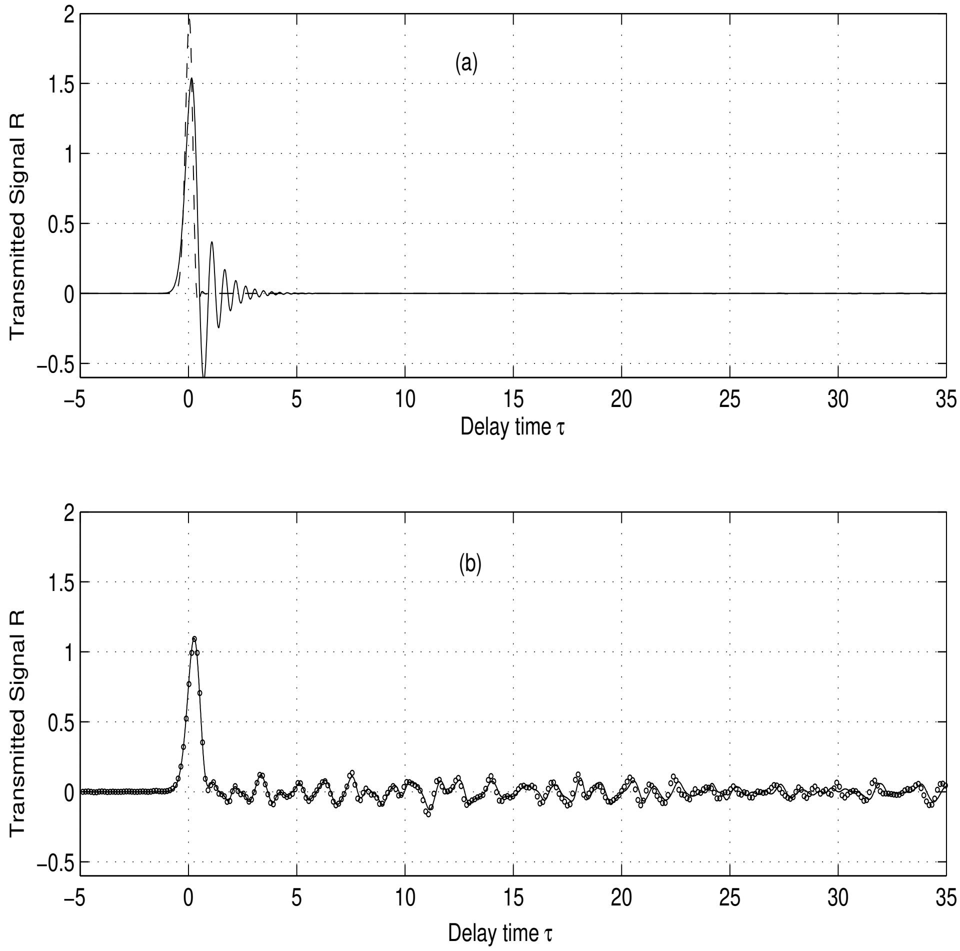


Figure 3.12: (a) Dashed line : Initial disturbance. Solid line : Solution for $M \equiv 1$ (flat bottom), $\alpha = 0.001$, $\beta = 0.0005$ at $\xi = 40$ (40 pulse widths). (b) Pulse propagating over a synthetic disordered rapidly-varying orography. Solid line : Numerical solution. Parameters are the same as in (a). Dotted line : Generalized O'Doherty-Anstey approximation (2.60) for $X = 20$.

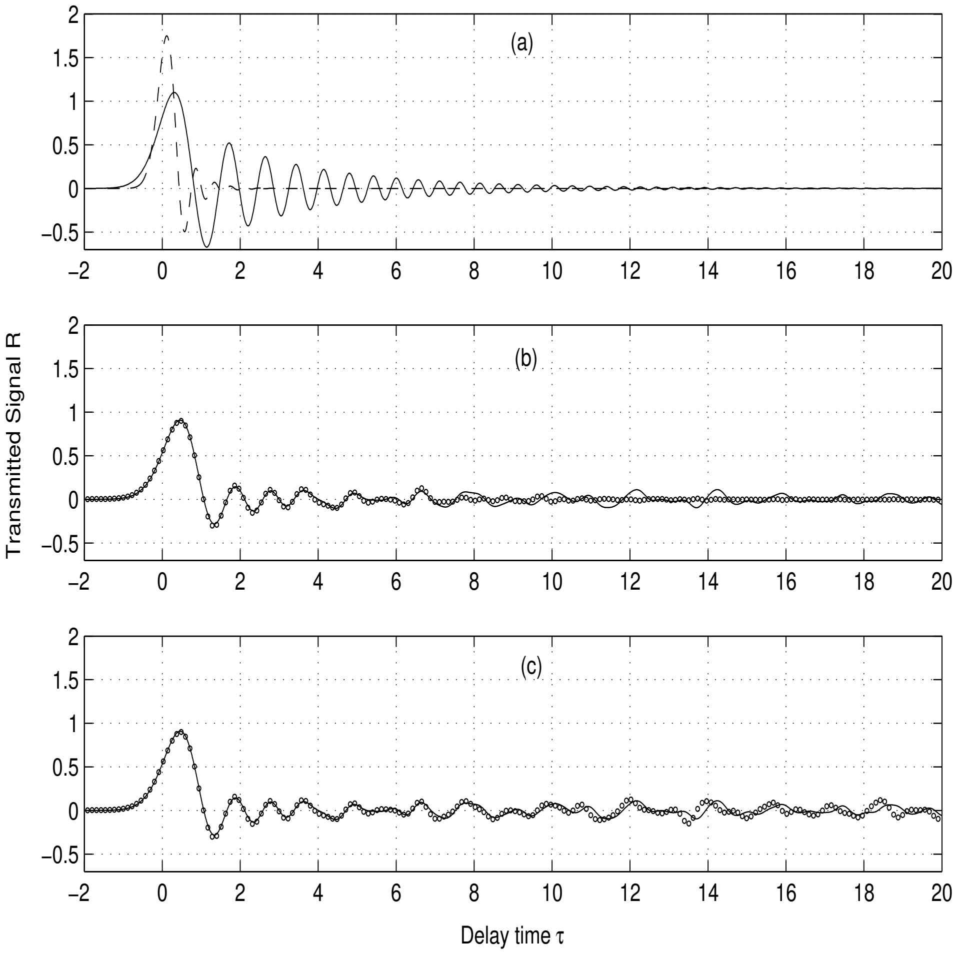


Figure 3.13: (a) Dashed line : Initial disturbance. Solid line : Solution for $M \equiv 1$ (flat bottom), $\alpha = 0.001$, $\beta = 0.002$ at $\xi = 40$. (b) Pulse propagating over a synthetic disordered rapidly-varying orography. Solid line : Numerical solution. Parameters are the same as in (a). Dotted line : Generalized O'Doherty-Anstey approximation (2.60) for $X = 3$. (c) The same experiment as in (b) but the ODA approximation is calculated for $X = 20$.

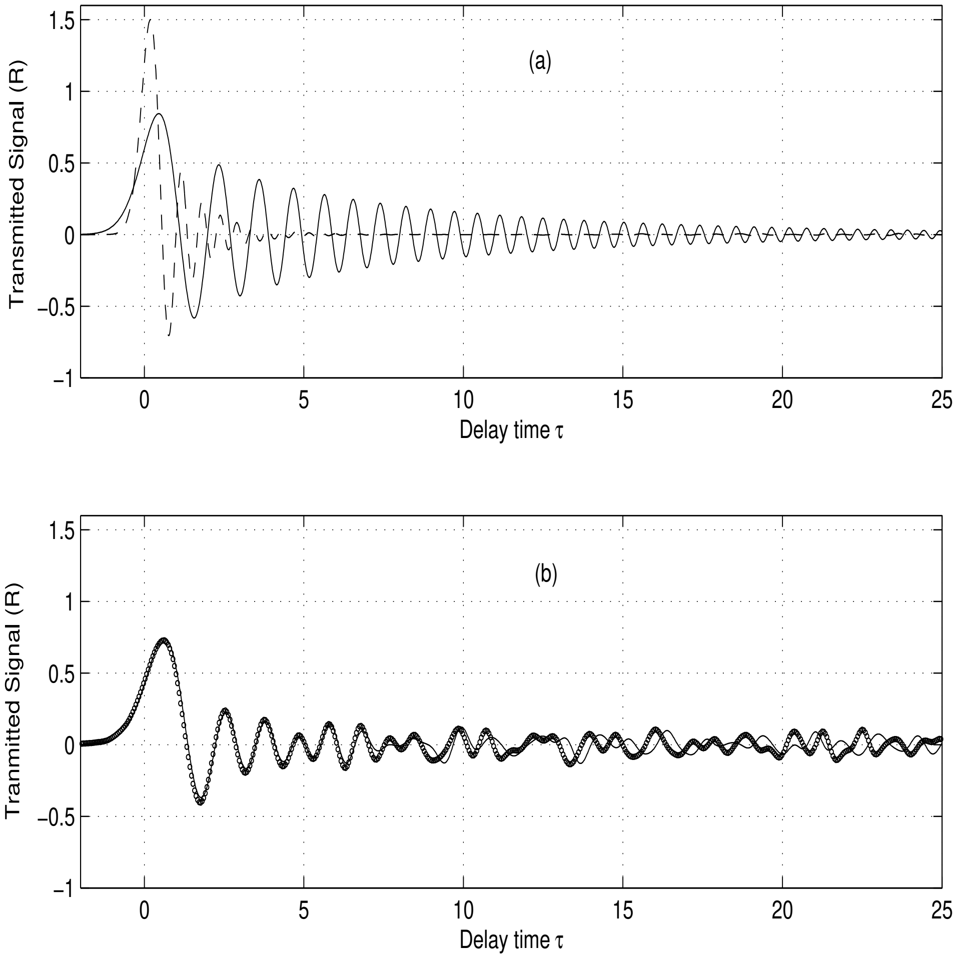


Figure 3.14: (a) Dashed line : Initial disturbance. Solid line : Solution for $M \equiv 1$ (flat bottom), $\alpha = 0.001$, $\beta = 0.005$ at $\xi = 40$. (b) Pulse propagating over a synthetic disordered rapidly-varying orography. Solid line : Numerical solution. Parameters are the same as in (a). Dotted line : Generalized O'Doherty-Anstey approximation (2.60) for $X = 20$.

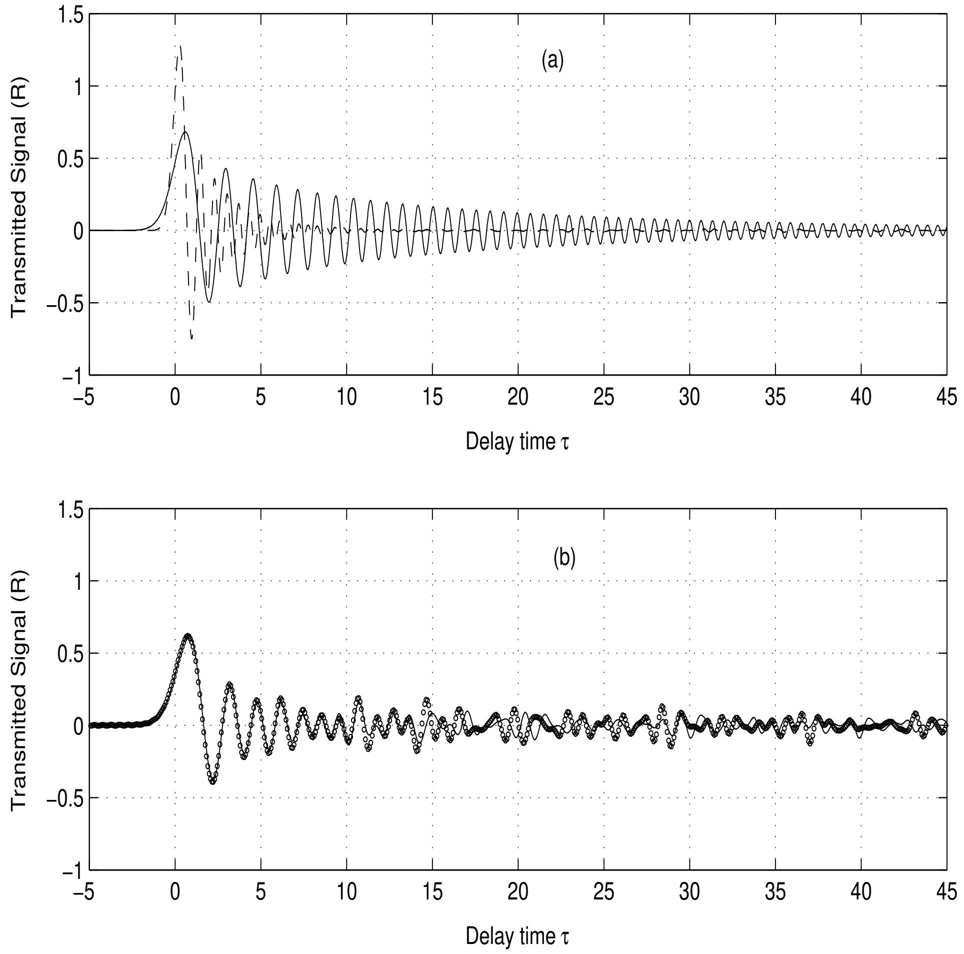


Figure 3.15: (a) Dashed line : Initial disturbance. Solid line : Solution for $M \equiv 1$ (flat bottom), $\alpha = 0.001$, $\beta = 0.01$ at $\xi = 40$. (b) Pulse propagating over a synthetic disordered rapidly-varying orography. Solid line : Numerical solution. Parameters are the same as in (a). Dotted line : Generalized O'Doherty-Anstey approximation (2.60) for $X = 20$.

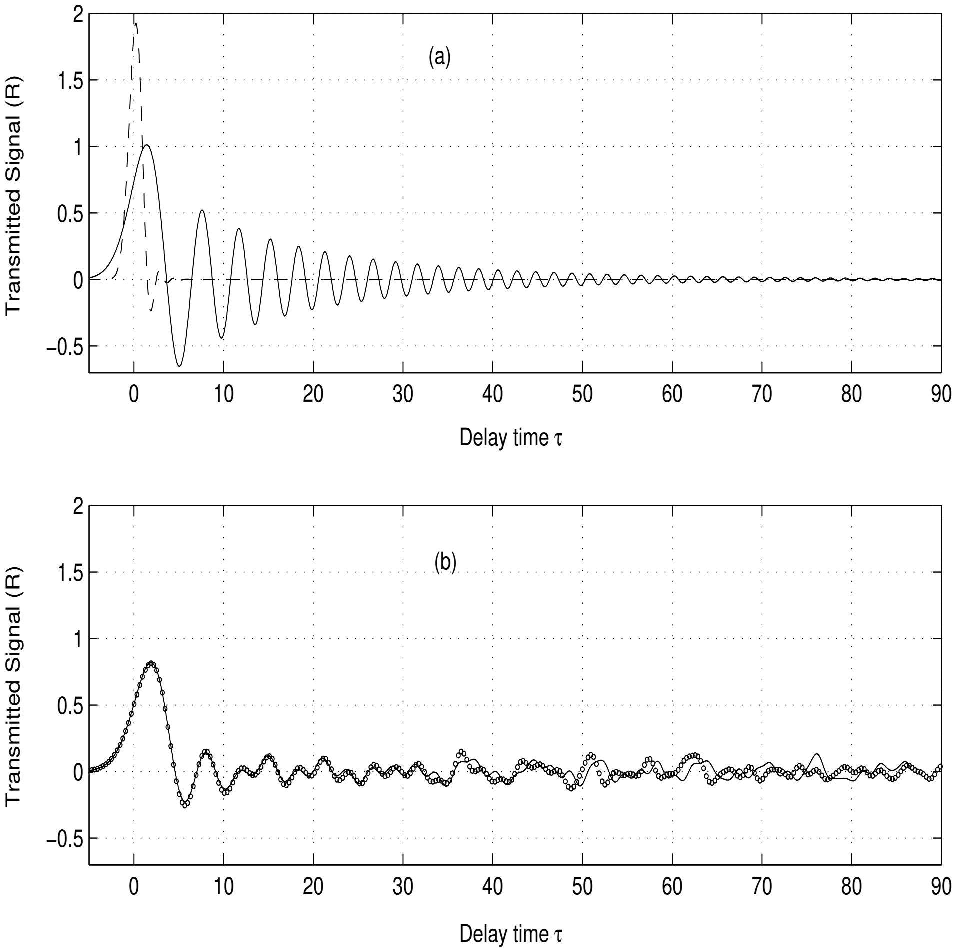


Figure 3.16: (a) Dashed line : Initial disturbance. Solid line : Solution for $M \equiv 1$ (flat bottom), $\alpha = 0.001$, $\beta = 0.05$ at $\xi = 150$. (b) Pulse propagating over a synthetic disordered rapidly-varying orography. Solid line : Numerical solution. Parameters are the same as in (a). Dotted line : Generalized O'Doherty-Anstey approximation (2.60) for $X = 20$. Effective pulse width $\ell_p \approx 6$.

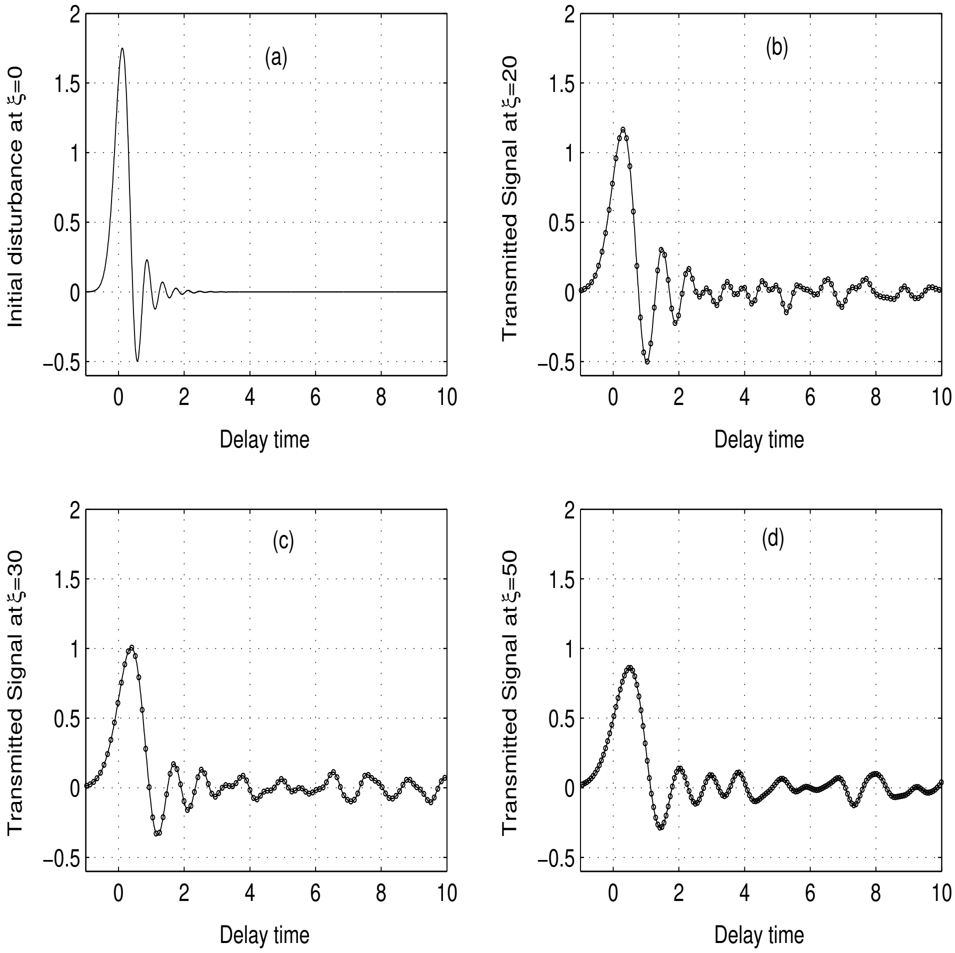


Figure 3.17: Pulse propagating over a synthetic disordered rapidly-varying topography at four different medium's locations for $\alpha = 0.001$ and $\beta = 0.002$. The numerical solution is in solid line and the generalized ODA approximation (2.60) with $X = 20$ is plotted in dotted line.

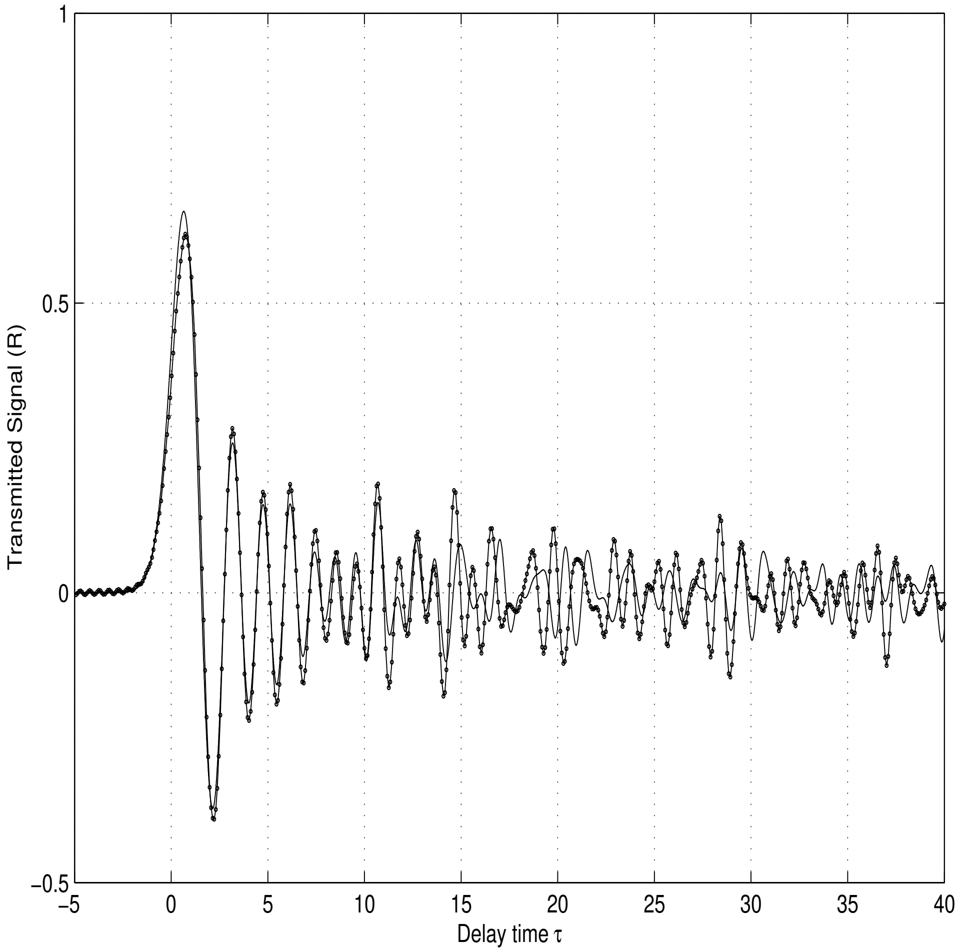


Figure 3.18: Pulse propagating over a synthetic disordered rapidly-varying topography at $\xi = 40$ for $\alpha = 0.01$ and $\beta = 0.01$. The numerical solution is in solid line and the generalized ODA approximation (2.60) with $X = 20$ is plotted in dotted line.

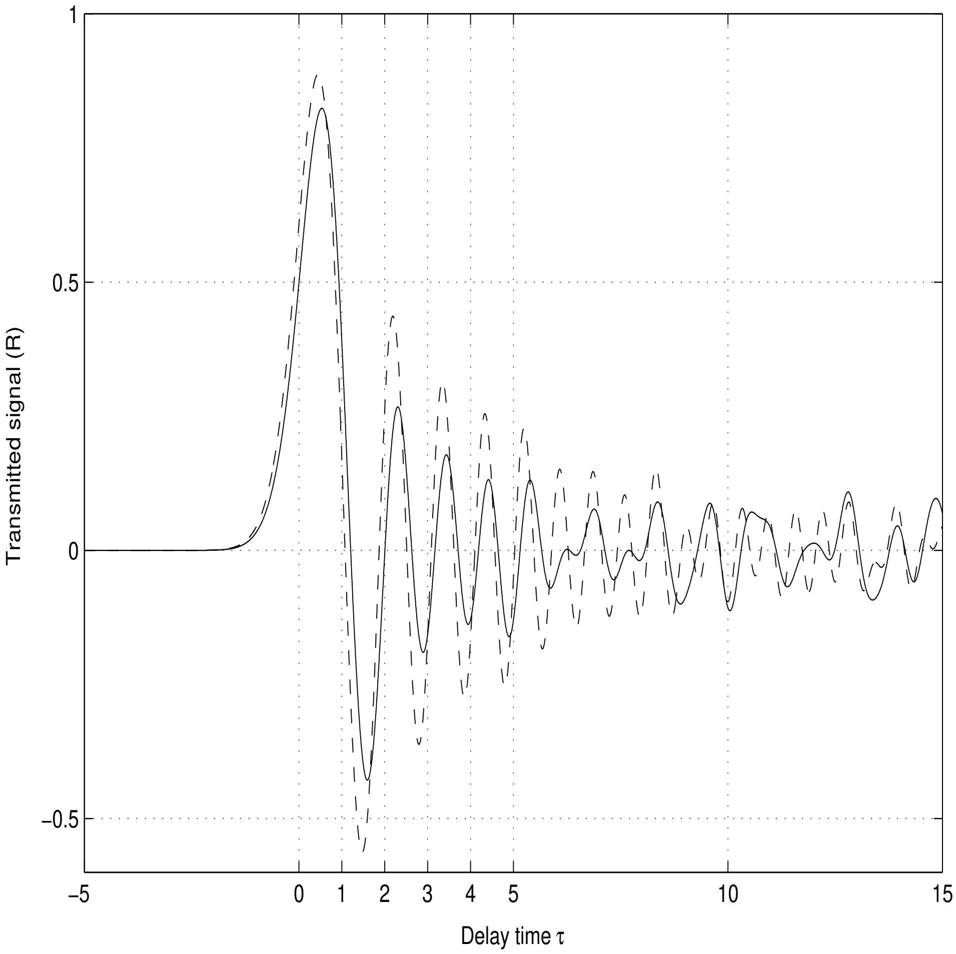


Figure 3.19: Pulse propagating over two realizations of synthetic orographies. For the pulse with solid line the orography's fluctuations amplitude is $\delta = 0.5$. For the pulse in dashed line $\delta = 0.25$. Model parameters: $\alpha = 0.001$, $\beta = 0.005$ and the medium's position is $\xi = 30$.

## 3.4 The generalized O'Doherty-Anstey approximation for solitary waves

After verifying the high accuracy of the generalized ODA approximation through several numerical experiments in the case of Gaussian-shaped pulses we are ready to extend our results to solitary waves in the form of (3.3). As we have already said, these are approximate solutions of the nonlinear Boussinesq system (3.1) when $M \equiv 1$ (flat bottom). Furthermore such pulses travel without changing their form. In our experiments we found that they propagate with constant speed provided that $O(\alpha) \approx O(\beta) < 0.1$. This balance prevents the formation of a dispersive tail in the wave. Moreover at this level of dispersion and nonlinearity the (effective) propagation velocity of the soliton is bounded (about unity) and thus the pulse-shaping theory developed in Chapter 2 (in particular the invariant imbedding technique) can be applied.

We will increase progressively the levels of nonlinearity and dispersion in the model in order to study the role of nonlinear effects in the shape of the soliton and determine up to where our linear theory gives a reasonable prediction.

The initial soliton (in space) is located at position $\xi_o = -5$ at time $t_o = \xi_o/C$ and therefore the initial soliton from the theoretical formula (2.60) is of the form

$$f(\tau) = \left(\frac{1}{C^2} + \frac{1}{C}\right) \operatorname{sech}^2(B\tau) + \frac{\alpha}{C^2} \operatorname{sech}^4(B\tau). \tag{3.14}$$

Recall that $C = \sqrt{1+\alpha}$ is the soliton's propagation speed (c.f. equation (3.12)). To start we set $\alpha = \beta = 0.001$. The initial soliton (3.14) is graphed in Figure 3.20(a). Since it is broader ($\ell_p \approx 6$) than the Gaussian in previous experiments, the orography's correlation length is taken to be $\ell = 0.6$ to preserve the ratio inhomogeneities/wavelength as 1/10. The orography's irregularities cover the interval [5,245] and its amplitude is $\delta = 0.5$. The numerical parameters are $J = 14000$, $N = 17000$, $\Delta\xi = 0.0186$, $\Delta t = 0.014$ and the computational domain is [-10,250]. The time of computation of each experiment is about 30 minutes. The station of observation in the medium is located at $\xi = 150$ (25 pulse widths).

See Figure 3.20(b) where we compare the ODA approximation (2.60) for $X = 10$ and $\beta = 0.001$ with the weakly-nonlinear, weakly-dispersive numerical solution. The linear ODA theory gives excellent prediction up to the value $\tau = 25$ approximately. In Figure 3.20(c) the slab length parameter $X$ is enlarged three times. We find that the deterministic formula (2.60) (using approximation (2.61)) captures up to roughly $\tau = 55$.

After travelling a distance of 150 units the pulse's amplitude decays to about 40% with respect to the initial height of the soliton. The broadening and the delay are also observed in this experiment.

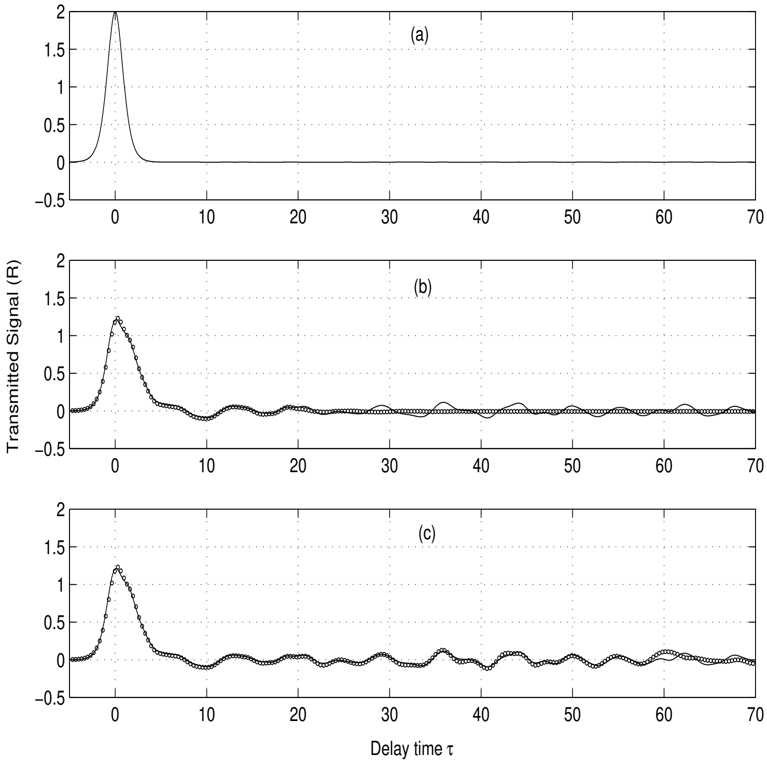


Figure 3.20: (a) Initial soliton $f(\tau)$. (b) Soliton propagating over a synthetic disordered rapidly-varying orography. Solid line : Numerical solution for $\alpha = \beta = 0.001$, at $\xi = 150$ (25 pulse widths). Dotted line : Generalized O'Doherty-Anstey approximation (2.60) for $X = 10$. (c) Same experiment as in (b) but the ODA approximation is computed with $X = 30$.

In Figures 3.21 and 3.22 we show the results obtained by increasing simultaneusly the values of nonlinearity and dispersion to $\alpha = \beta = 0.005$ and then $\alpha = \beta = 0.01$. The accuracy of the ODA theory is gradually decreasing specially near the peak of the pulse where nonlinear effects first arise. In contrast, the disordered coda is even captured with reasonable accuracy in particular for $\alpha = 0.005$. In Figure 3.22(b) the numerical solution appears sligthly shifted to the left and taller than the linear prediction. These effects are more accentuated for larger values of $\alpha$. At this point we have reached the limit of application of the linear theory. We contrast the soliton in Figure 3.21 with the Gaussian pulse in the hyperbolic experiment ($\beta = 0$) shown in Figure 3.10 with same level of nonlinearity. Note that in the latter a shock formation was identified. On the contrary here the weak dispersion ($\beta = 0.005$) prevents the breaking of the soliton. These results motivate the development of

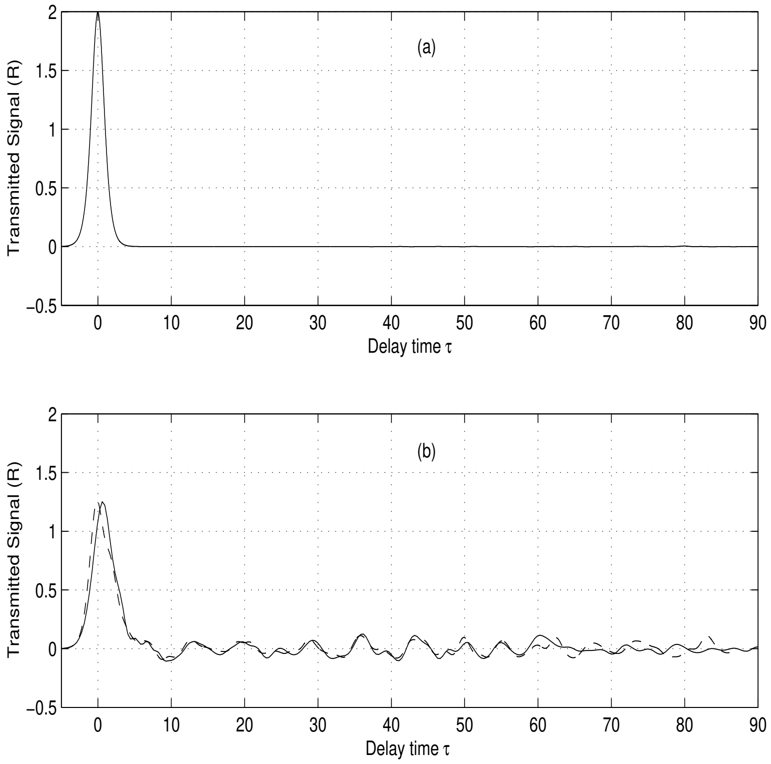


Figure 3.21: (a) Initial soliton. (b) Soliton propagating over a disordered rapidly-varying orography. Dashed line : Numerical solution for $\alpha = \beta = 0.005$ at $\xi = 150$ (25 pulse widths). Solid line : Generalized O'Doherty-Anstey approximation (2.60) for $X = 30$.

a full nonlinear theory which explains satisfactorily the new phenomena observed in solitary waves.

## 3.5 Pulse-shape stabilization

Approximation (2.60) depends on the particular orography's realization considered through the metric coefficient $M(\xi)$. However the **stabilization property** makes the ODA theory very robust. It is found that the transmitted coherent front stabilizes to a deterministic shape which is independent of the particular medium realization when observed relative to its corresponding first arrival time (travel time) up to a fixed observation station into the medium. This phenomenon is observed at large distances from the disturbance's source and is of great interest because in a real situation the properties of a particular medium are not

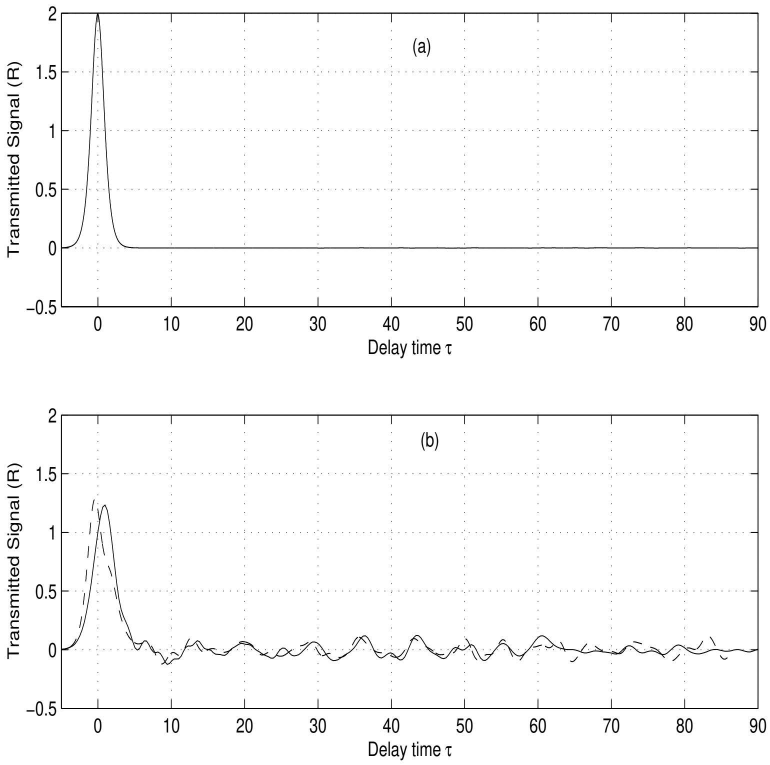


Figure 3.22: (a) Initial soliton $f(\tau)$. (b) Soliton propagating over a synthetic disordered rapidly-varying orography. Dashed line : Numerical solution for $\alpha = \beta = 0.01$ at $\xi = 150$ (25 pulse widths). Solid line : Generalized O'Doherty-Anstey approximation (2.60) for $X = 30$.

exactly known due to errors introduced in by the measurement devices employed.

The stabilization property in disordered media is studied for acoustic models in one dimension in [32] and extended to multiple dimensions in [35] by using probabilistic techniques. Stabilization is usually proved using stochastic modelling to show that the variance of the pulse shaping process tends to zero in the appropriate limit [50]. Here we will give strong evidence of this fact, which has never been proved for weakly-dispersive, weakly nonlinear waves. We consider both Gaussian-shaped pulses and solitary waves as initial disturbances.

The first case under study is $\alpha = 0.001$ and $\beta = 0.0005$. Ten different realizations of the synthetic disordered orographies (defined as in (3.13)) are considered in this experiment. In all of them the amplitude of the fluctuation is $\delta = 0.5$, the correlation length is $\ell = 0.1$ and the fluctuations are located over the interval [0,45]. The realizations only differ from each other in the noise functions $n(\xi)$ which are constructed by using different random number sequences.

A rightgoing Gaussian located at $\xi_o = -5$ is let to propagate alternatively over each orography and recorded in time at the same medium station $\xi = 40$. In Figure 3.23 we superimpose the traces of the resulting pulses. Observe that the shape of the wave's coherent front (approximately within the time interval $[-\infty, 1]$) varies very little from one realization to another. The maximum difference is about 0.1 near the peak. In contrast, the pulse's incoherent coda does not exhibit a defined structure and depends highly on the particular realization of the orography.

We remark that the pulse only stabilizes when it is observed in the travel time frame. To corroborate this in Figure 3.24 we graph the same pulses as in Figure 3.23 but now as a function of the clock time $t$. Note that the time of arrival of each pulse at the fixed medium station fluctuates around $t = 40$ and the stabilization does not take place.

Next we repeat the experiment above but increasing the dispersion parameter ten times ($\beta = 0.005$). Other parameters are left unchanged. The results are presented in Figure 3.25. Again we have the stabilization of the coherent signal within the time interval $[-\infty, 5]$ which is not readly filtered by the medium because this part of the wave is broad. In the interval [1.5,5] the variation of the pulses is higher (about 0.2). Beyond $\tau = 5$ we find their disordered codas.

Finally we regard the case of rightgoing solitary waves of the form of (3.3). The levels of nonlinearity and dispersion are set to $\alpha = \beta = 0.002$. In all of ten orographies considered here the fluctuations are located over the interval [0,245], their amplitude is $\delta = 0.5$ and its correlation length is taken to be $\ell = 0.6$. In Figure 3.26 we plot the transmitted pulses recorded at a distance of 150 units to the rightside of the origin (corresponding approximately to 25 pulse widths). The stabilization is observed within the time interval $[-\infty, 4]$ but now the variation of the transmitted traces appears to be higher than for the Gaussian profile in Figure 3.23. This is more noticeable within the interval [1,4].

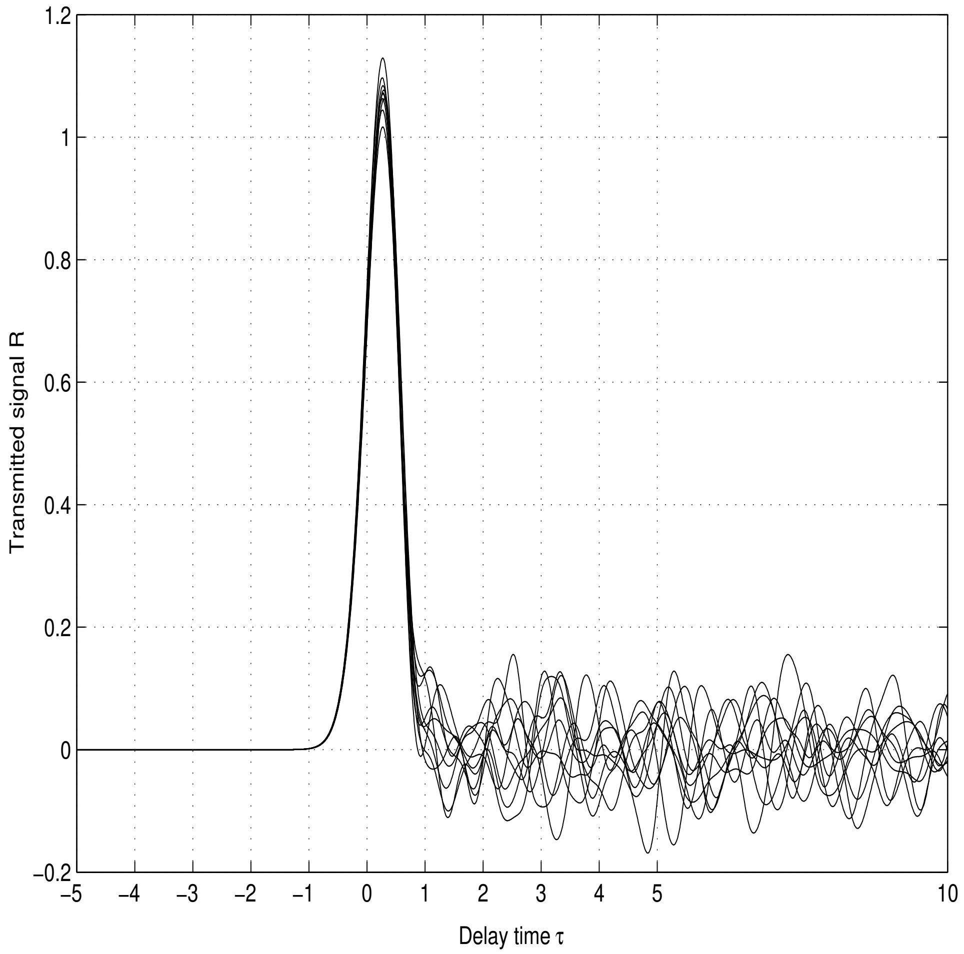


Figure 3.23: Transmitted pulse shape stabilization observed at the fixed medium's station $\xi = 40$ (40 pulse widths). This plot is obtained by propagating a Gaussian pulse over ten different realizations of synthetic orographies. Each trace corresponds to a realization. The model parameters are $\alpha = 0.001$ and $\beta = 0.0005$.

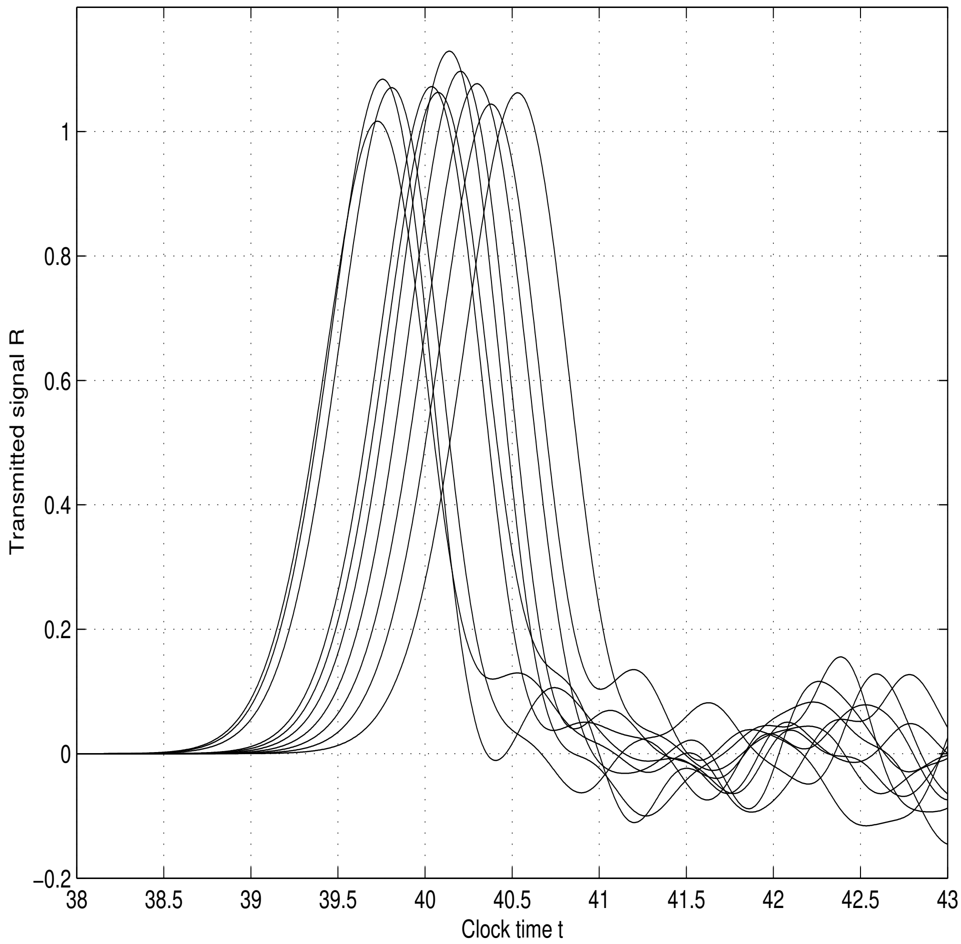


Figure 3.24: The same as in Figure 3.23 but now the pulses are graphed in the clock time $t$. The stabilization is not observable in this case.

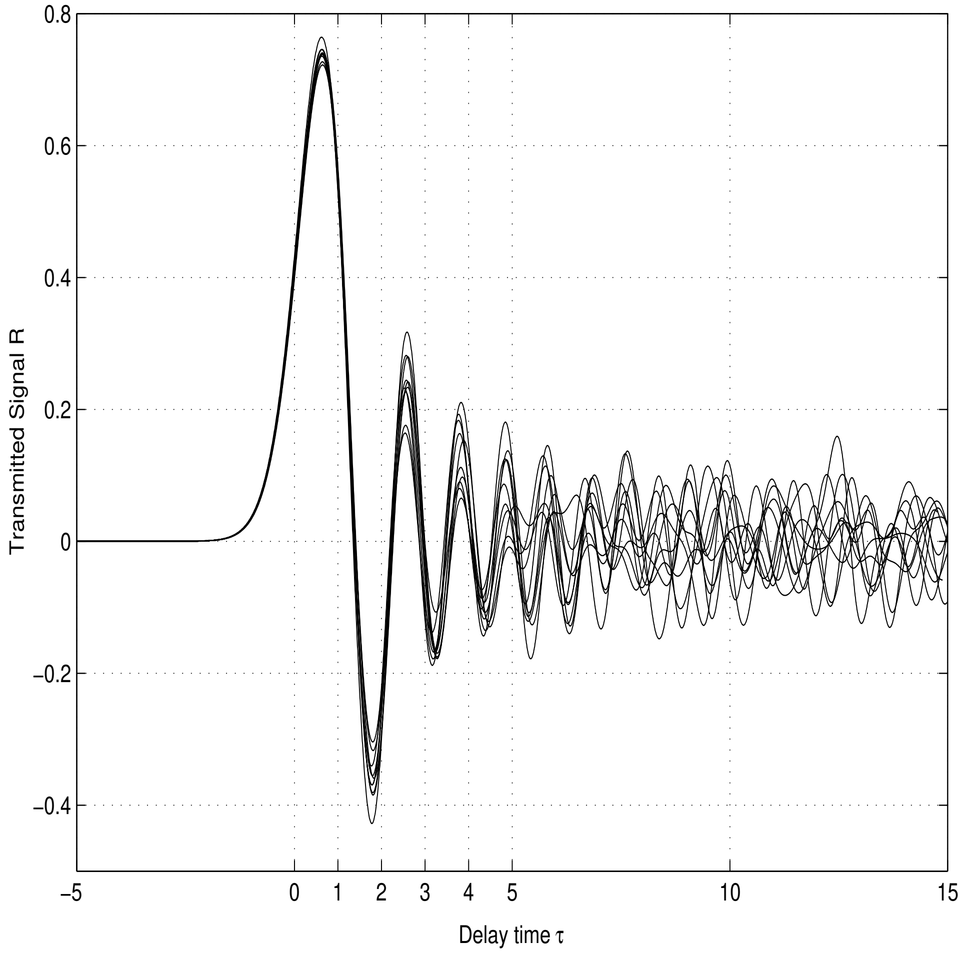


Figure 3.25: Pulse shape stabilization for the dispersion parameter $\beta = 0.005$. Other parameter are equal to those indicated in Figure 3.23.

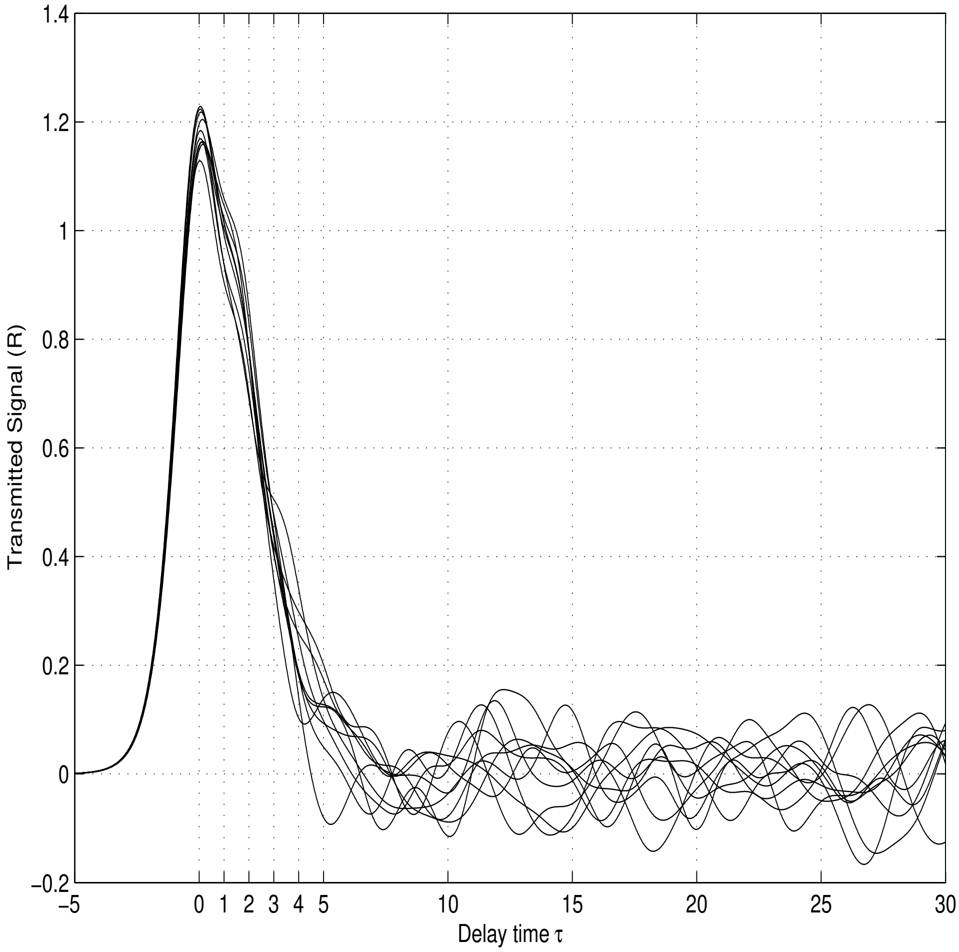


Figure 3.26: Transmitted pulse shape stabilization observed at the fixed medium's station $\xi = 150$ (25 pulse widths). This plot is obtained by propagating a solitary wave over ten different realizations of synthetic orographies. The model parameters are $\alpha = \beta = 0.002$.

## 3.6 Numerical computation of the coefficient $M(\xi)$

As mentioned earlier, computation of the orography-dependent coefficient $M(\xi)$ in large channels is a complex procedure since it requires the solution of a costly change of variable problem. This is exactly the case of the ODA theory because the effect of the orography fluctuations is only appreciable over long propagation distances of order $20\ell_p$ (twenty times the typical wavelength) approximately. This is the reason for which we have synthetized the coefficient $M(\xi)$ instead of computing it directly from the orography data. Through this strategy we validated the pulse-shaping theory by exhaustive numerical simulations. All phenomena of interest were observed.

Throughout this section the variable $x$ will denote the spatial coordinate in the physical domain. Here we wish to validate the ODA theory for a piecewise linear orography of the form

$$h(x) = 1 + \delta n(x/\ell), \tag{3.15}$$

when the length $L_o$ of the irregular section is up to fifteen times the typical wavelength ($L_o = 15\ell_p$). In this case the coefficient $M(\xi)$ can be computed by using Driscoll's package [18] developed for MATLAB which is based on the Schwarz-Christoffel transformations [2]. In the orography (3.15), $n(x)$ is the function describing the bottom's irregularities constructed as in Section 3.2.

First let $Z_1(\xi, \tilde{\zeta}) = x(\xi, \tilde{\zeta}) + i\tilde{y}(\xi, \tilde{\zeta})$ denote the conformal transformation which maps the bi-infinite strip $S_2$ onto the infinite polygonal domain $S_1$ satisfying that $Z_1(\pm\infty) = \pm\infty$ and $Z_1(-\sqrt{\beta}i) = -\sqrt{\beta}i$ (see Figure 3.27(B)-(D)). This map exists and is unique by the Riemann mapping theorem [2]. Then in Nachbin [45] it is shown that

$$M(\xi, \beta) = \frac{\partial \tilde{y}}{\partial \tilde{\zeta}}(\xi, 0)$$

or equivalently by the Cauchy-Riemann equations

$$M(\xi, \beta) = \frac{\partial x}{\partial \xi}(\xi, 0).$$

Here we make explicit the geometric dependence of function $M$ on the parameter $\beta$. This arises from the scale $\sqrt{\beta}$ in the domains $S_1$ and $S_2$ to be mapped (see Figure 3.27(B)-(D)). The Schwarz-Christoffel transformation has been scaled to account for the long wave regime under consideration. The fact that coefficient $M$ depends on the parameter $\beta$ adds an extra difficulty in its numerical evaluation because the conformal mapping $Z_1$ must be recomputed when $\beta$ is changed. Details are given in Nachbin [45].

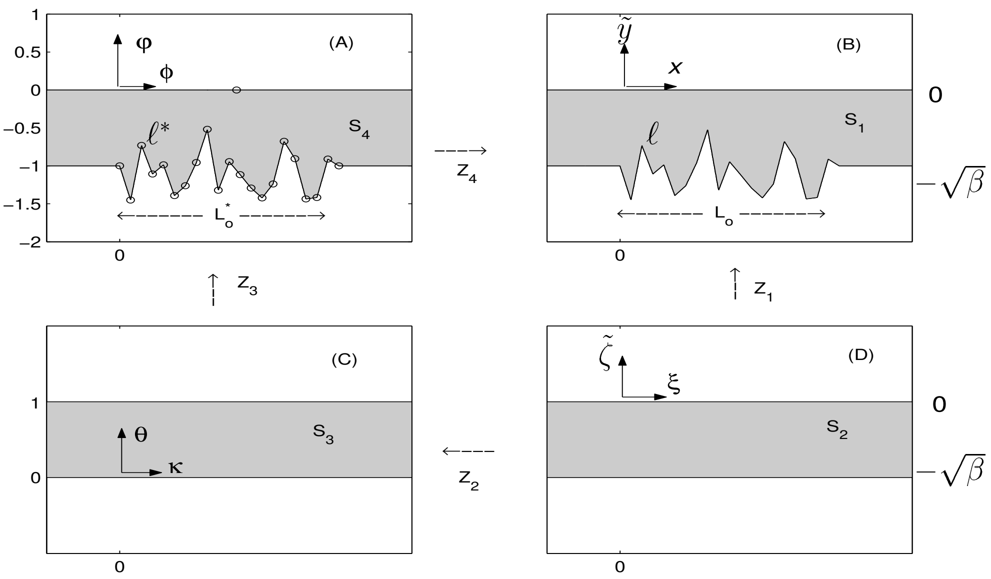


Figure 3.27: Scheme of change of variables for computing coefficient $M(\xi, \beta)$. The correlation lengths in (A) and (B) are related by $\ell^* = \ell/\sqrt{\beta}$ and the total length of the irregular sections by $L_o^* = L_o/\sqrt{\beta}$. The vertices necessary in computing map $Z_3$ are indicated in (A) with dots.

Note that the width of regions $S_1$ and $S_2$ is small when $\beta << 1$. Thus to avoid numerical difficulties we rescale them by the factor $\sqrt{\beta}$ through the change of variables

$$Z_2 \quad : \quad \kappa = \frac{\xi}{\sqrt{\beta}}, \quad \theta = \frac{\tilde{\zeta} + \sqrt{\beta}}{\sqrt{\beta}},$$

and

$$Z_4 \quad : \quad x = \sqrt{\beta}\,\phi, \quad \tilde{y} = \sqrt{\beta}\,\varphi.$$

Moreover, $Z_3$ is the map transforming the bi-infinite unit strip $S_3$ onto the interior of the polygonal region $S_4$. In such a way that we have that $Z_1 = Z_4 \circ Z_3 \circ Z_2$, where the symbol $\circ$ denotes the composition operator (see Figure 3.27). Note that in this way, we have that $Z_3(0) = -i$.

Then it is easy to see that

$$x(\xi, \tilde{\zeta}) = \sqrt{\beta}\,\phi\left(\frac{\xi}{\sqrt{\beta}}, \frac{\tilde{\zeta} + \sqrt{\beta}}{\sqrt{\beta}}\right), \tag{3.16}$$

and

$$M(\xi, \beta) = \frac{\partial \phi}{\partial \kappa} \left( \frac{\xi}{\sqrt{\beta}}, 1 \right). \tag{3.17}$$

Thus to compute $M(\xi, \beta)$ it suffices to evaluate the map $Z_3$ transforming region $S_3$ onto region $S_4$ (see Figure 3.27(A)-(C)).

For the unit strip Driscoll's package [18] provides the macro commands **stripmap** and **eval** for MATLAB which compute directly $Z_3$ as a Schwarz-Christoffel type transformation and the routine **evaldiff** to calculate its first-order derivatives. It uses a modification of the standard Schwarz-Christoffel formula [2].

In a first step, by using the command **stripmap**, Driscoll's package finds the corresponding pre-images in the unit strip $S_3$ of each vertex on the polygonal boundary of domain $S_4$. In the schematic figure 3.27(A) these vertices in the target domain are indicated with big dots. One additional vertex is necessary in order to fix the upper border $\varphi = 0$ of the channel. The prevertices are computed by solving a system of nonlinear equations which is accomplished by means of an iterative method. Hence the time of computation increases with the number of orography vertices. It takes roughly three hours of computation in the case of the orography shown in Figure 3.28(A) with dashed line. Its correlation length is $\ell = 0.1$, the amplitude of fluctuations is $\delta = 0.5$, the total length of the inhomogeneous section is $L_o = 15$ and $\beta = 0.01$. The orography's irregularities are located within the interval [0,15]. The total number of vertices used for this orography is 153 including the already fixed $-i$.

Notice that here the target domain for the Schwarz-Christoffel map $Z_3$ is an elongated region of length $L_o^* = L_o/\sqrt{\beta} = 150$ (see Figure 3.27(A)) which increases as $\beta \to 0$. Several numerical experiments showed that the routines in Driscoll's package fail to converge for $L_o^* > 150$ and $\ell^* = \ell/\sqrt{\beta} = 1$. We think that this is due in part to the **crowding phenomenon** known in numerical Schwarz-Christoffel mapping (see [27]). It happens that when the target domain is highly elongated in one direction some prevertices result spaced exponentially close becoming indistinguishable even in double precision. Furthermore, the extremely acute angles of the target polygonal region $S_4$ may also introduce significant secondary crowding effects [27].

A possible solution to this difficulty consists in decomposing the original region (in Figure 3.27(A)) into parts which can be solved successfully by Driscoll's package. Then the resulting prevertices of each section can be used as predictions for the computation of the Schwarz-Christoffel map onto the whole domain.

In Figure 3.28(A) we visualize the coefficient $M(x, \beta = 0.01)$ and the orography $h(x)$ for the parameters indicated above. They are plotted on the spatial coordinate $x$. For this we know that the variables $\xi$ and $x$ are related by equation (3.16) where the coordinate function $\phi$ is evaluated by using Driscoll's routine **eval** [18].

Notice that function $M(x)$ is smooth even at the corners of the orography. In Nachbin [45] is pointed out that $M(x,\beta)$ tends to the original orography as $\beta \to 0$. Here we give a numerical evidence of this fact. Furthermore little details of the orography are not perceived by the free surface coefficient. For instance, in Figure 3.28(B) we detail the interval [0.6,1] where two mountains and one valley seem to be averaged in coefficient $M(x)$. Moreover the overall slope of $M(x)$ is found to be smaller than that of the orography $h(x)$.

Next we validate the pulse-shaping theory of Section 2 by forcing system (2.1) with the coefficient $M(x,\beta = 0.01)$ computed here. In evaluating estimate (2.60) the derivative $M_\xi$ is approximated by

$$M_\xi(\xi,\beta) \approx \frac{M(\xi+\Delta\xi,\beta) - M(\xi,\beta)}{\Delta\xi},$$

where $\Delta\xi = 10^{-3}$.

We first consider the nonlinear hyperbolic system

$$\begin{aligned} M(\xi,\beta)\eta_t + \left(\left(1 + \frac{\alpha\eta}{M(\xi,\beta)}\right)u\right)_\xi &= 0, \\ u_t + \eta_\xi + \frac{\alpha}{2}\left(\frac{u^2}{M(\xi,\beta)^2}\right)_\xi &= 0, \end{aligned} \tag{3.18}$$

which arises after neglecting the dispersive $O(\beta)$ term in system (2.1). We remark that in contrast to other shallow-water models (corresponding to the limit $\beta \to 0$), the variable coefficients in system (3.18) are smooth (even at the orography's corners or discontinuities) due to the scale $\sqrt{\beta} > 0$ appearing inside function $M$ (see equation (3.17)).

In system (3.18) fix $\alpha = 0.001$ and $\sqrt{\beta} = 0.1$ for the smoothing effect. The initial disturbance is a Gaussian-shaped pulse of effective support one, shown in Figure 3.29(a). The numerical parameters are $J = 4500$, $N = 15000$, $\Delta t = 0.0047$ and $\Delta\xi = 0.0078$ and the computational domain is [-5,30]. With these settings the time of computation results in roughly 30 minutes.

In Figure 3.29(b) we display the numerical solution (in solid line) together with the ODA approximation (2.62) for $X = 20$ (in dotted line) corresponding to the medium's station $\xi = 20$ (equivalently 20 pulse's widths). The attenuation due to the multiple scattering process is clearly noted in the pulse's crest (about 1.7).

Observe that the theory reproduces very well the numerical solution for all times. This is due to fact that the whole medium's information was used in approximation (2.62) by taking the parameter $X = 20$ larger than the total length of the bottom's irregular section $L_o = 15$.

In the second experiment we consider the nonlinear Boussinesq system (2.1) with $\alpha = 0.001$ and $\beta = 0.01$. The medium and numerical parameters are left the same as before.

Again in Figure 3.30(b) we compare numerical solution and theory (approximation (2.60)) where the length of the invariant imbedding slab is taken to be $X = 20$. The traces are in good agreement within the interval $[-\infty, 8]$. In contrast to the hyperbolic case, the theory captures only a small part of the forward scattering radiation even though the same parameter $X = 20$ was used. The reason is approximation $a_\beta \approx a_0$ (see equation (2.61)) introduced in (2.60) that, as pointed out in Section 3.3, is less accurate for a large value of the dispersion parameter $\beta$.

The attenuation on the pure dispersive pulse shown in Figure 3.30(a) (solid line) is more notorious over the subinterval [2,8] whereas at the pulse's peak $\tau = 0.5$ it is almost unnoticeable. This is also due to the amplitude of the free surface coefficient fluctuations which is about 0.3, smaller than in the experiments of Section 3.3 where it was synthetized with amplitude $\delta = 0.5$. Therefore in the current experiment the propagation distance should be larger so that the coherent wave front can be substancially filtered by the medium. Beyond $\tau > 6$ we find the incoherent part of the signal which is quickly filtered by the orography's fluctuations.

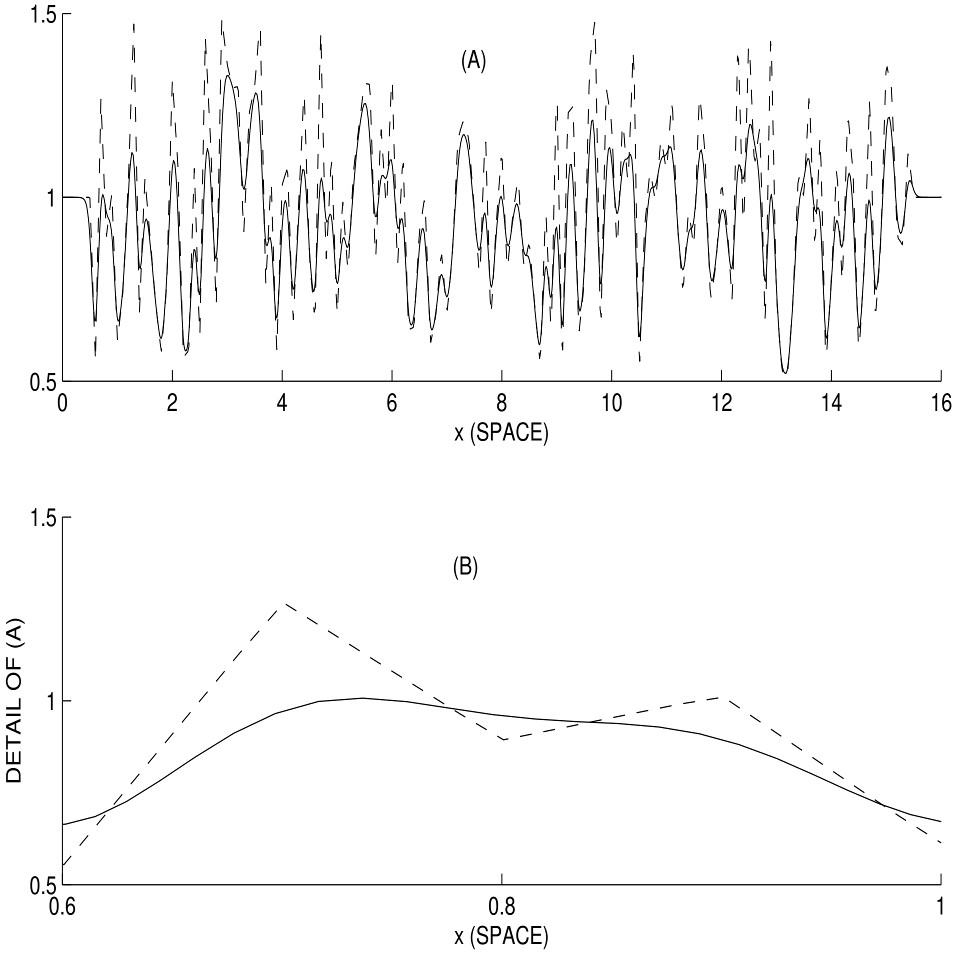


Figure 3.28: Comparison between the physical disordered orography $h(x)$ and the metric coefficient $M(x, \beta = 0.01)$. The former is graphed in dashed line and the latter appears in solid line.

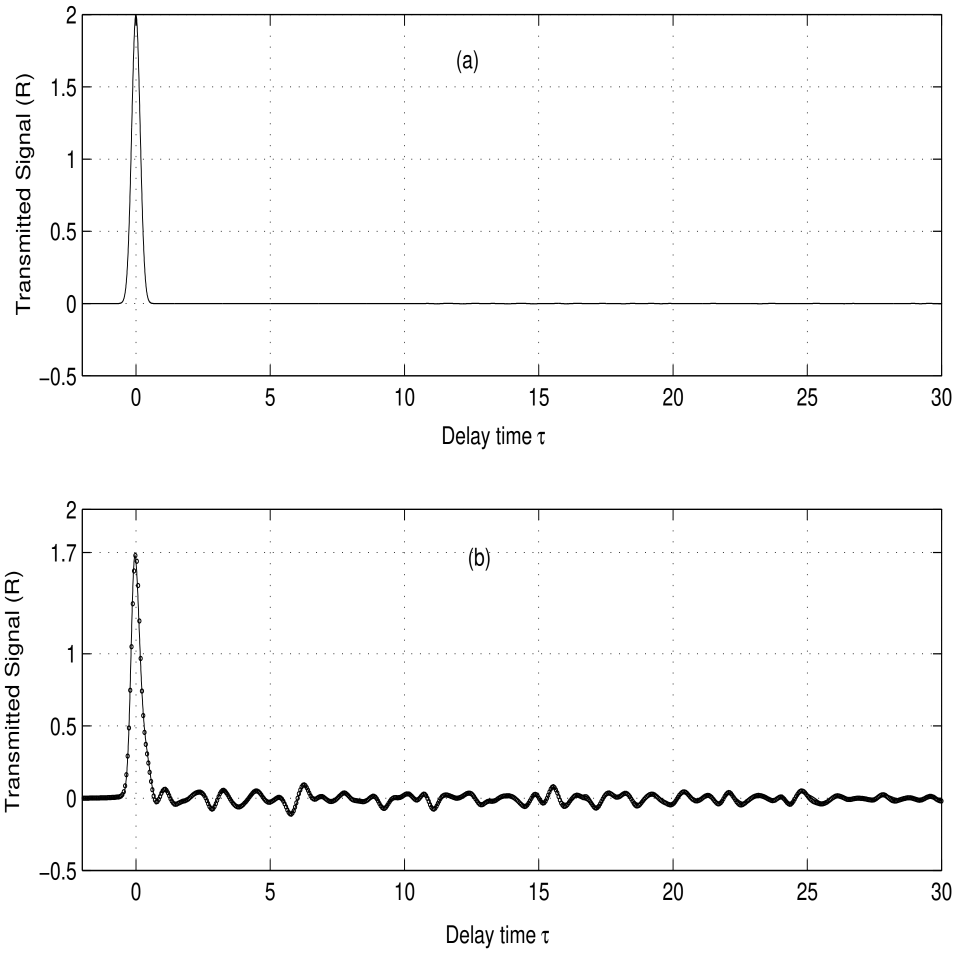


Figure 3.29: (a) Initial disturbance $R(0,\tau) = 2e^{-\tau^2/0.05}$. (b) Gaussian pulse propagating over a non-synthetic disordered rapidly-varying orography. Solid line : Numerical solution at $\xi = 20$ (20 pulse widths). Dotted line : O'Doherty-Anstey approximation (2.62) for $X = 20$. In all experiments $\alpha = 0.001$ and $\beta = 0$.

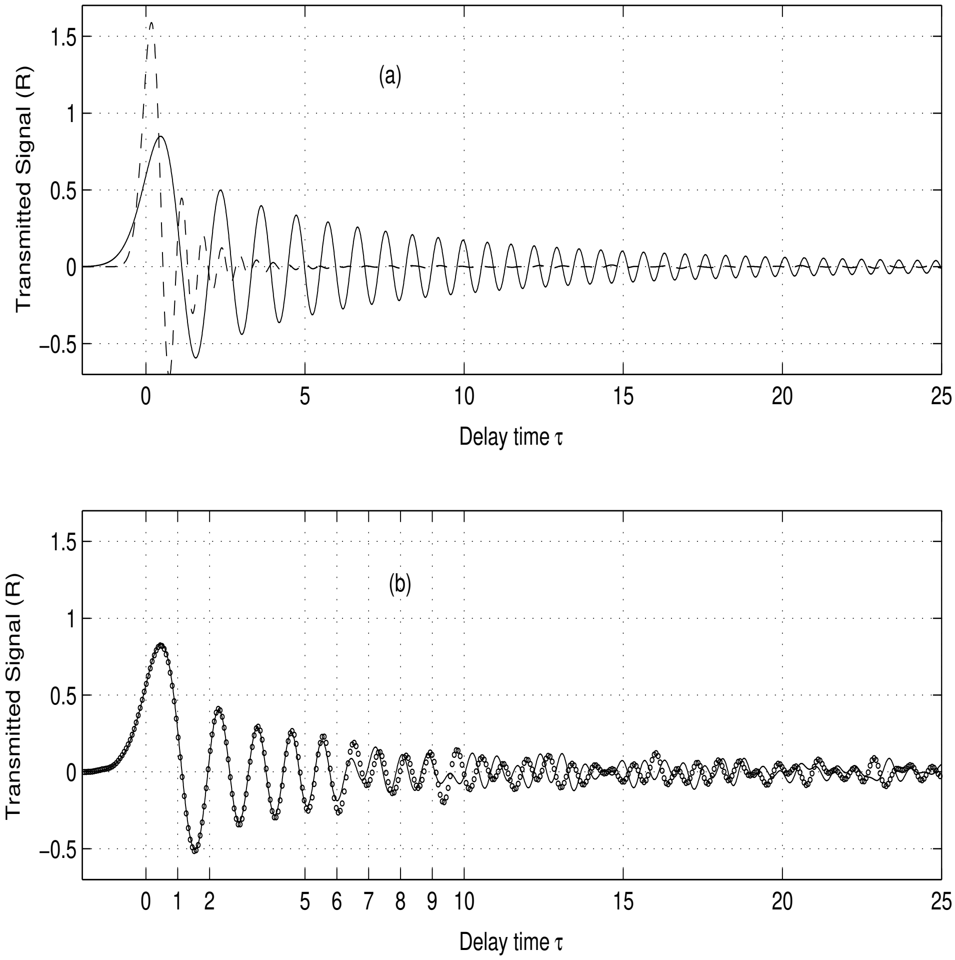


Figure 3.30: (a) Dashed line : Initial disturbance. Solid line : Solution for $M \equiv 1$ (flat bottom) (b) Gaussian pulse propagating over a nonsynthetic disordered rapidly-varying orography. Solid line : Numerical solution at $\xi = 20$ (20 pulse widths). Dotted line : Generalized O'Doherty-Anstey approximation (2.60) for $X = 20$. In all experiments $\alpha = 0.001$ and $\beta = 0.01$.

## 3.7 Conclusions

We have conducted a large number of numerical experiments in order to show the accuracy and robustness of the generalized O'Doherty-Anstey approximation for dispersive waves derived in Chapter 2. The numerical simulations were performed in the nonlinear Boussinesq system (3.1) by using a high-order finite difference scheme proposed by Wei and Kirby [56].

In the hyperbolic regime ($\beta = 0$) the level of nonlinearity (controlled by parameter $\alpha$) was progressively increased. In all cases, the agreement between theory and simulations was observed up to $\alpha = 0.003$. We find that the pulse-shaping formula reproduces with high accuracy not only the deterministic coherent part of the signal (constituted by part of the initial wave energy) but also a segment of the unstructured forward scattering radiation constituted by multiple scattered energy being filtered back by the orography. For an even larger value of nonlinearity $\alpha = 0.005$, nonlinear effects dominate and a shock arises in the wave front and the linear theory is no longer applicable.

We pushed the linear theory beyond its regime of application for exploring the important case of weak solitary waves (up to $\alpha = \beta = 0.01$). In all experiments the theory was found to be in perfect agreement with the corresponding weakly-nonlinear numerical simulation. Thus we tested the extent of application of the linear theory.

Our results also indicate that the orography destroys the dispersive oscillatory coda, being the Fourier modes of smallest localization length (equivalently highest frequency) who are first filtered by the fluctuations of the depth.

From the foregoing results we conclude that the new dispersive pulse-shaping theory provides a valuable tool for understanding the interplay between weak dispersion and orography in waves with small amplitude.

The generalized O'Doherty-Anstey approximation is very robust. This is due to the stabilization property which guarantees that the shape of the coherent front varies very little when a different orography's realization is considered. In contrast, the random fluctuations following the deterministic head pulse do not stabilize and depend highly upon the particular realization of the orography. This phenomenon was verified numerically both for Gaussian pulses and for weak solitary waves.

# Chapter 4

# Time reversal and refocusing

When a pulse scatters through a long highly disordered medium its shape is strongly modified and multiple reflections arise.

An amazing fact is that the reflected signal produced by this wave-orography interaction can be used to **refocus** (recover) the initial disturbance. This property of a highly disordered medium was studied by Fink [20] in the context of linear acoustic waves.

In this section, we wish to explore the refocusing for weakly-nonlinear, weakly-dispersive waves modeled by the terrain-following Boussinesq system (2.1) by using the **time reversal method** which was successfully applied to hyperbolic problems in random media by Clouet and Fouque [17]. The scaling and orography setups are as indicated in Chapter 2. The orography's fluctuations cover the interval [5,45] and its amplitude is $\delta = 0.5$. The numerical parameters are $J = 12000$, $N = 14000$, $\Delta\xi = 0.0075$ and $\Delta t = 0.0036$ and the computational domain is [-40,50]. It is sufficiently large to enable us to record a long part of the reflected signal emerging from the medium. In this case, the time of computation is estimated to be about 40 minutes.

The procedure employed to produce the pulse refocusing for the wave elevation field is explained in Figure 4.1. We set $\alpha = 0.001$ and $\beta = 0.002$. A Gaussian disturbance $\eta(\xi, 0) = u(\xi, 0) = h(\xi)$ (see (A)) is located at the leftside of the origin, say $\xi_o = -5$, and allowed to propagate to the right.

At time $t = t_1$ ($t_1 = 50$), we record the wave elevation $\eta(\xi, t_1)$ and the velocity $u(\xi, t_1)$ and cut any part of them to the leftside of the origin. A possible choice is the window within dashed lines indicated in (B). Here we use $G = 1_{[\ell_0,0]}$ (the indicator function of the interval $[\ell_0, 0]$) as the cutoff function. In this experiment we set $\ell_0 = -40$.

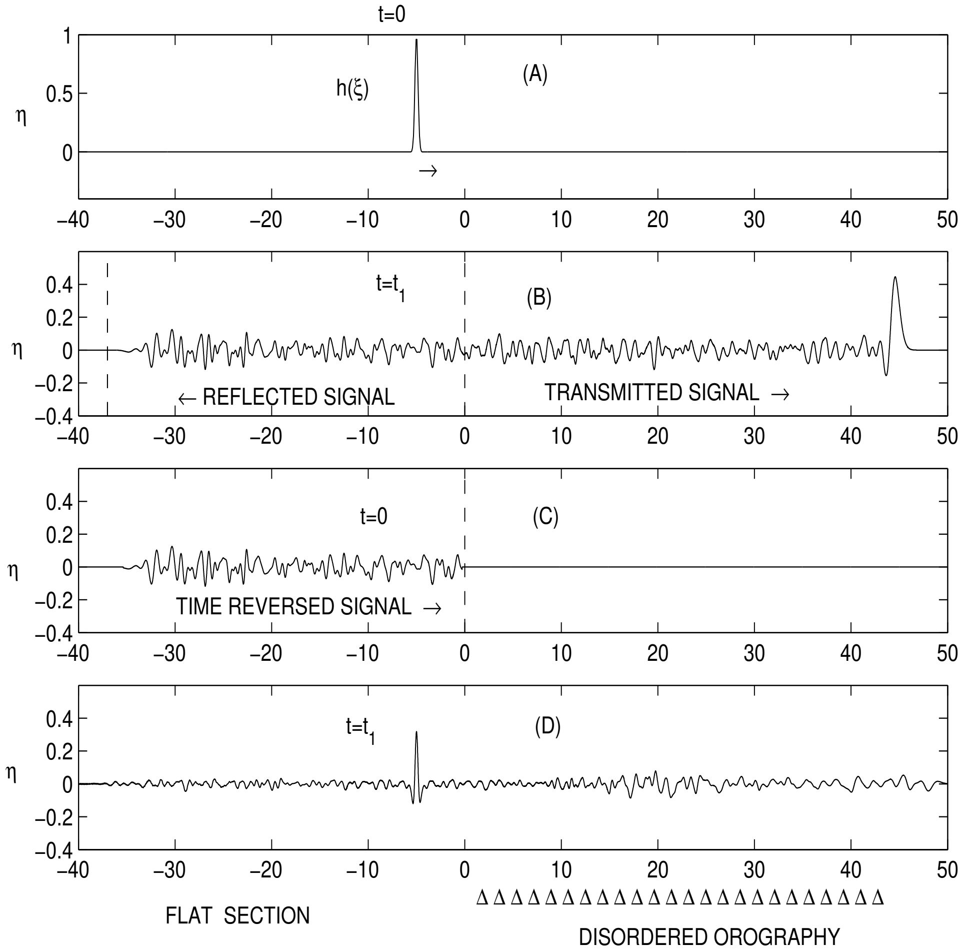


Figure 4.1: The time reversal method. In (A) we visualize the initial disturbance. In (B) we show the signal after travelling a distance of 50 units of channel ($t = t_1$). In (C) we indicate with dashed lines the signal's section considered for the time-reversal method. This "new" signal is sent back to the medium. In (D) the refocused pulse arises exactly at time $t = t_1$. Model parameters : $\alpha = 0.001$, $\beta = 0.002$.

The time-reversal method consists in changing the sign of the velocity field so that the "new" signal $\eta_o(\xi) = \eta(\xi, t_1)G(\xi)$, $u_o(\xi) = -u(\xi, t_1)G(\xi)$ corresponds to a rightgoing wave which is sent back to the **same medium** (see (C)) in its reversed time of arrival. In this way, last information in, first information out. In (D) we see a "clean" refocused pulse similar to $h(\xi)$ arising at its original location $\xi_o = -5$ exactly at time $t_1 = 50$. We remark that if at this step the medium is replaced by a different realization of the orography the refocusing **never** takes place.

In Figure 4.2 we superimpose the refocused pulse with the original Gaussian-shaped disturbance $h(\xi)$. Observe that the height of the former is about 30% of the latter. Moreover two mild undulations appears on both sides of the refocused pulse. These facts are due to the cutoff function $G$ introduced in the time-reversal method. This is demonstrated through probabilistic techniques in [17] for a one dimensional linear hyperbolic model analogous to system (2.20) with $\beta = 0$. In addition, their result implies in that the shape of the refocused pulse approximates $h(\xi)$ when the cutoff time $t_1$ increases (the **time refocusing property**). This corresponds to time reversing a longer segment of the reflected signal. Further hyperbolic experiments have been conducted in Fouque and Nachbin [22]. In the present work, dispersive refocusing has been done for the first time.

We now increase the dispersion parameter to $\beta = 0.01$. Other parameters are the same as in the preceding experiment. The resulting refocused pulse is plotted in Figure 4.3 where it is superimposed to the refocused pulse for $\beta = 0.002$. A remarkable fact is that the model's dispersion does not seem to affect the shape of the refocused pulse even at large values of dispersion. For the case that $\beta = 0.01$ in Figure 4.4 we examine the wave elevation at several time stages before the refocusing. A leftpropagating Airy-like pulse is observed in (A). The dispersive oscillation (now) ahead of the wave progressively decreases as long as time approximates to $t = 50$, the exact instant in which refocusing takes place. At this time we observe a relative "clean" pulse (see E) where the dispersive effects seem to have disappeared. Thus the dispersive tail has been compressed. This is a remarkable phenomenon only observable when dispersion is present.

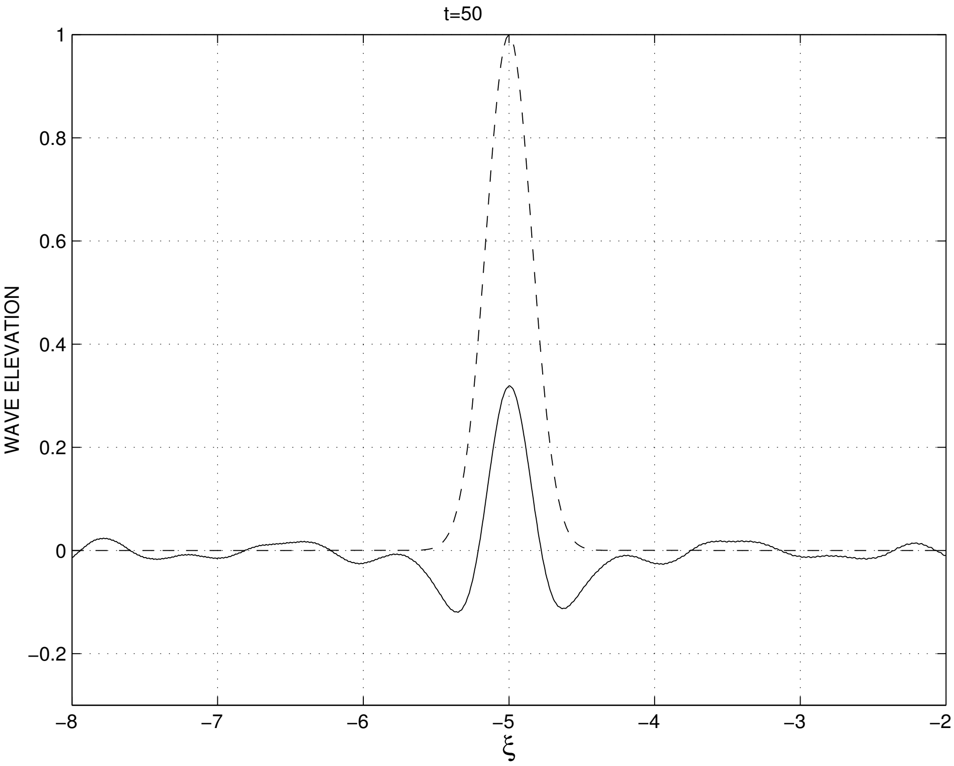


Figure 4.2: In dashed line : initial disturbance $h(\xi)$. In solid line : refocused pulse. Model parameters : $\alpha = 0.001$, $\beta = 0.002$.

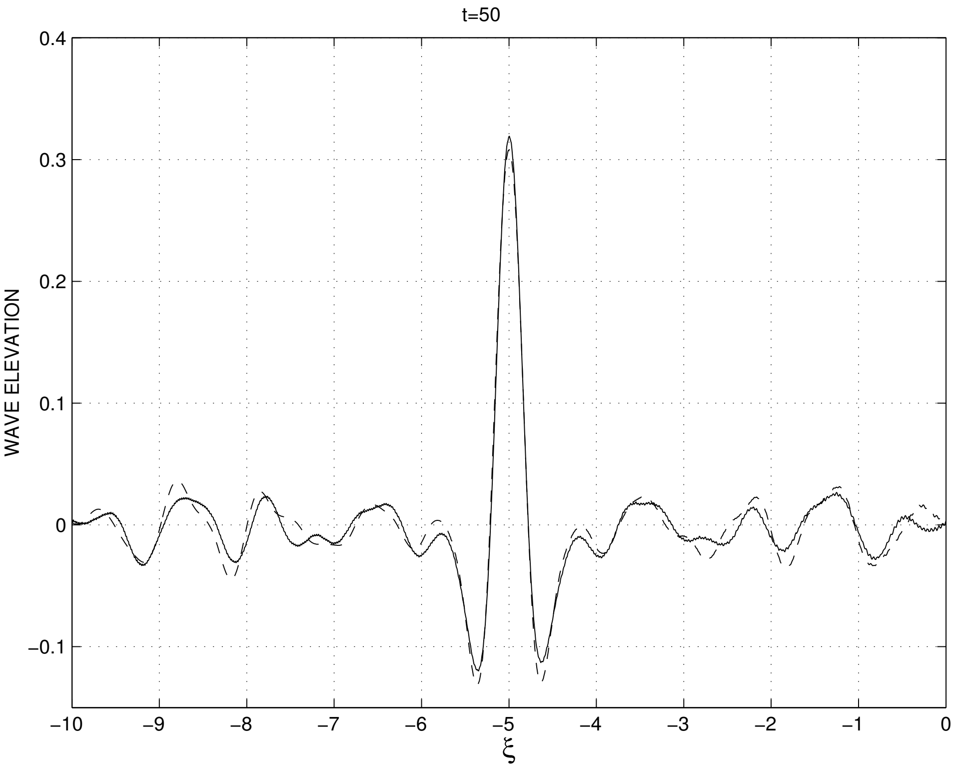


Figure 4.3: Refocusing of a Gaussian pulse for two dispersion levels: $\beta = 0.002$ (in solid line) and $\beta = 0.01$ (in dashed line).

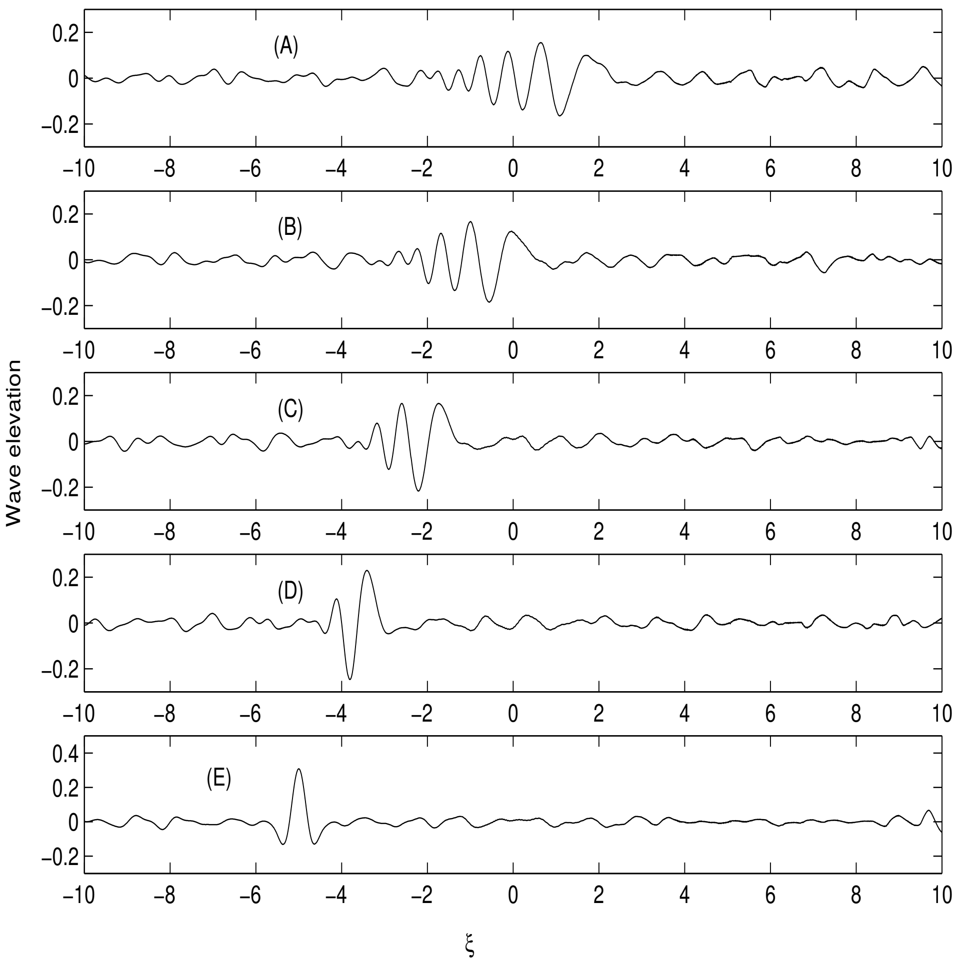


Figure 4.4: Dispersive refocusing mechanism. From top to bottom the plots correspond to the wave elevation at times $t = 43.2, 44.6, 46.4, 48.2, 50$, respectively. Model parameters : $\alpha = 0.001$ and $\beta = 0.01$.

We now examine the refocusing property in solitons. This is an interesting experiment because a weak nonlinearity is introduced ($\alpha = \beta = 0.001$). There is no available nonlinear theory for dispersive refocusing. For nonlinear hyperbolic systems Fouque et al. [21] obtained (stochastic theory) results using this work and [43] as the starting point.

The orography's fluctuations cover the interval [5,95], its amplitude is $\delta = 0.5$ and its correlation length is taken to be $\ell = 0.6$. The numerical parameters are $J = 8500$, $N = 7500$, $\Delta\xi = 0.025$ and $\Delta t = 0.016$ and the computational domain is [-110,100]. The time of computation of each experiment is approximately 10 minutes.

The refocused pulse and the initial soliton are graphed in Figure 4.5. The cutoff time is $t_1 = 120$ for which we recover only 20% approximately of the incoming energy in contrast to the Gaussian in Figure 4.2 for a smaller time ($t_1 = 50$). This is due to the fact that in the Fourier space the frequency band of the soliton (with effective width $\ell_p \approx 6$) is narrower than the Gaussian ( with $\ell_p \approx 1$) used in previous experiments. It requires a larger time so that the energy contained in the low frequency spectrum of the soliton returns in the reflected signal.

## 4.1 The refocusing linear theory

Formula (2.40) derived in Chapter 2 is the primary tool in order to develop a mathematical theory for dispersive wave refocusing. We follow the strategy used in [17] for one-dimensional acoustic waves. Like in the ODA theory the analysis is performed in time to take advantage of the fact that the coefficient $M(\xi)$ in system (2.20) is time independent.

Suppose that the incoming pulse in time is $R(\xi = 0, t) = f(t)$. The reflected signal generated by the interaction of this wave with the orography is received at the interface $\xi = 0$ and recorded over a finite time interval $[0, t_1]$. This signal corresponds to $L(0,t)G_{t_1}(t)$, where $G_{t_1} = 1_{[0,t_1]}$. For simplicity the $t_1$ subscript in $G$ will be omitted. When time reversed it yields the signal $g(t) = L(0, t_1 - t)G(t_1 - t)$.

To obtain an expression for $\hat{g}(\eta)$ we first apply equation (2.40) at the origin $x = 0$ and the Fourier inversion formula to find that

$$L(0,t) = \frac{1}{2\pi}\int e^{i\omega t}\widehat{K}(0,\omega)\hat{f}(\omega)d\omega, \tag{4.1}$$

where $\widehat{K}(0,\omega)$ is the solution at $x = 0$ of the initial value problem (2.41) subject to $\widehat{K}(X,\omega) = 0$. Recall that the parameter $X$ denotes the length of the slab used in the invariant imbedding technique.
Therefore $\hat{g}(\eta)$ can be written as

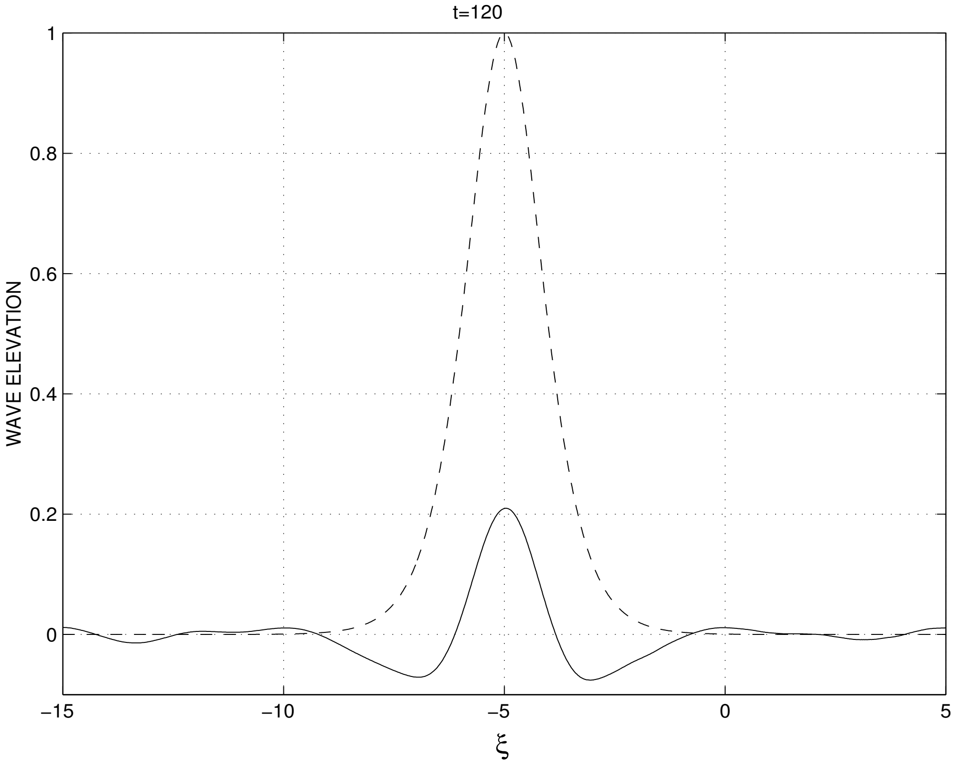


Figure 4.5: In dashed line : initial soliton. In solid line : refocused soliton. The model parameters are $\alpha = \beta = 0.001$.

$$\hat{g}(\eta) = \frac{1}{2\pi} \int e^{-i\eta t} \int e^{i\omega(t_1 - t)} \widehat{K}(0, \omega) \hat{f}(\omega) d\omega \; G(t_1 - t) dt. \tag{4.2}$$

After some changes of variables and applying the symmetry properties $\widehat{K}(0, -\omega) = \overline{\widehat{K}(0, \omega)}$ and $\hat{f}(-\omega) = \overline{\hat{f}(\omega)}$ we arrive at

$$\hat{g}(\eta) = \frac{1}{2\pi} \int e^{-it_1\eta} \overline{\widehat{K}}(0, \omega) \overline{\hat{f}}(\omega) \overline{\hat{G}}(\eta - \omega) d\omega. \tag{4.3}$$

When the signal $g(t)$ is sent back to the **same medium** it generates a new reflected signal $L_{\text{ref}}(0, t)$. By using equations (4.3),(2.40) and the Fourier inversion formula we deduce that

$$L_{\text{ref}}(0,t) = \frac{1}{4\pi^2}\int\int e^{i\eta(t-t_1)}\widehat{K}(0,\eta)\overline{\widehat{K}}(0,\omega)\overline{\hat{f}}(\omega)\overline{\hat{G}}(\eta-\omega)d\omega\, d\eta. \tag{4.4}$$

Furthermore, equation (4.4) can be rewritten in a more compact form. To do this we let $t = t_1 - s$ and introduce the change of variables $h = \eta - \omega$ to yield that

$$L_{\text{ref}}(0,t_1-s) = \frac{1}{2\pi}\int \overline{\hat{f}}(\omega)e^{-i\omega s}\overline{\hat{H}}_{t_1,s}(\omega)d\omega, \tag{4.5}$$

where $H_{t_1,s}(\omega)$ is the Fourier inverse transform with respect to $\omega$ of the function

$$m_{t_1,s}(\omega) = \frac{1}{2\pi}\int e^{ihs}\overline{\widehat{K}}(0,h+\omega)\widehat{K}(0,\omega)\hat{G}(h)dh. \tag{4.6}$$

Therefore by the convolution theorem we arrive at

$$L_{\text{ref}}(0,t_1-s) = (f(\cdot) * \overline{H}_{t_1,s}(\cdot))(s). \tag{4.7}$$

Formula (4.4) (or (4.7)) extends to dispersive waves the result by Clouet and Fouque [17] for one dimensional hyperbolic waves.

Observe that coefficient $\widehat{K}$ appears twice in equation (4.4), one for each time that the signal crosses the medium. If the time-reversal method is repeated a new copy of the reflection coefficient is introduced. This product of kernels $K$ in equation (4.6) is connected with the stochastic characterization of the power spectral density of the reflection process as given in [22], [13].

Kernel $K$ acts as the "medium's memory" because it stores the information required to rebuild the incoming pulse $f$ and indeed the "noise" around it. We point out that this noise is not captured by the probabilistic theory in [17]. The length of the part of medium considered is controlled by parameter $X$ which appears in computing kernel $K$ through the invariant imbedding technique. It must be larger than $t_1/2$ so that the refocused pulse can be recovered by equation (4.4). This is in accordance with intuition because a cutoff time higher $t_1$ implies in that the wave penetrates a deeper distance into the medium.

We will confirm the facts above through numerical simulations. We observe, however, that the computation of the coefficient $\widehat{K}$ directly from the Riccati equation (2.41), necessary in evaluating equation (4.4), is expensive. For this reason, as done in the ODA theory, we adopt the linear approximation

$$\widehat{K}(x_o,\omega) \approx -\int_{x_o}^{x_o+X} e^{2i\omega\int_{x'}^{x_o}\Gamma(s,\omega)\,ds}\bar{\zeta}(x',\omega)dx'. \tag{4.8}$$

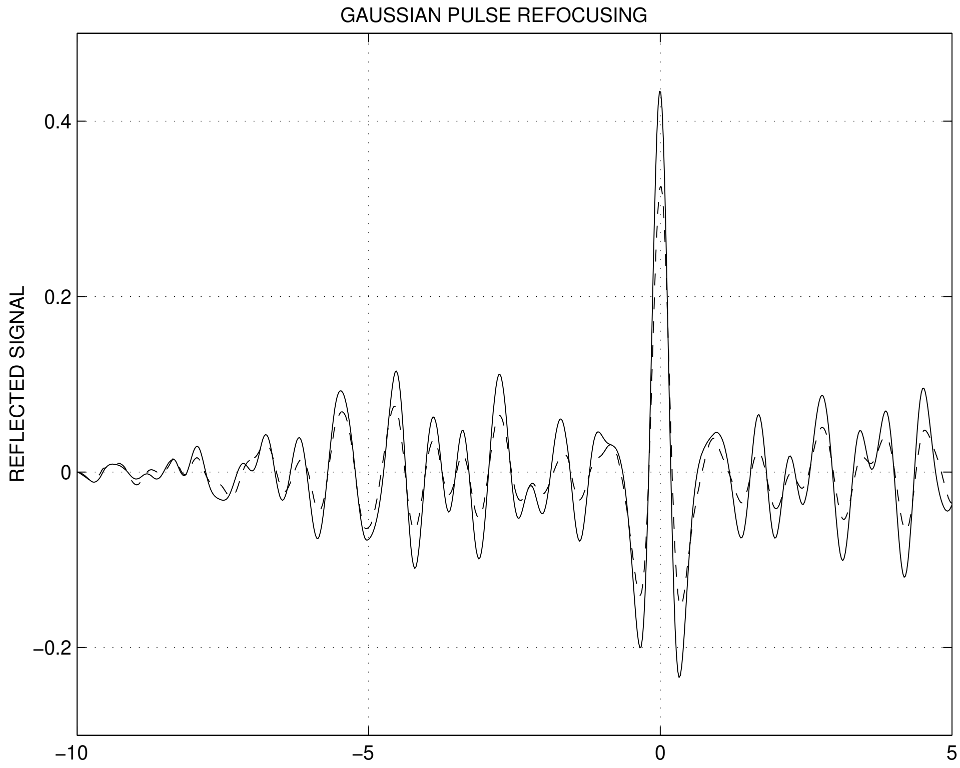


Figure 4.6: Reflected signal $L_{\text{ref}}$. Dashed line : numerical solution. Solid line : refocusing formula (4.4) for $X = 7.5$. Model parameters : $\alpha = 0.001$ and $\beta = 0$. The pulses have been centered at the origin for comparison.

First consider a Gaussian disturbance of the form $R(0,t) = f(t) = 2e^{-(t-5)^2/0.05}$ and $\beta = 0$. The nonlinearity is taken to be small $\alpha = 0.001$. The fluctuations of the orography are located within the interval [5,45] and its amplitude is taken to be $\delta = 0.5$. Also set $\ell = 0.1$. In Figure 4.6 we see that the theoretical formula (4.4) with $X = 7.5$ and the numerical solution agree reasonably. Notice that the two undulations on both sides of the refocused pulse are also reproduced by the theory. This can be explained by the fact that the Fourier transform of the cutoff function $\hat{G}$ (appearing in equation (4.4)) is a sinc function.

A little discrepancy in amplitude is found between theory and numerics. We believe that this is due to the **linear** approximation of the reflection coefficient $\widehat{K}$ introduced in equation (4.8).

Next, as shown in Figure 4.7 we consider the solitary wave defined by equation (3.14) with $\alpha = \beta = 0.001$. The fluctuations cover the interval [5,95], its amplitude is $\delta = 0.5$ and $\ell = 0.6$. The theoretical formula, with $X = 100$, is superimposed to the numerical solution

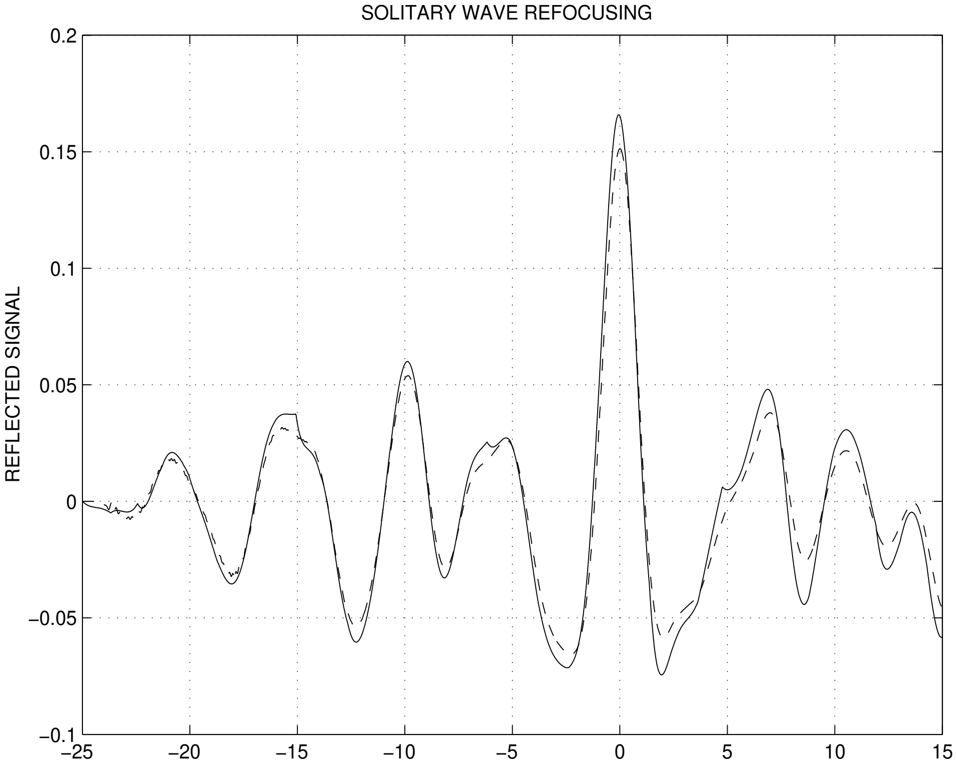


Figure 4.7: Reflected signal $L_{\mathrm{ref}}$. Dashed line : numerical solution. Solid line: refocusing formula (4.4) for $X = 100$. The model parameters are $\alpha = \beta = 0.001$. Both pulses are centered at the origin for comparison.

and again found to be in good agreement. The cutoff time in this experiment is $t_1 = 30$.

As mentioned above, Fouque et al. [21] consider only nonlinear hyperbolic waves. This work is the first to consider the refocusing of solitary waves and to provide an approximate expression for the refocused soliton shape. We also recall that, being deterministic, this theory is able to also capture the incoherent part about the refocused wave.

## 4.2 Refocused pulse stabilization

For one dimensional hyperbolic waves Clouet and Fouque [17] show that the shape of the refocused pulse does not depend on the particular medium's realization considered. They call it **refocusing self-averaging property**.

Here we explore it in the context of dispersive waves. We consider a Gaussian-shaped

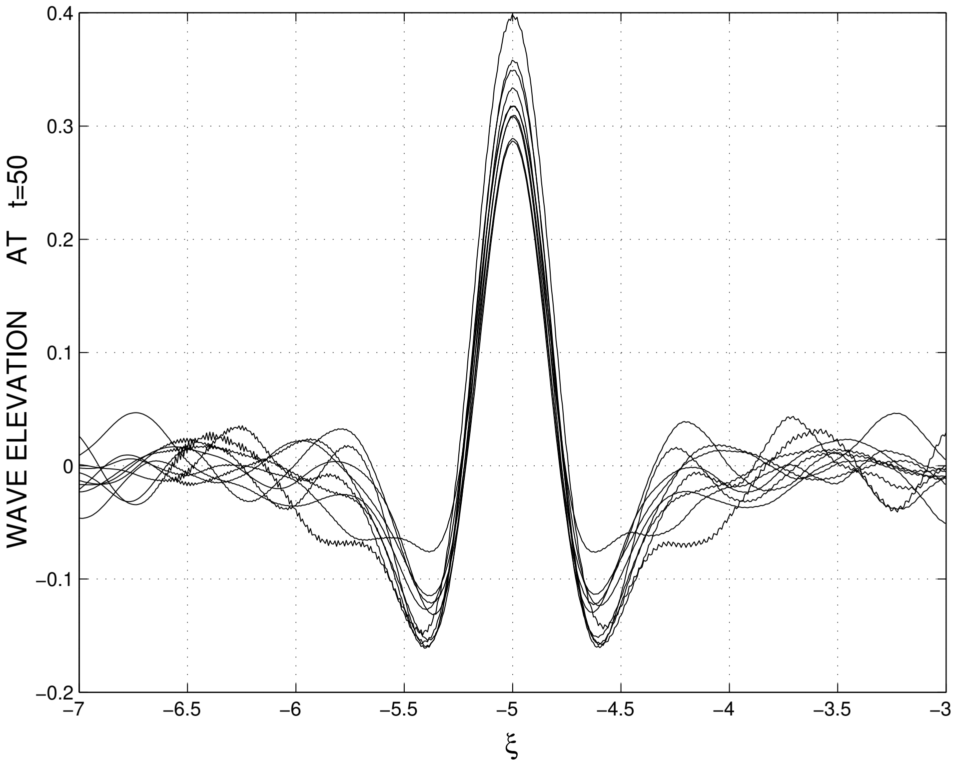


Figure 4.8: Refocusing stabilization of a Gaussian pulse over ten different synthetic orography realizations for $\alpha = 0.001$ and $\beta = 0.01$.

disturbance of effective unit width located at position $\xi_o = -5$. The time-reversal method is carried out separately in each of the ten different orography realizations which are constructed as indicated in Section 3.5. In all of them, the cutoff time is $t_1 = 50$. The fluctuations cover the interval [5,45], their amplitude is $\delta = 0.5$ and the orography's correlation length is $\ell = 0.1$.

In Figure 4.8, we superimpose the traces of the refocused pulses and find that their shapes stabilize approximately on the time interval [-5.5,-4.5]. There we find that the maximum difference is about 0.1 at the pulses' crest. Notice that about 30% to 40% of the total energy is refocused by the sequence of orographies considered here.

We repeat the preceding experiment in the case of a solitary wave. Its initial position is taken to be $\xi_o = -5$. The nonlinearity and dispersion parameters are set to $\alpha = \beta = 0.001$. Now the fluctuations of the orography cover the interval [5,95], their amplitude is $\delta = 0.5$ and its correlation length is $\ell = 0.6$. The cutoff time for the time-reversal method is $t_1 = 120$ in all cases. The results are presented in Figure 4.9. The stabilization of the shape of the

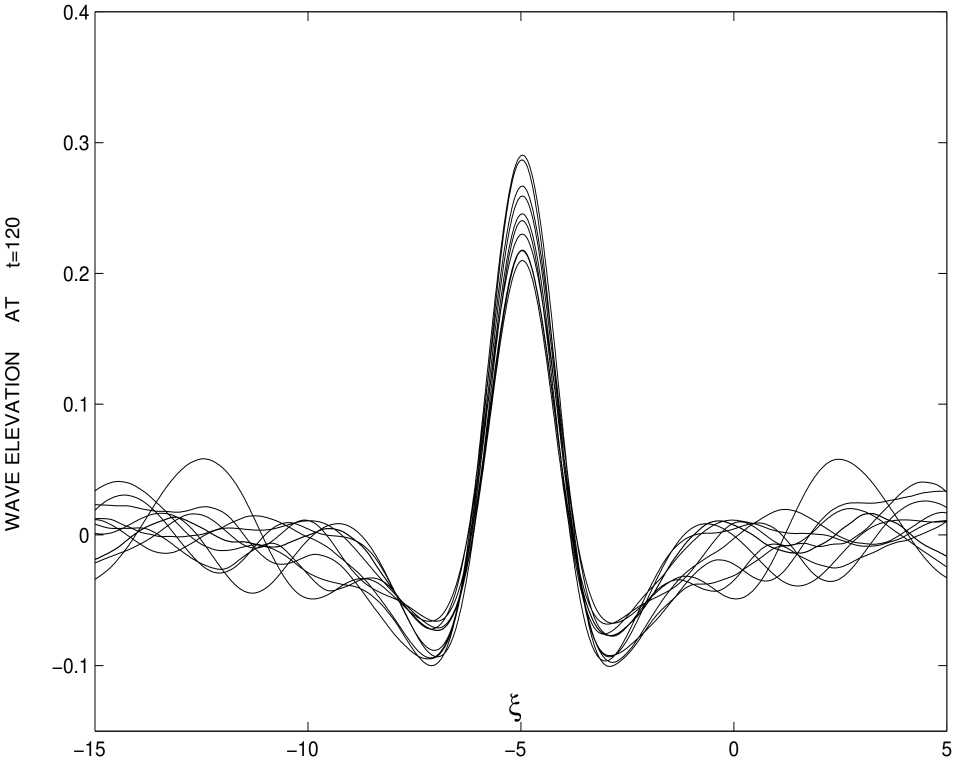


Figure 4.9: Refocusing stabilization for a soliton over ten different synthetic orography realizations. The model parameters are $\alpha = \beta = 0.001$.

refocused pulse takes place within the interval [-6,-2] where the maximum difference between the traces is about 0.1. Furthermore about 20% to 30% of the incoming soliton is refocused in the ten experiments.

## 4.3 Conclusions

In this chapter we have explored the property of refocusing of a dispersive water wave sent over a highly disordered orography. A part of the reflected signal produced by the wave-orography interaction is time reversed and resent to the medium. The result of this process is that the initial pulse is refocused (recovered) at its original source. The quality of the resulting refocused pulse depends on the extent of the reflected signal considered in the time-reversal technique.

In the linear case we derived a deterministic formula which gives a reasonable prediction for the refocused pulse, even reproducing part of the noise which appears around it. With numerical simulations we showed that the theory is applicable for weak solitons with $\alpha = \beta = 0.001$.

Furthermore, for Gaussian disturbances our numerical experiments indicated that the shape of the refocused pulse does not appear to be affected by the value of the dispersion parameter. Thus the dispersive oscillatory coda (observed at intermediate time stages) is compressed and disappears completely at the exact moment in that the refocusing takes place.

Finally, we find that the shape of the refocused pulse does not depend on the particular realization of the orography. In other words, it depends only on the statistical parameters of the medium. This is a strong evidence of the self-averaging property in the dispersive case, already observed in acoustic waves in [17], [20] and [52].

# Chapter 5

# Numerical advantages of Nachbin's model

We show the consistency of the terrain-following Boussinesq system (2.1) as compared with Peregrine's model [51] when they are viewed in the appropriate regime. This will be accomplished through numerical simulations on both models.

Peregrine's model [51] in dimensionless variables reads

$$\begin{aligned} &\eta_t + [(h+\alpha\eta)]_x = 0, \\ &u_t + \eta_x + \alpha u u_x + \beta\left(\frac{h^2}{6}u_{xxt} - \frac{h}{2}\partial_x^2(hu_t)\right) = 0, \end{aligned} \tag{5.1}$$

where $u = u(x,t)$ and $\eta(x,t)$ denote the averaged velocity and the wave elevation, respectively, and $h(x) = 1 + \delta n(x/\ell)$ is a function describing the channel's depth. Parameters $\ell$, $\delta$ and function $n(x)$ are as in Section 3.6 and $\alpha$ and $\beta$ are defined as done for model (2.1) (see Section 2).

Mei [40] (pag. 59) points out that model (5.1) is valid for small amplitude, weakly-dispersive wave propagation provided that the **mild condition**

$$m = O\left(\frac{h'(x)}{kh}\right) << 1, \tag{5.2}$$

is satisfied. Here, parameter $k$ represents the typical wavenumber. Implicity, it is also assumed that the derivative of the depth function is well-defined. In dimensionless variables, condition (5.2) can be expressed as

$$m = O\left(\frac{\delta n'(x/\ell)}{2\pi\ell\sqrt{\beta}}\right) << 1. \tag{5.3}$$

Other Boussinesq models in the literature, such as those by Nwogu [48] and Madsen et al. [37], also rely its validity on condition (5.3).

We remark that, in this work, condition (5.3) is not satisfied because the depth's correlation length $\ell$ is small for a rapidly-varying orography. Furthermore, we are considering general non-differentiable orographies. For instance, the orography considered in Section 3.6 is only piecewise differentiable and, moreover, $m \approx 8$.

Hence, the terrain-following system (2.1) extends the regime of validity of system (5.1) being even applicable for non-differentiable arbitrary orographies, which turns the mild condition unnecessary [45]. Its unique restriction is that the dispersion and nonlinearity parameters $\beta$, $\alpha$ be small which is common to all Boussinesq systems. As expected, models (5.1) and (2.1) coincide when condition (5.3) is fulfilled. To confirm this, we implement Wei and Kirby's scheme for system (5.1) for which we rewrite it as

$$\begin{aligned} \eta_t &= \tilde{E}(\eta, u), \\ \tilde{V}_t &= \tilde{F}(\eta, u), \end{aligned} \tag{5.4}$$

where

$$\begin{aligned} \tilde{E}(\eta, u) &= -[(h + \alpha\eta)u]_x, \\ \tilde{F}(\eta, u) &= -\alpha u u_x - \eta_x \end{aligned}$$

and

$$\tilde{V} = u + \beta\frac{h^2}{6}u_{xx} - \beta\frac{h}{2}(hu)_{xx}. \tag{5.5}$$

Again, in the change of variable $\tilde{V} \to u$, only one tridiagonal linear system must be solved. Nevertheless, the system's matrix now depends on the orography through the functions $h(x)$ and $h'(x)$. Recall that in the case of model (2.1) the corresponding system's matrix is constant (c. f. equation (3.10)). This is a direct consequence of the fact that the coefficient of the dispersive term $u_{\xi\xi t}$ in model (2.1) is constant in opposition to system (5.1).

System (5.4) is solved by the predictor-corrector scheme (3.6)- (3.11). In addition, first order derivatives of $\eta$ and $u$ are approximated as done in Section (3). Equation (5.5) is

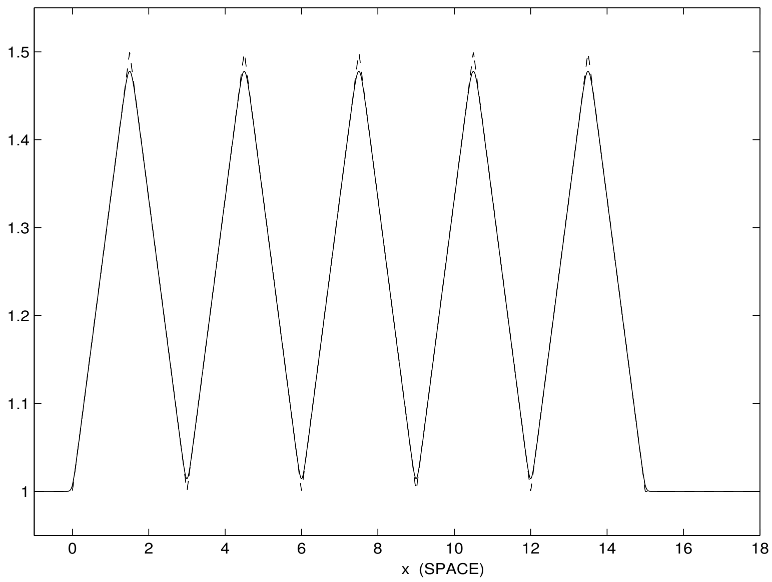


Figure 5.1: Free surface coefficient $M(x, \beta = 0.01)$ (in solid line) superimposed to a periodic piecewise linear orography (in dashed line).

discretized by using centered second-order approximations. At the orography's corners we use the leftside derivative of function $h(x)$.

We construct the periodic piecewise linear orography displayed in Figure 5.1. It consists of five equal triangles with base of length 3 and height 0.5. In this way, the inhomogeneities cover the interval [0,15], the amplitude of the fluctuations is $\delta = 0.5$ and the correlation length is $\ell = 1.5$. With this setup note that we have a slowly-varying bottom with slope 1:3 and $m \approx 0.5$.

The corresponding orography-dependent coefficient $M(x, \beta)$ is computed by using Driscoll's package [18] as explained in Section 3.6. Note that in this case the largest difference between them is at the mountain's peaks where $M(x)$ is smooth.

We compute the numerical solution for systems (2.1) and (5.1) forced by functions $M(x, \beta)$ and $h(x)$, respectively. In this experiment the level of dispersion and nonlinearity are taken to be $\alpha = \beta = 0.01$. The numerical parameters for both experiments are $J = 2000$, $N = 1500$, $\Delta\xi = 0.02$, $\Delta t = 0.01$ and the computational domain is [-20,20]. The time of computation is estimated in about one minute. The initial disturbance is a Gaussian of effective support one located at position $x = 0$. The ratio inhomogeneities/wavelength is set to roughly 1.5.

The numerical solutions for both models calculated at time $t = 15$ are visualized in Figure 5.2(A) each one on its corresponding independent spatial variable.

To establish a comparison between these solutions we replot them in Figure 5.2(B) but now on the physical spatial variable $x$. As in Section 3.6 the change of variable $\xi \to x$ was performed by using the routine **eval** in Driscoll's package. Note that the traces are in perfect agreement showing the consistency between the two models in the slow-varying depth regime. Nevertheless, small spurious oscillations are observed in the numerical solution of system (5.1). This can be seen with solid line in the detail presented in (C). We think that this is due to the acute corners where function $h(x)$ is non-differentiable and also the fact that the variable coefficient $h(x)$ appears in the dispersive term of the system. It has an effect on the solution of the linear system solved in changing from the intermediate variable $\tilde{V}$ to the fluid velocity $u$. This is an interesting numerical issue that deserves further investigation.

When the mesh sizes are increased substantially up to $J = 20000$, $N = 15000$ the spurious oscillations do not disappear completely. We also obtained similar results when the depth's slope was decreased up to 1:10.

In contrast, the simulation for model (2.1) in Figure 5.2(B) appears to be very smooth. In this experiment we set $J = 2000$ and $N = 1500$. A "clean" numerical solution is obtained with a low computational cost. We point out this fact as an important numerical advantage of system (2.1).

## 5.1 Conclusions

In a slowly-varying depth (i.e. when the mild condition (5.3) satisfies) we have showed numerically the consistency of the terrain-following Boussinesq system (3.1) (adopted in this work) with Peregrine's model [51]. This was accomplished by using Wei and Kirby's numerical scheme implemented in both models. The numerical solutions agree when superimposed in the same coordinate system. However, we observe that even for larger mesh sizes the simulation corresponding to Peregrine's model exhibits small spurious oscillations in contrast to model (3.1) which numerical solution is smooth with a low cost. This gives evidence of a potential numerical advantage of the Boussinesq system (3.1) which we intend to explore in more detail in a further work. At this moment we think that this fact is due to the matrix of linear system involved in the Boussinesq solver is not constant. The reason is that the dispersive terms of Peregrine's model [51] have orography-dependent variable coefficients. On the other hand, remark that the dispersive coefficient in system (3.1) is constant.

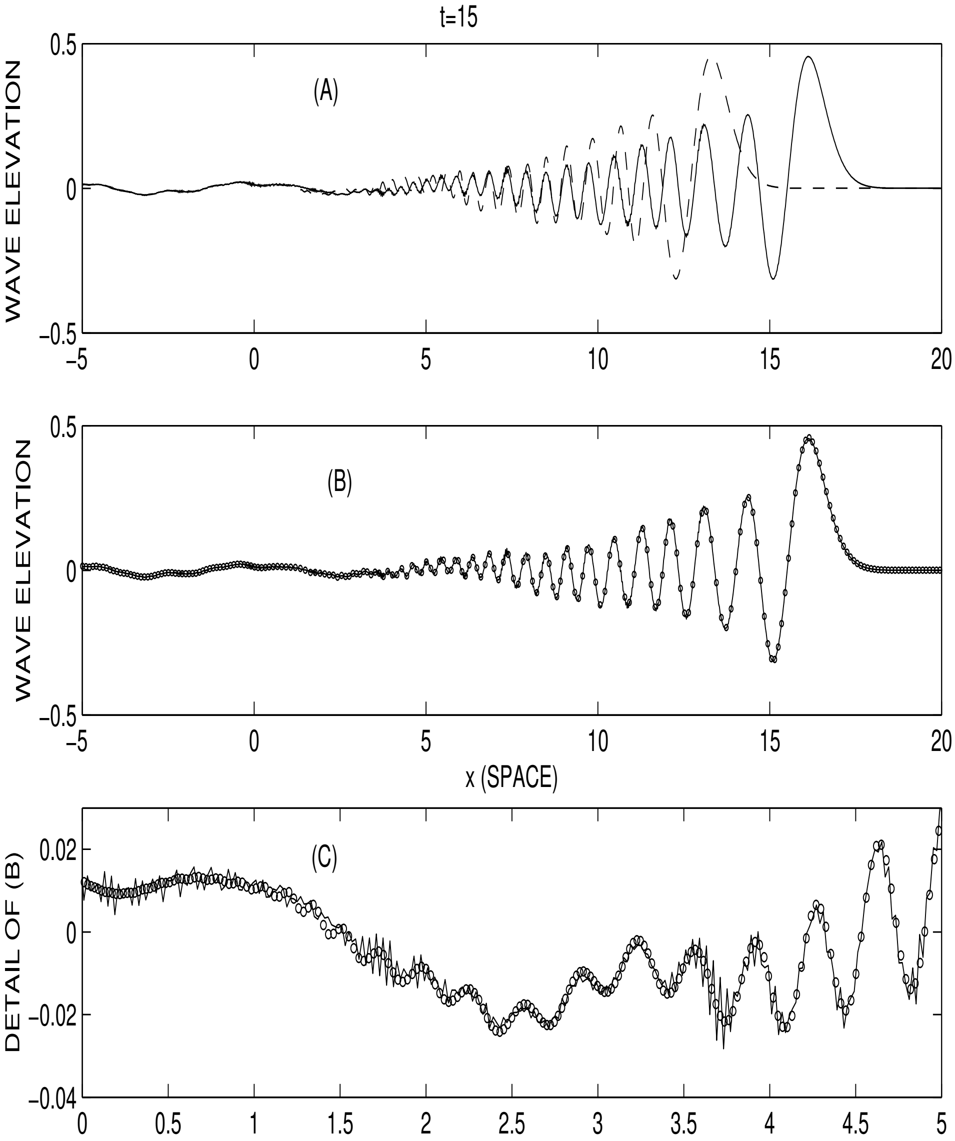


Figure 5.2: **(A)** Dashed line : Nachbin's model. Solid line : Peregrine's model. **(B)** Dotted line : Nachbin's model. Solid line : Peregrine's model. Now they are both visualized in the physical spatial variable $x$. **(C)** Detail of (B). The oscillations in solid line correspond to Peregrine's model. In all experiments we set $\alpha = 0.01, \quad \beta = 0.01$. The topography's correlation length is $\ell = 1.5$ and the amplitude of fluctuations is $\delta = 0.5$.

# Chapter 6

# Final conclusions

In this work we studied the scattering of weakly dispersive water waves with small amplitude over highly disordered depths in the shallow-water regime modelled by the terrain-following Boussinesq system (2.1).

Several wave phenomena were investigated. First, the shape of the propagating signal was examined with the help of a deterministic linear approximation derived by applying the invariant imbedding technique to the set of coupled equations governing the leftgoing and rightgoing wave components. It extends to dispersive waves the result by O'Doherty and Anstey [49] for acoustic waves. The input data for the mentioned approximation are solely the Fourier content of the incoming pulse and the correlation function of the orography's properties. Thus, its computation results inexpensive. Our theory is valid for smooth initial disturbances (in space) with effective compact support and arbitrary orographies. This means that it is applicable to waves such as Gaussian-shaped pulses and solitary waves.

The prediction of the theoretical formula is that the inhomogeneities of the orography together with the model's dispersion strongly affect the shape of the incoming pulse which is progressively attenuated, broadened and delayed as it propagates, as a consequence of the multiple reflections of the signal with the variable orography. These phenomena are more noticeable as the pulse travels large distances.

Several numerical simulations were performed for different levels of dispersion and non-linearity in order to validate the theory. This was accomplished by using a high accuracy finite difference numerical solver which models very well the dispersive characteristics of system (2.1) and captures the small scale structure of the disordered orography with a low computational cost.

In the hyperbolic regime ($\beta = 0$) the level of nonlinearity (controlled by parameter $\alpha$) was progressively increased to evaluate the limits of application of the linear theory. The agreement between theory and simulations was observed up to $\alpha = 0.003$. The pulse-shaping formula reproduces with high accuracy not only the deterministic coherent part of the signal (constituted by part of the initial wave energy) but also a segment of the unstructured forward scattering radiation constituted by multiple scattered energy being filtered back by the orography. For an even larger value of nonlinearity $\alpha = 0.005$, nonlinear effects dominate and a shock arises in the wave front and the linear theory is no longer applicable.

In the weakly dispersive regime, the dispersion and nonlinearity parameters were pushed up to $\alpha = \beta = 0.01$. No shock was observed in this situation due to the balance between nonlinear and dispersive effects. We found again that the linear theory furnishes an accurate prediction for the shape of the transmitted signal. Gaussian disturbances and weak solitons ($\alpha = \beta = 0.005$) were considered. Our results also indicate that the orography destroys the dispersive oscillatory coda, being the Fourier modes of smallest localization length (equivalently highest frequency) who are first filtered by the fluctuations of the depth.

From the foregoing results we conclude that the new dispersive pulse-shaping theory provides a valuable tool for understanding the interplay between weak dispersion and orography in waves with small amplitude.

The nonlinear effects are not negligible for larger values of parameter $\alpha$ in system (2.1) and gradually linear prediction and numerical simulation separate. In this connection we think that some of the ideas employed here in the linear equations could be useful in developing a full nonlinear theory, accounting in particular solitary waves.

The generalized O'Doherty-Anstey approximation presented in this work is very robust. This is due to the stabilization property which guarantees that the shape of the coherent front varies very little when a different orography's realization is considered. In contrast, the random fluctuations following the deterministic head pulse do not stabilize and depend highly upon the particular realization of the orography. This phenomenon was verified numerically both for Gaussian pulses and for weak solitary waves.

Finally, we confirmed the property of a highly variable medium to refocuse a pulse sent through it. For dispersive waves we used the time-reversal method in part of the reflected signal like in previous works [17], [52] on refocusing in acoustic waves. We found new theoretical and numerical results for the dispersive model (2.1). In particular, we derived a deterministic formula in the linear case which gives a reasonable prediction for the refocused pulse, even reproducing part of the noise which appears around it. The theory also proved to be applicable for weak solitons with $\alpha = \beta = 0.001$. However a slight discrepancy in amplitude was observed between theory and numerical simulation which at this moment we attribute to the linear approximation introduced in the reflection coefficient. Our opinion is that this approximation can be improved and we intend to explore this subject in more detail in a future work.

In addition, for Gaussian disturbances our numerical experiments indicated that the shape of the refocused pulse does not appear to be affected by the value of the dispersion parameter. Thus the dispersive oscillatory coda (observed at intermediate time stages) is compressed and disappears completely at the exact moment in that the refocusing takes place. This was verified up to $\beta = 0.01$ and $\alpha = 0.001$ and it would be interesting to perform a further numerical study for a broad range of values of dispersion and nonlinearity in order to grasp these new facts and get some insight on the effect of nonlinearities in the refocusing process. The development of theoretical results on soliton refocusing is an open problem to be explored.

The stabilization aspect was also systematically verified in the refocused pulse in a great number of numerical simulations over different realizations of the orography. We remark that the stabilization property does not follow directly from our results which are of a deterministic nature. Probabilistic techniques are required for a complete treatment of the problem.

# Appendix A

# Solutions for the linear KdV Equation and the linear Boussinesq model

### The linear KdV equation

Consider the initial value problem

$$u_t + u_x + \gamma u_{xxx} = 0, \tag{A.1}$$
$$u(x,0) = f(x), \tag{A.2}$$

where $\gamma$ is a nonzero constant.
Taking Fourier transform in $x$ of equations (A.1) and (A.2) we have

$$\begin{aligned} \hat{u}_t(k,t) &= i(-k+\gamma k^3)\hat{u}(k,t), \\ \hat{u}(k,0) &= \hat{f}(k). \end{aligned}$$

The solution of this initial problem value is

$$\hat{u}(k,t) = \hat{f}(k)e^{i(-k+\gamma k^3)t}$$

Now applying the Fourier inversion formula it results that

$$u(x,t) = \frac{1}{2\pi}\int_{-\infty}^{\infty} \hat{f}(k)e^{i(-k+\gamma k^3)t}e^{ikx}dk \tag{A.3}$$

or equivalently,

$$u(x,t) = \frac{1}{2\pi}\int_{-\infty}^{\infty}\left(\int_{-\infty}^{\infty} e^{i(k(x-t-y)+\gamma k^3 t)}dk\right) f(y)dy. \tag{A.4}$$

According to equation (A.3) the **dispersion relation** for the KdV equation (A.1) is

$$\omega = \omega(k) = k - \gamma k^3. \tag{A.5}$$

This relation implies in the **phase velocity**

$$C_k = \frac{\omega}{k} = 1 - \gamma k^2,$$

meaning that the velocity of any Fourier mode depends on the wave number $k$ and it is unbounded for short waves with $k \to \infty$. This is an important characteristic of a **dispersive equation** like (A.1). In contrast, in an hyperbolic model the phase velocity is a constant independent of $k$.

On the other hand, making a convenient change of variables, the inner integral in equation (A.4) can be expressed in terms of the Airy function to give

$$u(x,t) = \frac{1}{(3t\gamma)^{1/3}}\int_{-\infty}^{\infty} \mathrm{Ai}\left(\frac{x-t-y}{(3t\gamma)^{1/3}}\right) f(y)dy. \tag{A.6}$$

We conclude that the solution spreads at a rate proportional to the cubic root of the time $t$. This gives a valuable information for the invariant imbedding technique used in Chapter 2 due to the connection between the KdV equation (A.1) and the linear terrain-following system (2.20) as explained in the next section.

### The Linearized Boussinesq Model

Now we study the linear Boussinesq system (2.20)

$$\begin{aligned} M(\xi)\eta_t + u_\xi &= 0, \\ u_t + \eta_\xi - \frac{\beta}{3}u_{\xi\xi t} &= 0, \end{aligned} \tag{A.7}$$

with the initial conditions

$$\eta(\xi,0) = u(\xi,0) = f(\xi).$$

We consider the case of constant depth ($M \equiv 1$). Analogously to the KdV equation we can apply the Fourier transform technique to obtain the explicit Fourier coefficients

$$\begin{aligned}
\hat{\eta}(k,t) &= \frac{\hat{f}(k)}{2}\Big(\Big(1-\sqrt{1+(\beta/3)k^2}\Big)\, e^{\frac{ikt}{\sqrt{1+\beta/3k^2}}} + \\
&\quad \Big(1+\sqrt{1+(\beta/3)k^2}\Big)\, e^{\frac{-ikt}{\sqrt{1+\beta/3k^2}}}\Big), && \text{(A.8)} \\
\hat{u}(k,t) &= \frac{\hat{f}(k)}{2\sqrt{1+(\beta/3)k^2}}\Big(\Big(1+\sqrt{1+(\beta/3)k^2}\Big)\, e^{\frac{-ikt}{\sqrt{1+\beta/3k^2}}} \\
&\quad -\Big(1-\sqrt{1+(\beta/3)k^2}\Big)\, e^{\frac{ikt}{\sqrt{1+\beta/3k^2}}}\Big). && \text{(A.9)}
\end{aligned}$$

First of all, notice that because of (A.8), (A.9) and

$$\sqrt{1+(\beta/3)k^2} = 1 + (k^2/6)\beta + O(\beta^2),$$

$$\frac{1}{\sqrt{1+(\beta/3)k^2}} = 1 - (k^2/6)\beta + O(\beta^2),$$

then, as expected for the left propagating pulse $L$,

$$\widehat{L}(t,k) = \hat{\eta}(t,k) - \hat{u}(t,k) \approx O(\beta) \approx 0,$$

provided that $\beta$ is small enough.

The dispersion relation for system (A.7) can be obtained by considering solutions of the form

$$\begin{aligned}
\eta(\xi,t) &= \frac{1}{2\pi}\int_{-\infty}^{\infty} \hat{\eta}_k e^{i(k\xi - wt)} dk, \\
u(\xi,t) &= \frac{1}{2\pi}\int_{-\infty}^{\infty} \hat{u}_k e^{i(k\xi - wt)} dk.
\end{aligned}$$

Therefore we conclude that

$$\omega^2 = \omega^2(k) = \frac{k^2}{1+\frac{\beta}{3}k^2}$$

or

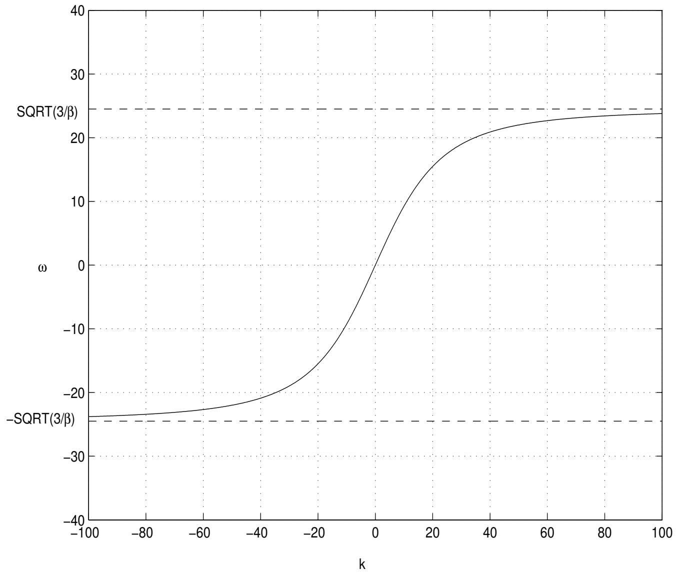


Figure A.1: Frequency $\omega_+$ as a function of the wave number $k$ for $\beta = 0.005$.

$$\omega_\pm = \omega_\pm(k) = \pm\frac{k}{\sqrt{1+\frac{\beta}{3}k^2}}, \tag{A.10}$$

where $\omega_+$ and $\omega_-$ represent Fourier modes propagating to the right and left, respectively. Thus the phase velocity is

$$C_k^\pm = \frac{\omega_\pm}{k} = \pm\frac{1}{\sqrt{1+\frac{\beta}{3}k^2}}. \tag{A.11}$$

As opposed to the KdV equation now the phase speeds are bounded by one. This is an important fact for applying the invariant imbedding technique used in Chapter 2. Furthermore, expanding $\omega_+ = \omega_+(k)$ in a Taylor series around $k = 0$ we find that

$$\omega_+(k) = k - \frac{\beta}{6}k^3 + O(k^5),$$

which **coincides** up to $O(k^3)$ with the dispersion relation for the KdV equation above with $\gamma = \beta/6$. (c.f. equations (A.1) and (A.5)). This is an important connection between these two models as mentioned before.

An interesting fact is observed when the time frequency $\omega_\pm$ (equation (A.10)) is plotted as a function of the wave number $k$ (see Figure A.1). We find that the range of possible time frequencies is bounded and

$$|\omega_\pm(k)| < \sqrt{\frac{3}{\beta}} \quad \text{for all } k.$$

As a consequence, solutions $u, \eta$ of system (A.7) are band-limited functions of $t$. In particular, this means that the Fourier transform

$$\hat{u}(\xi, \omega) = \int_{-\infty}^{\infty} u(\xi, t) e^{-it\omega} dt$$

satisfies that

$$\hat{u}(\xi, \omega) = 0, \text{ for all } |\omega| > \sqrt{\frac{3}{\beta}}.$$

This fact justifies why only a bounded band of frequencies was considered in the analysis in Chapter 2.

# Appendix B

# The invariant imbedding approach

For the sake of completeness in this appendix we present a brief summary of the main results on the invariant imbedding technique applied in this work in the study of the reflection-transmission problem in dispersive waves. We refer to the literature cited for a complete accounting on the subject.

Initially we develop the theory from a geometric point of view following [42]. This strategy enables us to obtain, in a very natural way, the whole set of invariant imbedding equations applicable in a great variety of problems, such as wave propagation and particle scattering, among others. Then we will present concrete applications which the invariant imbedding was first introduced [4]. In particular when applied to our problem of water waves we obtain the Riccati transformation (2.40) asserted in chapter 2 in the derivation of the generalized ODA approximation.

Consider the system of linear ordinary differential equations

$$\begin{aligned} z'(x) &= D(x)z(x) + C(x)y(x) + G(x), \\ y'(x) &= B(x)z(x) + A(x)y(x) + F(x), \end{aligned} \tag{B.1}$$

on $[0, X]$ and subject to the boundary conditions

$$y(0) = fz(0) + a, \quad g_1 y(X) + g_2 z(X) = b, \tag{B.2}$$

where $z \in \mathbb{R}^n$, $y \in \mathbb{R}^m$, $X > 0$ and $A, B, C, F, G$ matrices of consistent dimensions. Further $a, b, f, g_1, g_2$ are constant matrizes of consistent dimensions.

An interesting fact pointed out by Meyer [42] is that system (B.1) constitutes the set of characteristic equations corresponding to the quasilinear partial differential equation

$$u_x(x, z) + u_z(x, z)\left[C(x)u + D(x)z + G(x)\right] = A(x)u + B(x)z + F(x). \tag{B.3}$$

Thus a solution $\{z(x), y(x)\}$ of system (B.1) subject to the initial conditions $z(0) = s, \quad y(0) = fs + a$ can be **imbedded** into the integral surface $u(x, z)$ of (B.3) passing through the non-characteristic initial curve

$$u(x = 0, z) = fz + a. \tag{B.4}$$

This is what motivates Meyer [42] to call (B.3) the **invariant imbedding equation** associated with system (B.1).

From the Cauchy-Kowalevski theorem [28] we know that under some assumptions on the variable coefficients in equation (B.3), one unique solution to the Cauchy problem exists at least in a neighborhood of the initial curve (B.4). Now if in addition such a solution $u(x, z)$ exists for all $z$ and $x \in [0, X]$ and if the equation

$$g_1 u(X, z) + g_2 z = b, \tag{B.5}$$

has at least one solution $z = \hat{z}$ then it is easy to see that the characteristic curve $\{z(x), y(x)\}$ solution of system (B.1) subject to

$$z(X) = \hat{z}, \quad y(X) = u(X, \hat{z}) \tag{B.6}$$

is a solution of the boundary value problem (B.1)-(B.2). Notice the connection of these ideas with the **shooting method** used to solve boundary value problems [30].

The following theorem gives a characterization of the integral surfaces of equation (B.3).

**Theorem.** Suppose that the integral surface $u(x, z)$ solution of the Cauchy problem (B.3)-(B.4) exists for all $z$ and $x \in [0, X]$. Then $u(x, z)$ can be represented as

$$u(x, z) = U(x)z + v(x), \tag{B.7}$$

where matrix $U(x)$ satisfies the Riccati equation

$$U'(x) = B(x) + A(x)U - UD(x) - UC(x)U, \tag{B.8}$$

subject to

$$U(0) = f, \tag{B.9}$$

and $v(x)$ is solution of the initial value problem

$$\begin{aligned} v'(x) &= -\left[U(x)C(x) - A(x)\right] v - U(x)G(x) + F(x), \\ v(0) &= a. \end{aligned} \tag{B.10}$$

**Proof :** Except for a change of notation it corresponds to theorem 1.2.1 in Meyer [42], page 19.

Within the demonstration of the foregoing theorem is further shown that a characteristic curve $\{z(x), y(x)\}$, with $y(0) = fx(0) + a$ of $u(x, z)$, can be expressed as

$$z(0) = S(x)z(x) + \tilde{v}(x), \tag{B.11}$$

$$y(x) = U(x)z(x) + v(x), \tag{B.12}$$

where functions $S(x)$ and $\tilde{v}(x)$ solve the initial value problems

$$\begin{aligned} S'(x) &= -S(D(x) + C(x)U(x)), \\ S(0) &= 1, \end{aligned} \tag{B.13}$$

and

$$\begin{aligned} \tilde{v}'(x) &= -S(x)(C(x)v(x) + G(x)), \\ \tilde{v}(0) &= 0, \end{aligned} \tag{B.14}$$

respectively.

Functions $U(x)$ and $S(x)$ are commonly called the **reflection and transmission coefficients**. Remark that only function $U(x)$ occurs independently from others. Furthermore, the original boundary value problem (B.1)-(B.2) was decomposed in a sequence of initial value problems for several intermediate quantities introduced. This is a feature of the invariant imbedding strategy having important numerical and theoretical applications. Generalizations of this technique to nonlinear boundary value problems are also possible. However in that case the Riccati transformations (B.11) and (B.12) are no longer valid. See [54] and [42] for a discussion on these subjects. Existence and uniqueness theorems for the invariant imbedding equations, including Riccati equations, can be found in [6], [42] and references therein.

The invariant imbedding approach was first applied in steady-state particle transport problems in which equations of the form of (B.1) arise as the conservation laws for the relevant quantities in the system. This brings us to the original idea of invariant imbedding as conceived by Bellman and Kalaba in their pioneer paper [4] in 1956. Other related works are [5] and [7].

Consider a one-dimensional rod extending from $x = 0$ to $x = X_o$ which allows the transport of particles, for instance neutrons. Under some physical assumptions, a system of the form of (B.1) (in the scalar case) can be adopted as a very simple model for the interaction of particles (of the same kind) with the constituents of the medium rod [54]. This interaction is supposed to produce only forward or backward scattering, that is, neither fission (spontaneous generation of particles), collision or absorption of particles occur within the medium. Moreover, the medium's properties only depend upon the position $x$ and they are specified through the variable coefficients in system (B.1).

Within our simplified model, quantities $y(x)$ and $z(x)$ in system (B.1) can be interpreted as the densities of particles travelling to the right and to the left at the point $x$ within a medium's slab $0 \leq x \leq X \leq X_o$. Note that we have a **family of slabs** parametrized by its length $0 < X \leq X_o$ with $X_o$ the total length of the rod of interest. The mentioned family could be called **invariant** in the sense that its physical properties are preserved unaltered in each member of the family.

Further, accordingly with the nomenclature adopted above, when the solution $u(x, z)$ of the invariant imbedding equation (B.3) is evaluated at the interface $x = X$, it furnishes the density of particles emerging from that portion of the medium.

Here for simplicity we will suppose that there are no particle sources inside the medium and that all particles are incoming into the medium across the slab's rightside border $x = X$. There is no rightgoing flux of particles at the interface $x = 0$. Mathematically this amounts to take the forcing terms $F(x)$ and $G(x)$ in system (B.1) to be zero and set the two-point boundary conditions

$$y(0) = 0, \quad z(X) = b. \tag{B.15}$$

Thus the value $b$ specifies the density of particles entering the rod at the interface $x = X$.

For a fixed length $X$ consider now a subrod of medium $[0, x]$ **imbedded** into the slab $[0, X]$. Thus this subrod has the left end fixed at the origin and the right one variable at $x$. We can interpret the quantities $U(x)$, $S(x)$, $v(x)$ and $\tilde{v}(x)$ appearing in the Riccati transformations (B.11) and (B.12) in terms of the flux of particles across the borders of this subrod as follows :

(i) $S(x)$ gives the flux of leftgoing particles at the origin 0 as a consequence of an unity input of leftgoing particles at $x$.

(2i) $U(x)$ furnishes the flux of rightgoing particles at $x$ resulting from a unity input of leftgoing particles at point $x$. See the schematic figure B.1.

(3i) In a general situation, functions $v(x)$ and $\tilde{v}(x)$ correspond to contributions of fluxes of particles coming from the left of the border $x = 0$ or from sources located inside the medium. However in the current simplified problem, the boundary conditions (B.15) and the absence of forcing terms in equations (B.1) imply in $v(x) = \tilde{v}(x) = 0$. Analytically this can be deduced directly from the initial value problems defining these functions (c.f. equations (B.10) and (B.14)).

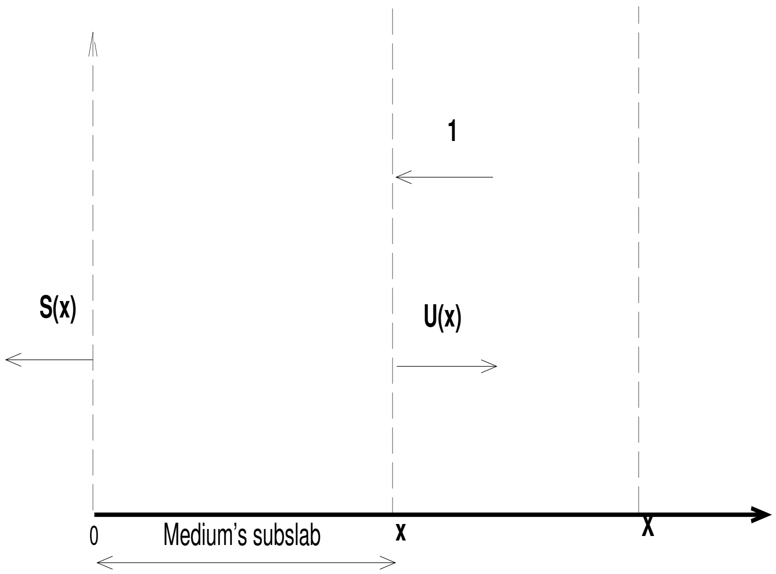


Figure B.1: Transmission and reflection coefficients defined in a subrod of medium $[0, x]$.

We point out that although we are primary interested in the values of quantities $z(x)$ and $y(x)$ at the borders of the slab $[0, X]$, equations (B.11) and (B.12) may indeed be used to solve for their interior values in terms of the reflection and transmission coefficients $U(x)$ and $S(x)$ (see [54], chapter 4). These coefficients are completely determined as solutions of the initial value problems (B.8)-(B.9) and (B.13).

Finally we concern the application of the invariant imbedding to the problem of dispersive water wave scattering studied in Chapter 2

$$\begin{aligned} \widehat{R}_x &= \zeta(x,\omega)\widehat{L} + \gamma(x,\omega)\widehat{R}, \\ \widehat{L}_x &= (2i\omega + \bar{\gamma}(x,\omega))\widehat{L} + \bar{\zeta}(x,\omega)\widehat{R}, \end{aligned} \tag{B.16}$$

subject to the two-point boundary conditions

$$\begin{aligned}\widehat{R}(x_o,\omega) &= \hat{h}(\omega), \\ \widehat{L}(x_o+X,\omega) &= 0,\end{aligned} \tag{B.17}$$

governing the evolution in $x$ of the rightgoing and leftgoing propagating wave modes for the terrain-following system (2.20). It should be noticed its analogy with the particle transport problem discussed above.

Frequency $\omega$ remains constant here and thus for simplicity we will omit it in the arguments of the coefficients in what follows. The equations of the invariant imbedding for problem (B.16)-(B.17) on the interval $[x_o, x_o+X]$ are obtained in a similar fashion as equations (B.8), (B.11),(B.12) and (B.13), yielding that

$$\widehat{R}(x_o+X) = \widehat{T}(x_o)\widehat{R}(x_o), \tag{B.18}$$

$$\widehat{L}(x_o) = \widehat{K}(x_o)\widehat{R}(x_o), \tag{B.19}$$

where the coefficients $\widehat{T}$ and $\widehat{K}$ solve

$$\widehat{K}_x = \overline{\zeta}(x) + 2i\omega\Gamma(x)\widehat{K} - \zeta(x)\widehat{K}^2, \tag{B.20}$$

$$\widehat{K}(x_o+X) = 0, \tag{B.21}$$

and

$$\begin{aligned}\widehat{T}_x &= -\widehat{T}(\gamma(x)+\zeta(x)\widehat{K}(x)), \\ \widehat{T}(x_o+X) &= 1.\end{aligned} \tag{B.22}$$

In particular, equations (B.19) and (B.20) correspond to equation (2.40) and to the Riccati equation (2.41), respectively, as stated in Chapter 2. The reflection coefficient $\widehat{K}$ describes the influence of the rightgoing component (the transmitted signal) upon the leftgoing field (the reflected signal) at a given position $x_o$ into the medium.

Notice also that equations (B.18) and (B.19) are consistent when the medium in the slab $[x_o, x_o+X]$ is nondispersive and homogeneous ($\beta = \zeta = \gamma = 0$). For in this case, we have that $\widehat{K} \equiv 0$, $\widehat{T} \equiv 1$, which in turn implies in $\widehat{R}(x_o+X) = \widehat{R}(x_o)$ and $\widehat{L}(x_o) = 0$. Thus as expected, no reflections are produced into the slab and the incoming signal at $x_o$ equals to the outcome one across the border $x_o+X$.

In the nonhomogeneous case, the transmission coefficient $\widehat{T}$ (c.f. equation (B.18)) regulates the amount of outcome transmitted energy across the righthand border $x_o+X$ after multiple reflections of the signal with the section of orography covering the slab $[x_o, x_o+X]$.

# Appendix C

# Validation of consistency of the pulse-shaping theory

In the purely dispersive regime (i.e. $M \equiv 1, \quad 0 < \beta \quad << 1$) we can validate directly the consistency of the general O'Doherty-Anstey approximation (2.60) which in this case results in

$$\begin{aligned} \widehat{R}(x_o,\omega) &\approx \hat{f}(\omega)\exp\left[\int_0^{x_o} - \int_x^{x+X} \frac{i\beta\omega^3}{6(1-(\beta/3)\omega^2)} e^{2i\omega\frac{2-(\beta/3)\omega^2}{2(1-(\beta/3)\omega^2)}(x-x')} \cdot \right. \\ &\quad \left. \frac{-i\beta\omega^3}{6(1-(\beta/3)\omega^2)} dx'dx\right] \exp\left[-\frac{\beta i\omega^3 x_o}{2(3-\beta\omega^2)}\right] \\ &\approx \hat{f}(\omega)\ \exp[O(\beta^2)]\ \ \exp\left[-\frac{\beta i\omega^3 x_o}{2(3-\beta\omega^2)}\right]. \end{aligned} \tag{C.1}$$

This approximation leads us to the estimate $a_\beta(x_o,\omega) \approx a_0(x_o,\omega)$ for $\beta$ small in Chapter 2 which simplifies the computation of the generalized pulse-shaping formula (see equation (2.61)).

This last equation implies in the approximation

$$\begin{aligned} \widehat{R}(x_o,\omega) &\approx \hat{f}(\omega)e^{-\frac{\beta i\omega^3 x_o}{2(3-\beta\omega^2)}} \\ &\approx \hat{f}(\omega)e^{-\frac{\beta i\omega^3 x_o}{6}}, \end{aligned} \tag{C.2}$$

where the error committed is of $O(\beta^2)$.

Now by using the Fourier inversion formula we find that

$$R(x_o,\tau) \approx \frac{1}{2\pi}\int_{-\infty}^{\infty} \hat{f}(\omega)e^{-\frac{\beta i\omega^3 x_o}{6}} e^{i\omega\tau}d\omega,$$

which can be expressed in terms of the Airy function as

$$R(x_o,\tau) \approx \frac{1}{(3x_o(\beta/6))^{1/3}} \int_{-\infty}^{\infty} \mathrm{Ai}\left(-\frac{\tau-y}{(3x_o(\beta/6))^{1/3}}\right) f(y)dy. \tag{C.3}$$

Note that approximation (C.3) for the right propagating pulse looks like equation (A.6) in Appendix A for the KdV equation with $\gamma = \beta/6$. The role of time and space are reversed because here $x_o$ is travel time.

On the other hand, directly from system (2.28) for $r \equiv 0$, we have

$$R_t + R_x = \frac{\beta}{6}(R-L)_{xxt}, \tag{C.4}$$

$$L_x - L_t = \frac{\beta}{6}(R-L)_{xxt}. \tag{C.5}$$

We will show that equations (C.4) and (C.5) can be formally approximated by the decoupled system

$$\begin{aligned} R_t &= -\left(\partial_x + \frac{\beta}{6}\partial_t^2\partial_x\right) R, \\ L_t &= \left(\partial_x + \frac{\beta}{6}\partial_t^2\partial_x\right) L. \end{aligned}$$

which may be solved explicitly. To this goal, following an analogous technique of Mattioli's [39], we differentiate equation (C.4) with respect to $t$ and $x$ alternatively and subtract the resulting equations to obtain

$$R_{tt} - R_{xx} = \frac{\beta}{6}(R-L)_{xxtt} - \frac{\beta}{6}(R-L)_{xxxt}. \tag{C.6}$$

Next equations (C.4) and (C.5) imply in

$$R_t = -R_x + O(\beta), \tag{C.7}$$

$$L_x = L_t + O(\beta). \tag{C.8}$$

By inserting relationships (C.7) and (C.8) into equation (C.6) we find that $R$ satisfies the equation

$$R_{tt} - R_{xx} = \frac{\beta}{3} R_{xxtt}, \tag{C.9}$$

with an error of $O(\beta^2)$.

Analogously $L$ satisfies the equation

$$L_{xx} - L_{tt} = -\frac{\beta}{3} L_{xxtt}. \tag{C.10}$$

Equivalently, we can write equations (C.9) and (C.10) as

$$R_{tt} = (\partial_x^2 + \frac{\beta}{3}\partial_x \partial_t^2 \partial_x) R, \tag{C.11}$$

$$L_{tt} = (\partial_x^2 + \frac{\beta}{3}\partial_x \partial_t^2 \partial_x) L. \tag{C.12}$$

Now committing an error of $O(\beta^2)$ we add the terms $(\beta/6)^2 \partial_t^4 \partial_x^2 R$ and $(\beta/6)^2 \partial_t^4 \partial_x^2 L$ to the right side of equations (C.11)-(C.12), respectively, yielding that

$$\begin{aligned} R_{tt} &= \left( \partial_x^2 + \frac{\beta}{3}\partial_x \partial_t^2 \partial_x + \left(\frac{\beta}{6}\right)^2 \partial_t^4 \partial_x^2 \right) R, \\ L_{tt} &= \left( \partial_x^2 + \frac{\beta}{3}\partial_x \partial_t^2 \partial_x + \left(\frac{\beta}{6}\right)^2 \partial_t^4 \partial_x^2 \right) L. \end{aligned} \tag{C.13}$$

In this way, the differential operators on the right side of equations (C.13) can be factored to give

$$\begin{aligned} R_{tt} &= \left( \partial_x + \frac{\beta}{6}\partial_t^2 \partial_x \right)^2 R, \\ L_{tt} &= \left( \partial_x + \frac{\beta}{6}\partial_t^2 \partial_x \right)^2 L. \end{aligned} \tag{C.14}$$

Equations (C.14) imply that $R$ and $L$ satisfy

$$R_t = -\left( \partial_x + \frac{\beta}{6}\partial_t^2 \partial_x \right) R, \tag{C.15}$$

$$L_t = \left( \partial_x + \frac{\beta}{6}\partial_t^2 \partial_x \right) L. \tag{C.16}$$

Notice that equations (C.14) allow other possible decompositions for $R$ and $L$. Nevertheless they are formally equivalent up to $O(\beta^2)$.

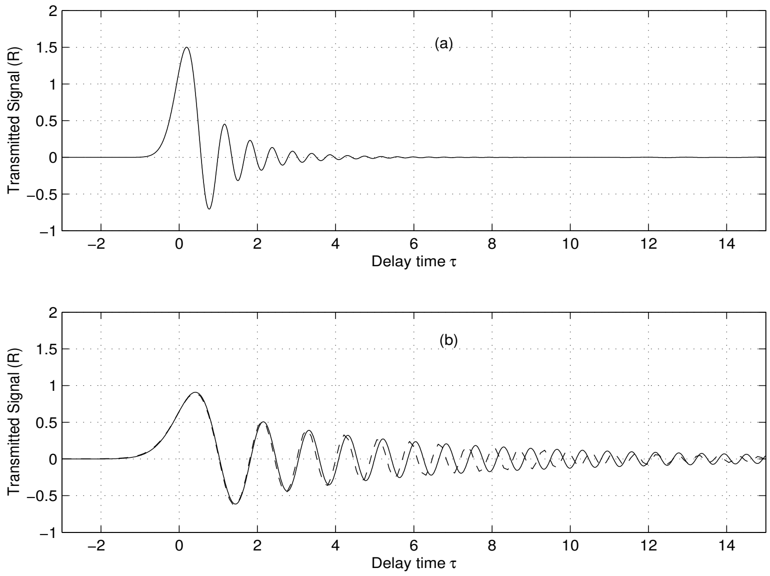


Figure C.1: Pulse propagating over a flat bottom. (a) Initial disturbance $f(\tau)$. (b) Dashed line : Numerical solution for $\alpha = 0.001$, $\beta = 0.005$ at $\xi = 30$. Solid line : Approximation (C.3)

System (C.15)-(C.16) can be solved explicitly for $R$ and $L$. For instance, by expressing equation (C.15) in the time-delay variable $\tau$ we find that

$$R_x = \frac{\beta}{6} R_{\tau\tau\tau} - \frac{\beta}{6} R_{x\tau\tau}. \tag{C.17}$$

Taking Fourier Transform in $\tau$ leads to

$$\left(1 - \frac{\beta}{6}\omega^2\right) \widehat{R}_x = -\frac{\beta i \omega^3}{6} \widehat{R}.$$

If $\widehat{R}(0, \omega) = \hat{f}(\omega)$ we conclude that

$$\begin{aligned} \widehat{R}(x_o, \omega) &= \hat{f}(\omega) e^{-\frac{\beta i \omega^3 x_o}{6(1-(\beta/6)\omega^2)}} \\ &\approx \hat{f}(\omega) e^{-\frac{\beta i \omega^3 x_o}{6}} e^{O(\beta^2)}. \end{aligned} \tag{C.18}$$

Finally comparing estimate (C.18) to approximation (C.2) we find that the error is of $O(\beta^2)$.

In Figure C.1 we compare approximation (C.3) to the numerical solution of the nonlinear Boussinesq system for the parameters $\alpha = 0.001$ and $\beta = 0.005$. The initial pulse $f(\tau)$ in time is computed as indicated in Sections 3.2 and 3.3. We observe that this approximation reproduces very well the wave front and part of the oscillatory coda.

# Appendix D

# Numerical computation of the coefficients $a_\beta(x_o, \omega)$ and $b(x_o, \omega)$

As mentioned in Chapter 2, the numerical computation of the dispersive coefficient $a_\beta(x_o, \omega)$ is expensive. To override this difficulty we approximated it by the hyperbolic medium's correlation function $a_0(x_o, \omega)$, which corresponds to the leading order term of a Taylor series expansion of $a_\beta$ around $\beta = 0$. The numerical experiments in Section 3.2 and 3.3 showed the high accuracy of this approximation.

To compute coefficient $a_0(x_o, \omega)$ as in equation (2.61) we rewrite it as

$$a_0(x_o, \omega) = \frac{1}{x_o} \int_0^X \Phi(\eta) e^{-2i\omega\eta} d\eta, \tag{D.1}$$

where

$$\Phi(\eta) = \int_0^{x_o} r(x) r(x + \eta) dx.$$

We know by the correlation theorem that

$$\int_{-\infty}^{\infty} r(x) r(x + \eta) dx = F^{-1}[\hat{r}\overline{\hat{r}}](\eta),$$

where the hat denotes the Fourier transform, $F^{-1}$ the inverse Fourier transform and the bar indicates complex conjugation. Therefore function $\Phi$ defined above can be computed by using the FFT (Fast Fourier Transform) algorithm letting the coefficient $r(x)$ be zero outside the interval $[0, x_o]$. This is consistent with the invariant imbedding approach used in Chapter 2. We must append enough zeros to the tail of the sampled coefficient $r(x)$ (zero padding) in order to eliminate the overlapping phenomenon that appears due to the fact that $r(x)$ is not a periodic function. The Fast Fourier Transform assumes periodicity in both physical and frequency domains (see Brigham [10]). The cost of computing the discrete correlation function results in only three FFT evaluations which is faster than an ordinary computation of the integral defining $\Phi$ for each value of $\eta$. The numerical code to perform the discrete correlation can be found in [10].

Once the function $\Phi$ is known, the windowed Fourier transform in equation (D.1) is evaluated by using only one FFT. Analogously to the discrete correlation zero padding outside the interval $[0, X]$ is required on the sampling of function $\Phi$.

The complete evaluation of the generalized ODA approximation also requires the dispersive coefficient $b(x_o, \omega)$ and the initial pulse in time $f(\tau)$ (c.f. equation (2.60)). To make the computation faster we make a change of variables in its integral, yielding that

$$b(x_o, \omega) = -\frac{\beta}{6x_o} \int_0^{\xi(x_o)} \frac{-i\omega^3 M^{3/2}(\xi) + M'(\xi)\omega^2}{1 - (\beta/3)M(\xi)\omega^2} d\xi, \tag{D.2}$$

where the upper limit $\xi(x_o)$ denotes the medium's position corresponding to the travel time $x_o$. Thus we must compute only once the coefficients $M(\xi)$, $M^{3/2}(\xi)$ and $M'(\xi)$ which can be stored at the beginning. The integral in (D.2) is approximated by the trapezoidal method for roughly $2^{14}$ frequencies in the range $|\omega| < \sqrt{3/\beta}$. Due to $b(x_o, -\omega) = \overline{b(x_o, \omega)}$, only positive frequencies must be computed.

Finally the transmitted initial pulse at the medium's position $\xi = 0$ can be approximated by using the numerical code described in Chapter 3. In this step the computational domain is set to be the interval $-6 \leq \xi \leq 1$ and the spatial mesh size is taken to be 300 nodes. We point out that the radiation conditions (3.8)-(3.9) can be imposed at the boundaries of this interval since the channel is flat over the longer interval $[-\infty, 5]$. Thus the waves are allowed to leave the computational domain without affecting the inner solution.

The total time of computation of all theoretical components of the ODA approximation is of approximately 3 minutes for the numerical experiments presented in this work. This is contrasted to the fact that it takes 40 minutes approximately to obtain similar results if we perform a complete simulation by using our numerical code. Thus, in addition to the theoretical results, the ODA approximation gives us an inexpensive and accurate prediction for a long distance propagation of the coherent transmitted signal provided that the strength of the system's nonlinearities are sufficiently small so that the linear theory applies.

# Appendix E

# Error estimation of the pulse-shaping theory

In Chapter 2 the Fourier transform of the reflection kernel is decomposed as

$$\widehat{K}(x_o,\omega) = -\int_{x_o}^{x_o+X} e^{2i\omega\int_{x'}^{x_o}\Gamma(s,\omega)\,ds}\bar{\zeta}(x',\omega)dx' + E(x_o,\omega), \tag{E.1}$$

where

$$E(x_o,\omega) = \int_{x_o}^{x_o+X} e^{2i\omega\int_{x'}^{x_o}\Gamma(s,\omega)\,ds}\zeta(x',\omega)\widehat{K}^2(x',\omega)dx'. \tag{E.2}$$

In the derivation of the generalized ODA approximation (under the hypothesis of rapidly-varying orography and weakly-dispersive regime $0 < \beta << 1$) we retain the first term on the right side of equation (E.1) and neglect the frequency-dependent function $E(x_o,\omega)$ leading to the approximation

$$\widehat{K}(x_o,\omega) \approx -\int_{x_o}^{x_o+X} e^{2i\omega\int_{x'}^{x_o}\Gamma(s,\omega)\,ds}\bar{\zeta}(x',\omega)dx'. \tag{E.3}$$

In this Appendix we wish to provide numerical evidence showing the accuracy of this approximation. First of all, the reflection coefficient $\widehat{K}$ can be computed by solving numerically the Riccati equation

$$\widehat{K}_x = \bar{\zeta}(x,\omega) + 2i\omega\Gamma(x,\omega)\widehat{K} - \zeta(x,\omega)\widehat{K}^2,$$

subject to

$$\widehat{K}(x_o + X, \omega; T) = 0.$$

Consequently, we can evaluate the error function $E(x_o, \omega)$ at any time $x_o$ and frequency $\omega$.

The results are presented in Figure E.1 where we compare the norm of the function $E(x_o, \omega)$ to that of approximation (E.3) at the point $\xi = 40$, $X = 10$ and $\beta = 0.005$. We see that the error function results negligible for any frequency. The orography's parameters used in this experiment are $L_o = 240$ (total length of the rough bottom) , $\ell = 0.6$ (scale of variation of the bottom's irregularities) and $\delta = 0.5$ (bottom's fluctuations amplitude).

We point out that in this case and for more general topographies, error estimate (2.54) deduced in Chapter 2 is not sharp because the coefficient $r(x)$ may be large. However its magnitude can be controlled in a Goupillaud layered discrete medium and estimate (2.54) is useful in this situation. This special type of medium is used by Papanicolaou et al. [12], [32] to validate the ODA theory for acoustic pulse propagation in random media. The properties describing a Goupillaud medium are piecewise constant and the pulse's travel time within each layer is always the same.

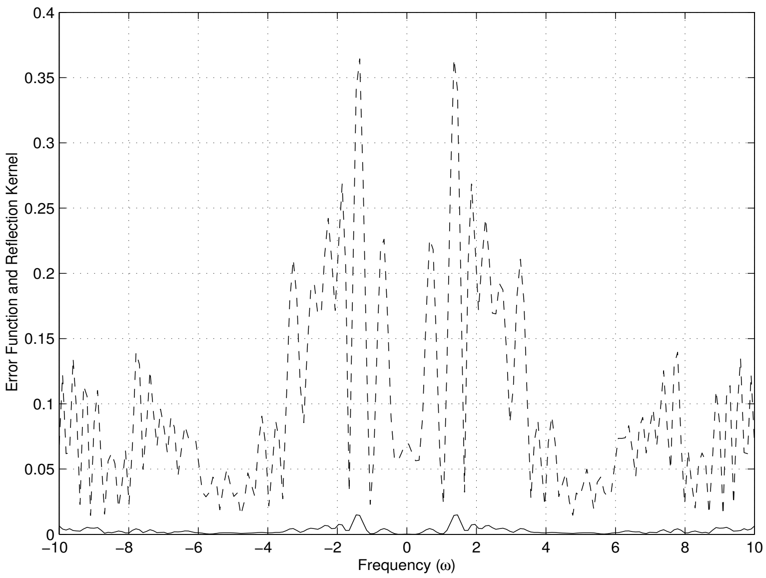


Figure E.1: Solid line : Error's norm for $\beta = 0.005$, $X = 10$ at $\xi = 40$. Dashed line : norm of approximation (E.3) for the same parameters.

To construct a Goupillaud type medium for the coupled mode system (2.28) we discretize the local wave velocity $C_o(x)$ as

$$C_o(x) = \begin{cases} 1 + \delta e^{z_k/\sqrt{N}}, & x \in (\frac{k}{N}, \frac{k+1}{N}], \\ 1, & x \in (-\infty, 1/N] \cup (1, \infty), \end{cases} \tag{E.4}$$

where $z_k$, $k = 1, ..., N-1$, is a sequence of random numbers in $[-1, 1]$, $N > 0$ indicates the number of layers in the medium and $\delta > 0$ regulates the amplitude of the medium's fluctuations. The scaling by $1/\sqrt{N}$ in (E.4) is important so that the incoming pulse feels the bottom irregularities after travelling through $N$ layers. Moreover as shown bellow, this scaling leads to a local reflection coefficient $r(x)$ of $O(1/\sqrt{N})$, small when $N >> 1$ and therefore estimate (2.54) applies. Note also that even though in the travel time variable $x$ the layers are equally spaced $1/N$ this is not necessarily true in the spatial variable $\xi$.

Error estimate (2.54) can be simplified into

$$|E(x_o, \omega)| \leq \frac{V^3(x_o, \omega)}{1 - V^2(x_o, \omega)}. \tag{E.5}$$

In the present analysis we assume that $0 < \beta << 1$, $N >> 1$ and $O(\omega) = 1$. Taking the absolute value of $V(x_o, \omega)$ we have

$$|V(x_o, \omega)| \leq \int_{x_o}^{x_o+X} \frac{|d(x)\omega^3|}{2(1 - d(x)\omega^2)} + \frac{|r(x)|\,(d(x)\omega^2 + 1)}{1 - d(x)\omega^2} dx. \tag{E.6}$$

Now suppose that $x_j = x_o$ and $x_{j+p+1} = x_o + X$ with $O(X) = O(p) = 1$ and let $x_k = k/N$. Then using that $d(x) = O(\beta)$ and

$$|r(x_k)| = \left| \frac{C_o(x_{k+1}) - C_o(x_k)}{C_o(x_{k+1}) + C_o(x_k)} \right| \leq \left| \tanh \left[ \frac{1}{2\sqrt{N}} (z_{k+1} - z_k) \right] \right| \leq \frac{1}{\sqrt{N}}$$

into equation (E.6) leads to

$$|V(x_o, \omega)| = O(\beta) + O(1/\sqrt{N}). \tag{E.7}$$

Therefore from equation (E.5) we arrive at the error estimate

$$|E(x_o, \omega)| \leq \frac{(O(\beta) + O(1/\sqrt{N}))^3}{1 - (O(\beta) + O(1/\sqrt{N}))^2} = (O(\beta) + O(1/\sqrt{N}))^3.$$

As a consequence, the error's norm goes to zero when $N \to \infty$ and $\beta \to 0$.

# Appendix F

# Mattioli's decomposition of a Boussinesq-type system

Consider

$$
\begin{aligned}
&\eta_t + [(h+\alpha\eta)u]_x = -\beta\frac{\partial}{\partial x}\left[\frac{\partial}{\partial x}\left(\frac{1}{3}h^3u_x\right)+\frac{1}{2}h^2h_{xx}u\right], \\
&u_t + g\eta_x + \frac{\alpha}{2}(u^2)_x = 0,
\end{aligned} \tag{F.1}
$$

where $t$ is time, $x$ the space variable, $h$ the depth, $\eta = \eta(x,t)$ is the wave elevation, $u = u(x,t)$ is the surface velocity, $g$ is the gravity acceleration, $\alpha = a_o/h_o$, $\beta = (k_oh_o)^2$ are dimensionless parameters with $a_o$ the characteristic pulse's amplitude, $h_o$ the characteristic depth and $k_o$ the typical wavenumber.

When $\alpha = 0$, Mattioli [39] decomposes system (F.1) into the pair of coupled KdV-type equations

$$
\begin{aligned}
\eta_t^+ + c\eta_x^+ &= -\frac{1}{2}c_x(\eta^+-\eta^-) - \beta\frac{\partial}{\partial x}\left[\frac{\partial}{\partial x}\left(\frac{1}{6}h^2c^2\frac{\partial}{\partial x}\left(\frac{1}{c}(\eta^+-\eta^-)\right)\right)\right. \\
&\quad \left.\frac{1}{4}hh_{xx}c(\eta^+-\eta^-)\right], \qquad \text{(F.2)} \\
\eta_t^- - c\eta_x^- &= -\frac{1}{2}c_x(\eta^+-\eta^-) - \beta\frac{\partial}{\partial x}\left[\frac{\partial}{\partial x}\left(\frac{1}{6}h^2c^2\frac{\partial}{\partial x}\left(\frac{1}{c}(\eta^+-\eta^-)\right)\right)\right. \\
&\quad \left.\frac{1}{4}hh_{xx}c(\eta^+-\eta^-)\right],
\end{aligned} \tag{F.3}
$$

where $c = c(x) = \sqrt{gh(x)}$ is the shallow water velocity.

Considering the depth $h$ constant and test pulses of the form

$$\eta(x,t) = \hat{\eta}_k e^{i(kx-\omega t)}, u(x,t) = \hat{u}_k e^{i(kx-\omega t)},$$

in system (F.2), leads to the dispersion relation

$$C_k^2 = \frac{\omega^2}{k^2} = c^2\left(1 - \frac{\beta h^2 k^2}{3}\right), \tag{F.4}$$

which shows that system (F.2) amplifies short waves with $k > (1/h)\sqrt{3/\beta}$. In contrast, the dispersion relation for system (2.28) in constant depth ($r \equiv 0$),

$$\begin{aligned} R_t + R_x &= \frac{\beta}{6}(R-L)_{xxt}, && \text{(F.5)} \\ L_x - L_t &= \frac{\beta}{6}(R-L)_{xxt} && \text{(F.6)} \end{aligned}$$

is given by

$$C_k^2 = \frac{\omega^2}{k^2} = \frac{1}{1+\frac{\beta}{3}k^2}, \tag{F.7}$$

which is bounded as a function of the wavenumber $k$. As we said in Appendix A this fact is important for the theory developed in Chapter 2.

# Appendix G

# Estimation of the scattering parameters $\alpha_o$, $\mu$, $\sigma$ and $\lambda$

Our intent in this appendix is to give details on the numerical computation of the parameters involved in approximations (2.71) (for $0 < \beta << 1$) and (2.78) (for $\beta = 0$). In Section 2.7 they are defined by

$$\begin{aligned}
\alpha_o &= \alpha_o(x_o) = a_0(x_o, 0) \\
\mu &= \mu(x_o) = -ia_0'(x_o, 0) \\
\sigma &= \sigma(x_o) = \frac{a_0''(x_o, 0) + b''(x_o, 0)}{2} \\
\lambda &= \lambda(x_o) = -i\left(\frac{a_0'''(x_o, 0) + b'''(x_o, 0)}{3!}\right).
\end{aligned} \tag{G.1}$$

Recall that coefficient $a_0(x_o, \omega)$ may be rewritten as

$$a_0(x_o, \omega) = \frac{1}{x_o}\int_0^X \Phi(\eta)e^{-2i\omega\eta}d\eta, \tag{G.2}$$

where

$$\Phi(\eta) = \int_0^{x_o} r(x)r(x+\eta)dx.$$

Note that only the local behavior of function $a_0(x_o, \omega)$ around the origin $\omega = 0$ is taken into account for the scattering parameters. Therefore the high frequency band of coefficient $a_0(x_o, \omega)$ is not being considered.

Because of our primary interest in the wave's coherent front, that is, the part of signal first arriving at the location of observation, the length of the invariant imbedding slab $X$

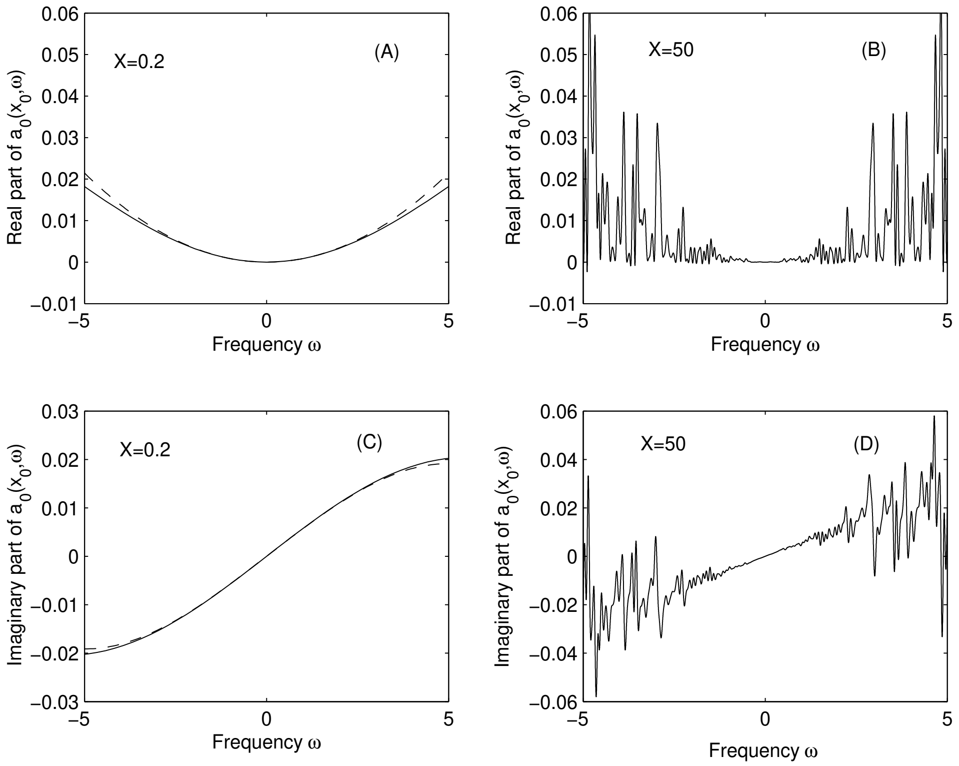


Figure G.1: In solid line is the correlation function $a_0(x_o, \omega)$ for two different values of parameter $X$ at the medium's position $x_o = 39.9404$ (equivalently $\xi = 40$). In (A) and (C) we plot in dashed line its 3rd-order Taylor approximation around the origin.

(used in (G.2)) need not be too large. Indeed taking it to be twice the orography's correlation length ($X = 2\ell$) suffices.

For this value of $X$ the correlation function can be approximated for a relatively large range of frequencies for its Taylor series at $\omega = 0$. This is crucial for the accuracy of approximations (2.71) and (2.78) (c.f. Section 2.7). In Figure G.1(A)-(C) we compare the correlation function for $X = 0.2$ with its Taylor series expansion around the origin. In this experiment the medium's fluctuations are located on interval [5,45], the amplitude of fluctuations is $\delta = 0.5$ and the orography's correlation length is $\ell = 0.1$. We will preserve these medium's parameters throughout this appendix.

In Figure G.1(A)-(C) also observe that in a neighborhood of the origin $\omega = 0$ the real part of coefficient $a_0(x_o, \omega)$ is approximately quadratic and **positive** and its imaginary part is locally linear with **positive slope**. This forces parameters $\sigma$ and $\mu$ to be positive accounting for the attenuation and delay of the incoming pulse (c.f. approximations (2.71) and (2.78)).

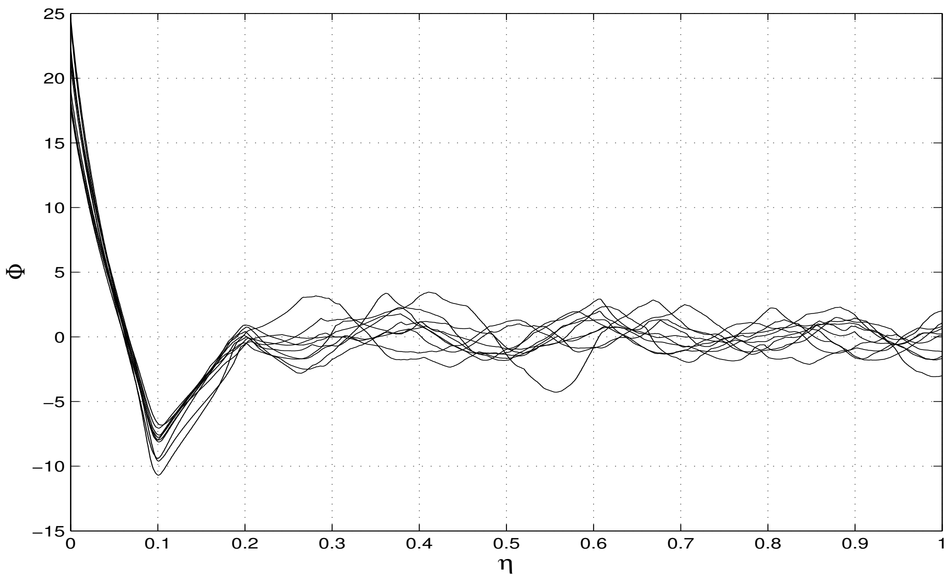


Figure G.2: Autocorrelation of the medium's properties computed at position $\xi = 20$ for ten different orography's realizations. Each solid line corresponds to a realization.

Meanwhile, a larger value of $X$ introduces "noise" around the origin in the correlation function as shown in Figure G.1(B)-(D) for $X = 50$ due to additional (unnecessary in this case) medium information introduced. As a consequence, its Taylor expansion represents it only in a narrower band of frequencies.

Our choice for parameter $X$ is also motivated by Figure G.2 where we plot the autocorrelation function $\Phi(\eta)$ (the inner integral in (G.2)) for ten different realizations of synthetized orographies at location $\xi = 20$. Observe that within roughly the interval $[0, 2\ell]$ ($\ell = 0.1$), the traces of $\Phi$ varies very little in each realization. We find similar results at other medium's positions. On the contrary, outside the mentioned interval they fluctuate without a determined pattern. This fact is closely related to the stabilization property of the coherent part of the wave discussed in Section 3.5.

Opposite to the correlation function, the dispersive coefficient does not depend on the parameter $X$ (c.f. equation (2.59)) and it is always a "clean" function whose real part is locally quadratic and its imaginary part is approximately cubic. We confirm these assertions in Figure (G.3) for $\beta = 0.002$.

Evaluation of parameter $\alpha_o$ is straightforward. To compute parameters $\mu$, $\sigma$ and $\lambda$ we approximate equations (G.1) to 2nd-order accuracy as

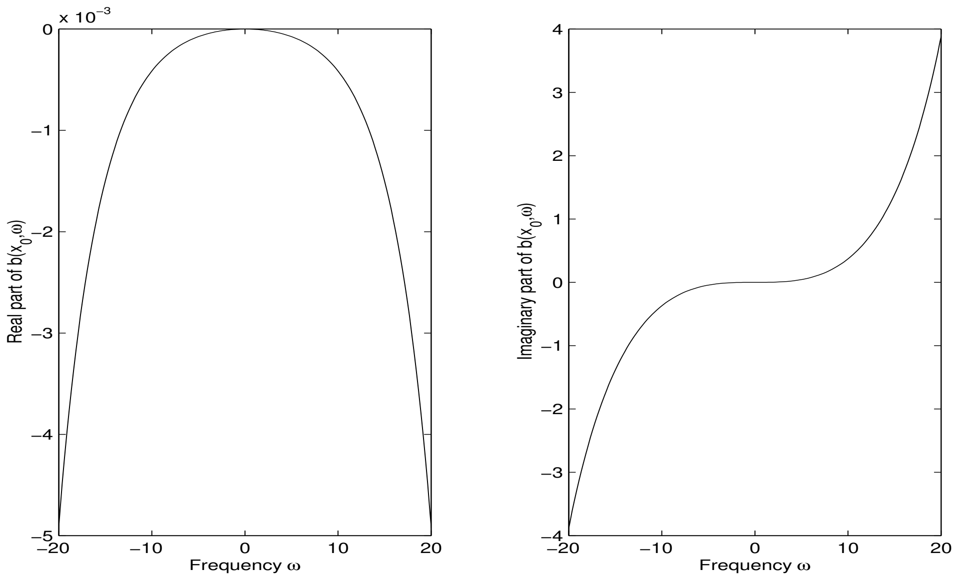


Figure G.3: Dispersive coefficient $b(x_o, \omega)$ for $\beta = 0.002$ at the medium's position $x_o = 39.9404$ (equivalently $\xi = 40$).

$$\begin{aligned}
\mu(x_o) &\approx -i\left(\frac{a_0(x_o, \Delta\omega) - a_0(x_o, -\Delta\omega)}{2\Delta\omega}\right) \\
\sigma(x_o) &\approx \frac{\varphi(x_o, \Delta\omega) - 2\varphi(x_o, 0) + \varphi(x_o, -\Delta\omega)}{2\Delta\omega^2} \\
\lambda(x_o) &\approx -i\left(\frac{\varphi(x_o, 2\Delta\omega) - 2\varphi(x_o, \Delta\omega) + 2\varphi(x_o, -\Delta\omega) - \varphi(x_o, -2\Delta\omega)}{12\Delta\omega^3}\right),
\end{aligned} \tag{G.3}$$

where $\varphi(x_o, \omega) = a_0(x_o, \omega) + b(x_o, \omega)$.

The values of the parameters at the medium position $\xi = 40$ obtained from estimates (G.3) are $\alpha_o = 5.2e-6$, $\mu = 5.8e-3$, $\sigma = 8.6e-4$. First we consider the hyperbolic regime $\beta = 0$. Recall that in such a case $\lambda = 0$. In Figure G.4 we compare the weakly-nonlinear numerical simulation with the hyperbolic approximation (2.78) for the parameters computed and they are found to be in good agreement. Observe that only the coherent front is captured by (2.78) and the forward scattering radiation is lost as expected.

Next we set the dispersion parameter to be $\beta = 0.002$. In the sequence of plots in Figure G.5 we display the transmitted signal at several stations into the medium and compare them to approximation (2.71) corresponding to the dispersive regime. The values of the parameters computed from equations (G.3) at every position are presented in table G.1.

| $\xi$ (Medium's position) | $\alpha_o$ | $\mu$ | $\sigma$ | $\lambda$ |
|---|---|---|---|---|
| 6 | -8e-4 | 1.4e-3 | 1.7e-4 | 3.2e-4 |
| 8 | -1.6e-3 | 3.6e-3 | 5.5e-4 | 2.8e-4 |
| 10 | -1.5e-3 | 4.1e-3 | 6e-4 | 2.8e-4 |
| 20 | -1.7e-3 | 5e-3 | 6.8e-4 | 2.9e-4 |
| 40 | 5.2e-6 | 5.8e-3 | 8.5e-4 | 2.6e-4 |

Table G.1: Scattering parameters at five medium's locations.

Remark that accordingly with our results, factor $e^{-x_o\alpha_o}$ in approximations (2.71) and (2.78) is negligible and indeed it could be taken to be zero. In the hyperbolic regime this is consistent with previous works [11], [16] and [12] where this factor does not appears. Moreover we have that $\sigma(x_o) > 0$ $\mu(x_o) > 0$ and $\lambda(x_o) > 0$ as claimed in Section 2.7.

Observe that approximation (2.71) reproduces very well the coherent part of the pulse at each station considered.

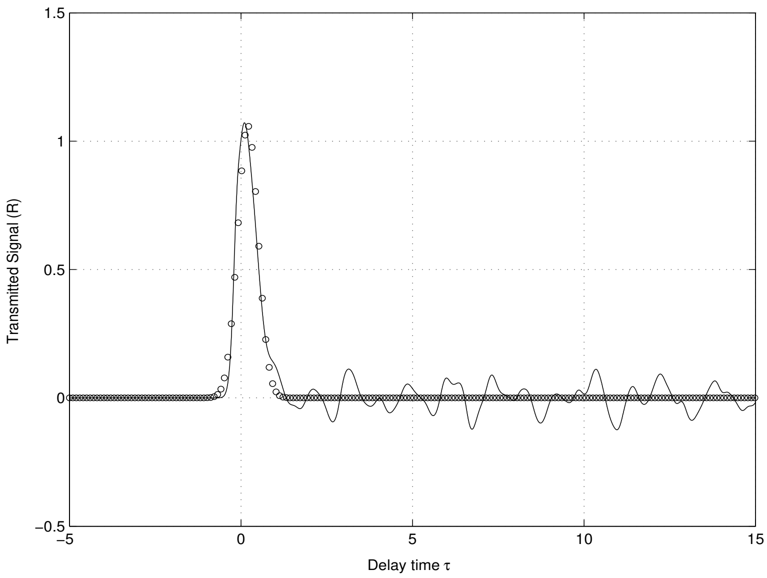


Figure G.4: Pulse propagating over a disordered rapidly-varying orography. Solid line: Numerical solution for $\alpha = 0.001$, $\beta = 0$ at $\xi = 40$ (40 pulse widths). Dotted line : Approximation (2.78).

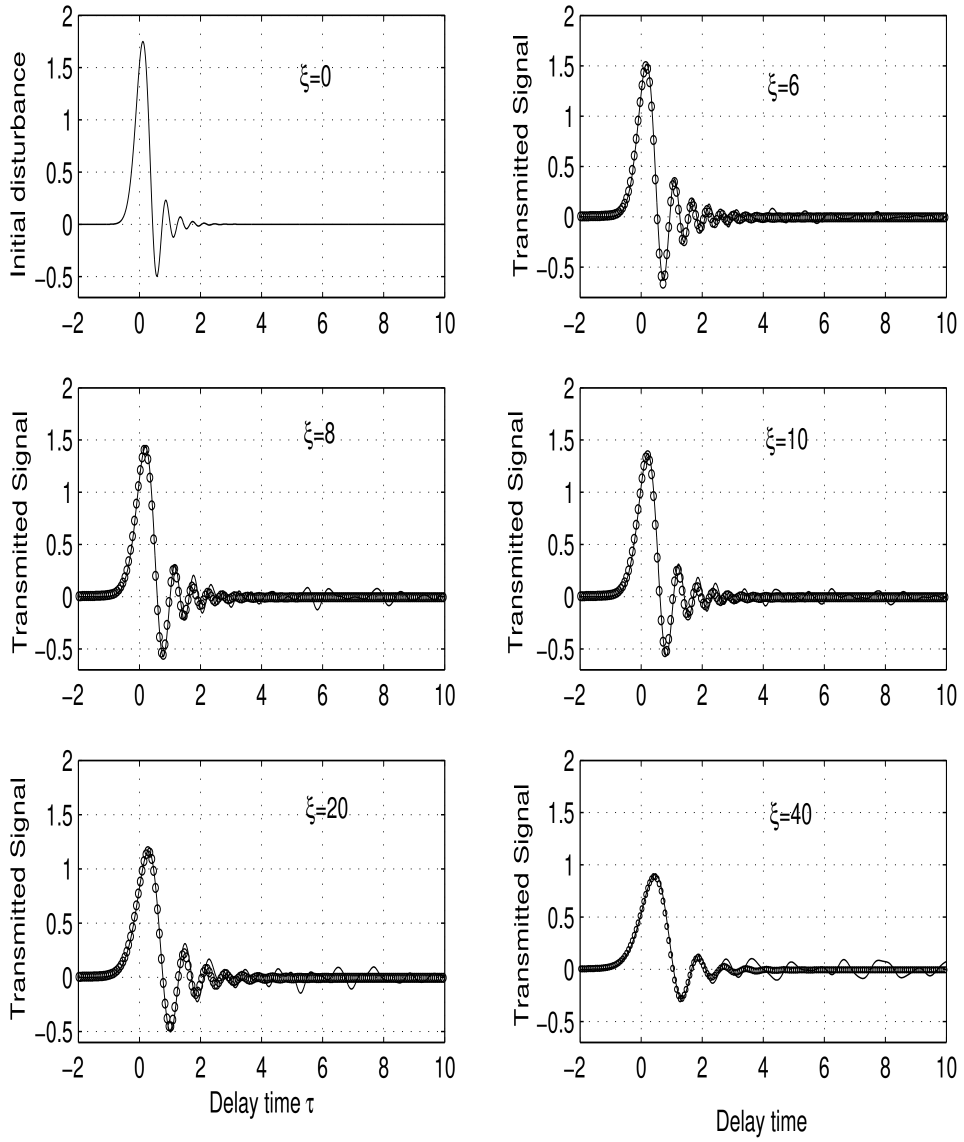


Figure G.5: Pulse propagating over a disordered rapidly-varying orography at six different medium's locations for $\alpha = 0.001$, $\beta = 0.002$. Solid line : Numerical solution. In dotted line : Approximation (2.71).

# Appendix H

# Error estimation of Wei and Kirby's scheme

In this appendix we will show that the truncation error of the predictor-corrector scheme introduced in Chapter 3 is formally of order $O(\Delta\xi^2) + O(\Delta t^4)$ when applied to the linear Boussinesq system ($M \equiv 1$)

$$\begin{aligned} \eta_t &= E(\eta, u) = -u_\xi, \\ V_t &= F(\eta, u) = -\eta_\xi, \end{aligned}$$

where $V = u - (\beta/3)u_{\xi\xi}$.

In the following, $A, B, C, D$ are constants. We only analyze the corrector step given by the fourth-order Adams-Moulton scheme

$$\begin{aligned} \eta_j^{n+1} &= \eta_j^n + \frac{\Delta t}{24}(9E_j^{n+1} + 19E_j^n - 5E_j^{n-1} + E_j^{n-2}) - D\Delta t^5 E_{tttt}, \\ V_j^{n+1} &= V_j^n + \frac{\Delta t}{24}(9F_j^{n+1} + 19F_j^n - 5F_j^{n-1} + F_j^{n-2}) - D\Delta t^5 F_{tttt}. \end{aligned}$$

When the first-order derivatives $u_\xi$ and $\eta_\xi$ are approximated to fourth-order accuracy and $u_{\xi\xi}$ is discretized by second-order centered differences, it yields that

$$\begin{aligned} \frac{\eta_j^{n+1} - \eta_j^n}{\Delta t} &= \frac{1}{24}(9E_j^{n+1} + 19E_j^n - 5E_j^{n-1} + E_j^{n-2} + A\Delta\xi^4 u_{\xi\xi\xi\xi\xi}) + D\Delta t^4 u_{\xi tttt}, \quad \text{(H.1)} \\ \frac{u_j^{n+1} - u_j^n}{\Delta t} &= \frac{\beta}{3}\left(\frac{u_{j+1}^{n+1} - 2u_j^{n+1} + u_{j-1}^{n+1}}{\Delta\xi^2\Delta t} - \frac{u_{j+1}^n - 2u_j^n + u_{j-1}^n}{\Delta\xi^2\Delta t} + C\Delta\xi^2 u_{\xi\xi\xi\xi t}\right) \\ &\quad + \frac{1}{24}(9F_j^{n+1} + 19F_j^n - 5F_j^{n-1} + F_j^{n-2} + B\Delta\xi^4 \eta_{\xi\xi\xi\xi\xi}) + D\Delta t^4 \eta_{\xi tttt}, \end{aligned}$$

The terms $A\Delta\xi^4 u_{\xi\xi\xi\xi\xi}$ and $B\Delta\xi^4 \eta_{\xi\xi\xi\xi\xi}$ in equations above correspond to the truncation errors of the 4th-order approximations of the derivatives $u_\xi$ and $\eta_\xi$ in the fields $E$ and $F$.

This verifies the order $O(\Delta\xi^2) + O(\Delta t^4)$ of the scheme. Observe also that all truncation errors contain only fifth-order derivatives of the form $\Delta t^4 u_{\xi tttt}$, $\beta\Delta\xi^2 u_{\xi\xi\xi\xi t}$, $\Delta\xi^4 u_{\xi\xi\xi\xi\xi}$ and similar terms for $\eta$. Therefore with this high order discretization we eliminated all truncation terms of the same form as the dispersive third-order derivative $(\beta/3)u_{\xi\xi t}$ appearing on the model. This is important so that the dispersive characteristics of the Boussinesq model be accurately reproduced by the numerical scheme.

# Bibliography

[1] Abramowitz, M. and Stegun, I. A. *Handbook of Mathematical Functions.* Dover, 1968.

[2] Ahlfors, L. V. *Complex Analysis : an introduction to the theory of analytic functions of one complex variable.* 2d. ed., McGraw-Hill, New York, 1966.

[3] Ash, M., Kohler, W., Papanicolaou, G., Postel, M. and White, B. Frequency content of randomly scattered signals. *SIAM Review* 33, pp. 519-625, 1991.

[4] Bellman, R. and Kalaba, R. On the principle of invariant imbedding and propagation through inhomogeneous media. *Proc. Nat. Acad. Sci. U.S.A.*, 42, pp. 629-632, 1956.

[5] Bellman, R., Kalaba, R. and Wing, G. M. Invariant Imbedding and Mathematical Physics I. Particle Processes. *J. Math. Phys.*, Vol. 1, No. 4, pp. 280-308, 1960.

[6] Bellman, R., Cooke, K. L., Kalaba, R. and Wing, G. M. Existence and Uniqueness Theorems in Invariant Imbedding. Conservation Principles. *J. Math. Anal. and Appl.* 10, pp. 234-244, 1965.

[7] Bellman, R. and Wing, G. M. *An introduction to invariant imbedding.* Wiley, 1975.

[8] Bona, J. and Chen, M. A. Boussinesq system for two-way propagation of nonlinear dispersive waves. *Physica D*, 116, pp. 191-224, 1998.

[9] Berlyand, L. and Burridge, R. The accuracy of the O'Doherty-Anstey approximation for wave propagating in highly disordered stratified media. *Wave Motion* 21, pp. 357-373, 1995.

[10] Brigham, E. O. *The Fast Fourier Transform and its Applications.* Prentice Hall, 1988.

[11] Burridge, R. and Chang, H. Multimode, one dimensional wave propagation in a highly discontinuous medium. *Wave Motion* 11, pp. 231-249, 1988.

[12] Burridge, R., Papanicolaou, G. and White, B. S. One-dimensional wave propagation in a highly discontinuous medium. *Wave Motion* 10, pp. 19-44, 1988.

[13] Burridge, R., Papanicolaou, G., Sheng, P. and White, B. Probing a random medium with a pulse. *SIAM J. Appl. Math.*, Vol. 49, No. 2, pp. 582-607, 1989.

[14] Carrier, G. F. Gravity waves on water of variable depth. *J. Fluid Mech.* 24, pp. 641-659, 1966.

[15] Clark, T. L. A small scale dynamical model using a terrain–following coordinate transformation, J. Comput. Phys., **24** (1977), pp. 136–215.

[16] Clouet, J. F. and Fouque, J. P. Speading of a pulse travelling in random media. *The Annals of Applied Probability*, Vol. 4, No. 4, pp. 1083-1097, 1994.

[17] Clouet, J. F. and Fouque J. P. A time-reversal method for an acoustical pulse propagating in randomly layered media. *Wave Motion* 25, pp. 361-368, 1997.

[18] Driscoll, T. http://www.math.udel.edu/driscoll/software.

[19] Engquist, B. and Majda, A. Absorbing boundary conditions for the numerical simulation of waves. *Math. Comp.* 31 (139), pp. 629-651, 1977.

[20] Fink, M. Time-reversed acoustics, *Scientific American,* pp. 67-93, 1999.

[21] Fouque, J. P., Garnier, J. and Nachbin, A. The O'Doherty-Anstey theory and time reversal for nonlinear water waves in random media, preprint, 2002.

[22] Fouque, J. P. and Nachbin, A. Time-reversed refocusing of surface water waves. Submitted for publication, 2002.

[23] Fouque, J. P., Garnier J. and Nachbin, A. Time reversal for dispersive waves in random media, preprint, 2002.

[24] Gill, A. E. *Atmosphere–Ocean Dynamics*, Academic Press, 1982.

[25] Guazzeli, E. Rey, V. and Belzons, M. Higher Order Bragg Reflection of Gravity Surface Waves by Periodic Beds. *J. Fluid Mech.* 245, pp. 301-317, 1992.

[26] Hamilton, J. Differential equations for long-period gravity waves on a fluid of rapidly vaying depth. *J. Fluid Mech.* 83, pp. 289-310, 1977.

[27] Howell, L. H. and Trefethen, L. N. A modified Schwarz-Christoffel transformation for elongated regions. *SIAM J. Sci. Stat. Comput.*, Vol. 11, No. 5, pp. 928-949, 1990.

[28] John, Fritz. *Partial Differential Equations.* 4th ed., Springer, 1982.

[29] Keller, J. B. Surface waves on water on non-uniform depth. *J. Fluid Mech.* 4, pp. 607-614, 1958.

[30] Keller, H. B. *Numerical Methods for two-point boundary value problems.* Blaisdell Publishing Company, 1968.

[31] Kreisel, G. Surface waves. *Q. Appl. Maths* 7, pp. 21-44, 1949.

[32] Lewicki, P., Burridge, R. and Papanicolaou, G. Pulse stabilization in a strongly heterogeneous layered medium. Wave Motion 20, pp. 177-195, 1994.

[33] Lewicki, P. and Papanicolaou, G. Reflection of wavefronts by randomly layered media. *Wave Motion*, 20, pp. 245-266, 1994.

[34] Lewicki, P. Long time evolution of wavefronts in random media. *SIAM J. Appl. Math.*, Vol. 54, No. 4, pp. 907-934, 1994.

[35] Lewicki, P., Burridge R. and de Hoop, M. Beyond effective medium theory: Pulse stabilization for multimode wave propagation in high-contrast layered media, *SIAM J. Appl. Math.*, 56, No. 1, pp. 256-276, 1996.

[36] Liu, P., Yoon, S. and Kirby, J. Nonlinear refraction- diffraction of waves in shallow water. *J. Fluid Mech.*, Vol. 153, pp. 185-201, 1985.

[37] Madsen, A., Murray, R. and Sørensen, O. R. A new form of the Boussinesq equations with improved linear dispersion characteristics. *Coastal Eng.* 15, pp. 371-388, 1991.

[38] Mattioli, F. Decomposition of the Boussinesq Equations for Shallow-Water into a set of Coupled Korteweg-de Vries Equations. *Phys. Fluids* A 3 (10), pp. 2355-2359, 1991.

[39] Mattioli, F. On the Hamiltonian Decomposition of the Boussinesq Equations in a pair of Coupled Korteweg-de Vries Equations. *Wave Motion* 28, pp. 283-296, 1998.

[40] Mei, C. C. *The Applied Dynamics of Ocean Surface Waves*, John Wiley, 1983.

[41] Mei, C. C. and Black, J. L. Scattering of surface waves by rectangular obstacles in waters of finite depth. *J. Fluid Mech.* 38, pp. 499-511, 1969.

[42] Meyer, G. *Initial Value Methods for Boundary Value Problems : Theory and Application of Invariant Imbedding.* Academic Press, 1973.

[43] Muñoz Grajales, J. C. and Nachbin, A. Dispersive wave attenuation due to orographic forcing. Submitted for publication, 2002.

[44] Nachbin, A. *Modelling of Water Waves in Shallow Channels.* Computational Mechanics Publications, Southampton, U.K., 1993.

[45] Nachbin, A. A terrain-following Boussinesq system. To appear in *SIAM J. Appl. Math.*

[46] Nachbin, A. The localization length of randomly scattered water waves. *J. Fluid Mech.*, 296, pp. 353-372, 1995.

[47] Nachbin, A. and Papanicolaou, G. Water waves in shallow channels of rapidly-varying depth. *J. Fluid Mech.*, Vol. 241, pp. 311-332, 1992.

[48] Nwogu, O. Alternative form of Boussinesq equations for nearshore wave propagation. *J. Waterway, Port, Coastal and Ocean Engineering*, 119, pp. 618-638, 1993.

[49] O'Doherty, R. F. and Anstey, N. A. Reflections on amplitudes. *Geophysical Prospecting*, 19, pp. 430-458, 1971.

[50] Papanicolaou, G. and Sølna, K. Ray theory for a locally layered random medium, *Waves in Random Media* **10**, 151, 2000.

[51] Peregrine, D. H. Long waves on a beach. *J. Fluid Mech.* 27, pp. 815-827, 1967.

[52] Prada C. and Fink, M. Eigenmodes of the time reversal operator : A solution to selective focusing in multiple-target media. *Wave Motion* 20, pp. 151-163, 1994.

[53] Rosales, R. R. and Papanicolaou, G. C. Gravity waves in a channel with rough bottom. *Stud. Appl. Maths.* 68, pp. 89-102, 1983.

[54] Scott, M. *Invariant Imbedding and its Applications to Ordinary Differential Equations. An introduction.* Addison-Wesley, 1973.

[55] Sølna, K. Stable spreading of acoustic pulses due to laminated microestructure. Ph.D. dissertation, Stanford University, 1997.

[56] Wei, G. and Kirby, J. Time-Dependent Numerical Code for Extended Boussinesq Equations. *J. of Waterway, Port, Coastal and Ocean Engineering*, vol. 121, No. 5, pp. 251-261, 1995.

[57] Whitham, G. B. *Linear and Nonlinear Waves*, John Wiley, 1974.

[58] Yoon, S. and Liu, P. Resonant reflection of shallow-water waves due to corrugated boundaries. *J. Fluid Mech.*, Vol. 180, pp. 451-469, 1987.